TEMPERATURE-COMPENSATED CALIBRATION AND MEASUREMENTS WITH CROSS-STYLE HOTWIRE ANEMOMETERS

A Thesis
by
COLTON PHILLIP FINKE

Submitted to the Graduate and Professional School of
Texas A&M University
in partial fulfillment of the requirements for the degree of

MASTER OF SCIENCE

Chair of Committee,	Edward B. White
Committee Members,	Diego Donzis
	Mirjam Fürth
Head of Department,	Srinivas Vadali

December 2021

Major Subject: Aerospace Engineering

ABSTRACT

Flow field measurements collected using constant-temperature hotwire anemometers (CTAs) are known to be sensitive to variation in the ambient fluid temperature. Various calibration techniques are detailed in literature for temperature compensation of single-component velocity measurements using single-normal hotwires. However, a rigorous methodology has not yet been defined for temperature compensation in two-component velocity measurements using cross-style hotwires. This research defines a procedure for the calibration of cross-style hotwires from which temperature compensated estimates of the streamwise, U, and spanwise, W, components of the local velocity are obtained. To map the effects of ambient temperature, flow angularity, and velocity magnitude to hotwire voltages, a series of four calibration sweeps is conducted at the beginning of each day of operation. Resulting velocity component accuracy is analyzed for several known flow angle, temperature, and velocity magnitude combinations in the freestream. Based on the study's results, model form errors in the hotwire responses are known *a priori* for general experiments to remain under 2% for measurements taken within the bounds of the calibration probe angle range while component uncertainties are determined for the included experiment *a posteriori* to range up to $\pm 1.1\%$ of the measured velocity magnitude and within $\pm 0.6^\circ$ of the measured flow angle. Comparisons of cross-style and single-normal hotwire flat-plate boundary layer measurements in the wake of a vortex generator demonstrate excellent agreement in the streamwise component estimates.

DEDICATION

To my family and friends,
for years of love and support.

ACKNOWLEDGMENTS

I am greatly thankful to my research advisor, Dr. Edward White, for his guidance throughout my time at the Klebanoff-Saric Wind Tunnel. His technical input in discussions was always helpful and his conversational tangents were always enlightening. I would also like to thank my thesis committee members, Dr. Diego Donzis and Dr. Mirjam Fürth, for their time and supportive comments and suggestions, and my academic advisor, Mrs. Gail Rowe, for her helpful responses and general positivity.

My thanks are also extended to Jeppesen Feliciano, Ezequiel Justiniano, and Eleazar Herrera, whose support in the setup and execution of experiments was vital to the timely completion of this degree. The COVID-19 pandemic led to delays in various experiments, but, with tireless effort, everyone in the lab came together to bring back operations and enable this research.

I am incredibly thankful for all of the love and support that I have received from both family and friends. They have brought me to where I stand today, and I am blessed to have them in my life. Finally, I owe much of what I have accomplished to Mr. Ralph Real, my high school Algebra II–Calculus teacher. His love for the subject and its application inspired me to pursue an engineering degree and ignited my love for learning.

CONTRIBUTORS AND FUNDING SOURCES

Contributors

This work is supported by a thesis committee consisting of Dr. Edward B. White and Dr. Diego Donzis of the Department of Aerospace Engineering and Dr. Mirjam Fürth of the Department of Ocean Engineering.

Jeppesen Feliciano and Ezequiel Justiniano supported in the setup of the test section in preparation for the present experiment. Eleazar Herrera assisted in the running of boundary layer experiments using the cross-style hotwires.

Funding Sources

The work presented here was funded by grants from the Air Force Office of Scientific Research, #FA9550-19-1-0145, and the National Science Foundation, #1805889.

TABLE OF CONTENTS

Page

LIST OF FIGURES

LIST OF TABLES

TABLE Page

1. INTRODUCTION

1.1 Motivation

Hotwire anemometry is a well-established technique used to collect high-resolution velocity measurements in a variety of flow conditions. The basic concept is that the fluid velocity can be estimated based on heat transfer from a slender wire to the surrounding fluid. As such, the method is sensitive to ambient temperature variations.

For experiments using so-called single-normal hotwires, whose sensing element is oriented normal to the principle flow direction to measure a single component of the flow field, several methods of temperature compensation have been developed to reduce the effects of ambient temperature variation on hotwire response. A rigorous approach to temperature compensation in two-component velocity measurements using a cross-style hotwire probe has not yet been developed. The intent of this work is to provide a detailed method of incorporating temperature compensation into the daily calibration of cross-style hotwires as well as a means of quantifying the calibration's error and uncertainty.

1.2 Fundamental Principles of Hotwire Anemometry

The fundamental heat transfer problem governing hotwire anemometer response is that of convection to the surrounding fluid from a slender wire oriented normal to the principle flow direction. In constant temperature anemometry (CTA), the wire temperature, T_w, is held constant using a feedback control loop applied to a wheatstone bridge circuit. The feedback rapidly adjusts the applied current through the wire to compensate for instantaneous changes in the local fluid velocity. From the method proposed by King [1], the heat transfer relationship is generally written in terms of the Nusselt and Reynolds numbers as

$$Nu \equiv \frac{hD}{k} = A^{III} + B^{III}\, Re_D^{0.5}, \tag{1.1}$$

where A^{III} and B^{III} are empirical coefficients, h is the convective heat transfer coefficient, D is the wire diameter, and k is the fluid thermal conductivity. Because Eq. 1.1 is empirical and better results could be obtained by allowing the Reynolds exponent to vary, the exponent of 0.5 is commonly substituted with $1/n$, where n is a third empirical coefficient ([2], [3], [4]).

Following Bruun [2], the relationship between the actual voltage across the hotwire, E_w, and the voltage output by the anemometer, E, is represented by

$$E = \frac{R_p + R_L + R_w}{R_w} E_w, \tag{1.2}$$

where R_p, R_L, and R_w are the resistances of the probe stem, cable, and wire, respectively. The electrical power dissipated through the hotwire can then be written as

$$\frac{E_w^2}{R_w} = \frac{E^2 R_w}{\left(R_1 + R_L + R_w\right)^2} = \left(A^{II} + B^{II}\, V^{1/n}\right) \left(T_w - T_a\right), \tag{1.3}$$

where V is the velocity of the fluid and T_w and T_a are the wire and ambient temperatures, respectively. The probe and cable resistances are constant and, for CTA, the wire resistance is constant as well. All of the resistances can therefore be absorbed into the leading coefficients, reducing Eq. 1.3 to

$$E^2 = \left(A^I + B^I\, V^{1/n}\right) \left(T_w - T_a\right). \tag{1.4}$$

If T_a is also constant then $(T_w - T_a)$ can also be absorbed into the unknown constants. Under these assumptions, the common form for the convective heat transfer equation relating the measured hotwire voltage to the local velocity is

$$V = \left(A + B\, E^2\right)^n, \tag{1.5}$$

where A, B, and n are empirical coefficients determined during calibration of the hotwire and E is the hotwire voltage.

Equation 1.5 is the foundation upon which this research is constructed, but the intended operating conditions (cross-style hotwire measurements with variable ambient temperature) raise two points of conflict:

1. the orientation of each wire comprising a cross-style probe is approximately ±45° with respect to the flow direction while the fundamental heat transfer relationship is based on flow perpendicular to the wire, and
2. the ambient temperature varies throughout the day while the equation assumes a constant temperature.

Previous research has addressed both of these problems independently, however no rigorous method addresses both problems simultaneously. This research seeks to merge these established solutions to enable temperature compensated cross-style hotwire measurements.

1.3 Background

Many variations of the basic hotwire calibration technique exist, reviews of which are presented by Bruun [2], Stainback [5], and Comte-Bellot [6]. Because the heat transfer relationship embodied in King's Law depends on more than simply fluid velocity, hotwires require frequent calibration in laboratory settings [7]. Hotwire calibration is straightforward when the wire is oriented normal to the principle flow direction and when the ambient temperature is constant. However, when hotwires are required to make multi-component velocity measurements or when fluid temperature varies during an experiment, more sophisticated calibration approaches are required. The calibration technique described in this research addresses the scenario in which cross-style CTAs are used to make two-component velocity measurements as ambient fluid temperature varies.

1.3.1 Multi-Component Velocity Measurements

Cross-sytle hotwires are used when two-component measurements of the velocity field are sought. A cross-style hotwire setup consists of two oppositely oriented, single-inclined hotwires spaced 1 millimeter apart. During experiments in which the probe stem is aligned with the principle flow direction, the two wires are inclined to the flow approximately ±45°. Calibration of crosswires occurs in the freestream and requires varying both the principle flow magnitude and the probe angle in order to generate a unique relationship between the two hotwire voltage outputs (E_1, E_2) and some combination of parameters that is sufficient to calculate the velocity vector (either the velocity magnitude and angle or the two components of the velocity vector).

Bruun [2] details two methods of calibrating cross-style hotwires, the first of which is the V_e-calibration method. An individual hotwire is known to have different responses to components of the velocity acting normal, tangential, and binormal to it. An effective cooling velocity, V_e, is used to encapsulate the response of the wire to all of the velocity components. For measurements of a single-inclined hotwire in a three-dimensional flow-field, the effective cooling velocity concept was defined by Jorgensen [8]

$$V_e = \left(V_N^2 + k^2 V_T^2 + h^2 V_B^2\right)^{1/2}, \tag{1.6}$$

where V_N, V_T, and V_B are the velocity components normal, tangent, and binormal to each wire, k is the yaw sensitivity coefficient, and h is the pitch sensitivity coefficient. Hinze [9] proposed a widely-used simplification of Jorgensen's formula for two-dimensional flows in which $V_B = 0$. For two-dimensional flows lying in the same plane as the hotwire sensing element, the components can be rewritten in terms of known calibration parameters

$$V_e = \left(V_N^2 + k^2 V_T^2\right)^{1/2} = U_\infty \left(\cos^2\alpha + k^2 \sin^2\alpha\right)^{1/2}, \tag{1.7}$$

where U_∞ is the freestream velocity magnitude and α is the angle between the wire-normal direction and the principle flow direction. In the V_e-analysis method, each wire is treated independently and calibrated at yaw positions about its nominal experimental orientation. King's Law can be used to model the convective heat transfer for a slanted wire if the effective velocity is used in the place of the principle flow magnitude normal to the wire used Eq. 1.5 such that

$$V_e = \left(A + B\, E^2\right)^n. \tag{1.8}$$

It is important to note that the hotwire voltage in this expression has not been adjusted to a constant temperature. During calibration, empirical coefficients A, B and n are determined for each wire that best represent the relationship between their respective effective velocities and measured voltages using Eq. 1.8. After calibration, the measured voltages and empirical coefficients from each wire are used to calculate the effective velocities. Using the two wire's effective velocities, a modified sum and difference method can be used to calculate the in-plane velocity components. This method is widely used in practice (e.g., Refs. [10] and [11]).

The second method reported by Bruun is the multi-angle calibration method, which requires a dense velocity and probe angle calibration spanning the anticipated velocity magnitude and flow angle range to establish a suitable mapping to the two voltage measurements. During experiments, voltage measurements from each of the hotwires are used in an interpolative look-up method through the calibration database to determine a best estimate of the velocity magnitude and angle combination. Bruun reports that this method is generally more accurate than its effective velocity counterpart, but the considerable amount of time it would take to complete the calibration on a daily basis makes it undesirable.

The two methods of calibrating cross-style hotwires detailed by Bruun are some of the most widely used, however several other variants have been defined. Rather than using King's Law to relate the hotwire voltage to the local velocity, Talamelli *et al.* [12] use an alternate expression in which a secondary term is used to account for the effects of free convection at low velocities (formulated by Johansson and Alfredsson [13]). Analysis assumed a two-dimensional flow-field and applied Hinze's effective velocity formulation (Eq. 1.7) with a negligibly small yaw sensitivity coefficient. For zero yaw sensitivity coefficient, the effective velocity is governed by a pure cosine cooling law and calibration at multiple angles is not necessary; their procedure was reduced to a simple velocity calibration. Morrison *et al.* [14] introduced a dynamic cross-style hotwire calibration method in which a shaker mechanism is used to oscillate the probe in a uniform flow. By oscillating the probe in the streamwise and spanwise directions separately, the velocity sensitivities could be evaluated through relating the velocity component fluctuations to the fluctuating hotwire voltage signal. The results of the static versus dynamic calibration methods are comparable, however dynamic calibration introduces potentially significant dynamic-prong effects which can lead to large deviations from static calibration results. Further studies of dynamic calibration are conducted by Mulhearn and Finnigan [15] and Kühn and Dressler [16].

Many studies have examined the calibration of single-inclined hotwires, and these methods can be applied to the crosswire calibration for each wire independently. Bruun and Tropea [4] investigated several yaw sensitivity functions in addition to two yaw calibration procedures of single-normal and single-inclined probes. They found that the yaw correction factors can vary significantly and are very sensitive to the yaw calibration approach used. When statistical velocity measurements are sought in low turbulence intensity regions, the standard V_e approach was found to yield sufficiently accurate results (A, B, n and the squared yaw sensitivity coefficient k^2 are assumed constant and independent of flow angle). However, for instantaneous velocity measurements or high turbulence intensity flows they found that A, B, n and k^2 are yaw dependent functions. Ultimately, selection of yaw correction and calibration methods depend upon the conditions under which the probes will be used. Adrian *et al.* [17] present the results of an extensive study comparing various formulations of the effective velocity under different flow conditions. They introduced both yaw and pitch angles in the calibration of a single-normal hotwire and subjected the probe to sixty-six different combined pitch and yaw configurations for varying velocities. Of the effective velocity formulations examined, that proposed by Jorgensen [8] proved to be the most accurate for three-dimensional flows. The effective velocity formulation proposed by Hinze [9] was found to provide the best results for two-dimensional flows, for which only the yaw angle was varied.

Each of the sources reviewed in this section propose methods with which to calibrate cross-style CTAs for flow-angle effects while neglecting ambient temperature variation effects. The concept of the effective cooling velocity offers closure to the first fundamental heat transfer equation issue identified in Section 1.2: the wires comprising the crosswire are not perpendicular to the flow. Further improvements to the calibration will be required in order to implement some form of temperature compensation in these multi-component velocity measurements.

1.3.2 Temperature Compensation

Compensating hotwire voltage during calibrations for fluid temperature variation is required in experiments in which the ambient fluid temperature may change. In long-duration experiments, the wind tunnel ambient temperature can change substantially and require the inclusion of ambient temperature compensation. This section will detail several existing methods of temperature compensation for CTAs.

There are a number of temperature calibration methods for single-normal hotwires that are not governed by any heat transfer relationships. A robust method of correcting for many sources of voltage drift was proposed by Talluru *et al.* [18]. In their method, a hotwire undergoes pre- and post-experiment calibration sweeps in addition to intermediate single point recalibrations at regular intervals throughout the course of the experiment. Each recalibration point is conducted at a pre-defined location with reference to a fixed Pitot tube. The recalibration point measurements are then applied in post-processing to create intermediate calibration curves from which the experiment's measured voltages can be corrected using a cubic-spline interpolation scheme. A correction method for CTAs developed by Hultmark and Smits [19] resulted in consistent voltage outputs for temperatures ranging 15°C. In typical calibration procedures which determine the velocity, U, as a function of the hotwire voltage, E, conducting velocity sweeps at different temperatures result in different U-E curves. By instead conducting a calibration relating U/ν to $E^2/k\Delta T$ (where ν is the fluid kinematic viscosity, k is the fluid thermal conductivity, and ΔT is the difference between the wire and ambient temperatures, $T_w - T_a$), they found that the curves are independent of temperature and that only a single velocity sweep is necessary to calibrate the hotwire. The model requires knowledge of the wire temperature, T_w, and the fluid properties, k and ν, as a function of temperature.

For single-normal hotwires, various methods of temperature compensation have been proposed that utilize heat transfer relationships without all of the simplifying assumptions made in Section 1.2. Takagi [20] demonstrates the effectiveness of a temperature compensation method that exhibits voltage drift less than 1% of the indicated velocity after a temperature increase of 25°C. Great care was taken to achieve reproducible least-squares calibration coefficients within 1.5%; the hotwire sensor was cleaned with acetone every two hours to eliminate effects of dust particle collection on voltage output. To achieve these results, however, the physical properties of the hotwire probe and a compensating probe were required, including the various resistances of the system at 0°C and the temperature coefficients of the resistance. Cimbala and Park [21] detail a method which enables the calibration for velocity as a direct function of ambient temperature, pressure, and hotwire voltage. Their approach included the wire temperature, T_w, as one of the least-squares calibration coefficients fit to fundamental heat transfer relationships, eliminating the need to know the overheat ratio.

For single-normal hotwires, Bremhorst [22] details the use of a linearized coefficient relating squared hotwire voltage to the ambient temperature as a function of velocity. This temperature compensation coefficient requires two velocity calibration sweeps separated by a temperature differential exceeding the temperature bounds of the day's experiments. This method was found to be the most accurate of those compared by Bowers *et al.* [23], however it required the use of a polynomial fit procedure. White [3] has since applied an analytical-compensation technique such that the temperature compensation coefficient is related to the velocity via King's Law with a variable exponent for improved results. The approach is to replace the measured voltage E in King's Law with a temperature-compensated voltage, $\widehat{E}$, the voltage that would be measured by the hotwire if the ambient temperature were equal to some constant "compensation temperature", $\widehat{T}$, rather than the actual ambient temperature T. This is accomplished using a temperature-compensation coefficient C_T that is a function of the hotwire local velocity V:

$$\widehat{E}^2 = E^2 + C_T\left(V\right)\left(\widehat{T} - T\right). \tag{1.9}$$

The temperature compensation coefficient serves as an interpolation from the measured ambient temperature to the compensation temperature, $\widehat{T}$, and its form can be derived from King's Law as

$$C_T\left(V\right) = \frac{E_h^2 - E_c^2}{T_h - T_c} = -\widehat{A} - \widehat{B}\, V^{1/\widehat{n}}, \tag{1.10}$$

in which the fit parameters $\widehat{A}$, $\widehat{B}$, and $\widehat{n}$ are denoted with hat symbols to mark them as distinct from the equivalent variables in King's Law. The subscripts h and c refer to the voltages and temperatures during "hot" and "cold" calibration runs during which the $C_T\left(V\right)$ input data are generated.

One simple but limited approach to the introduction of temperature compensation in cross-style hotwire measurements was used by Downs [11] to measure multiple components of freestream turbulence in a variable-temperature flow. Because the mean velocity was constant in Down's experiments, it was assumed that voltage drift was linear with the ambient temperature over small temperature variations. Using this assumption, temperature-compensated calibration was carried out by heating the wind tunnel by operating at a high velocity for several minutes and applying a linear fit to correct the measured voltage to an arbitrary, constant compensation temperature. This approach was successful when applied to an essentially homogeneous mean flow but would not be applied for situations with mean-velocity variations.

While there is extensive literature in temperature compensation inclusion in single-normal hotwire calibration, rigorous techniques for its inclusion in cross-style hotwire calibrations have not been adequately addressed. However, the existence of temperature compensation techniques for the single-normal present means by which the second obstacle posed in Section 1.2 (the ambient fluid temperature is not constant) might be addressed.

1.4 Objectives and Organization

There is a clear need for calibration procedures that enable temperature-compensation of cross-style hotwires intended to operate across a range of velocities, flow angles, and ambient temperatures. The work cited in the sections above only address two of the three requirements at a given time. Several approaches have been developed which address velocity and temperature variation of single-normal hotwires, or velocity and flow angle using cross-style hotwires. Alternatively, Downs [11] proposed a method of temperature compensation for cross-style CTAs, but it was not intended to be applied across a wide range of velocities.

This research intends to establish a rigorous technique to provide temperature-compensation in the calibration of a cross-style hotwire probe. The first objective is to design an analytical approach to merge the processes of adjusting calibration voltages to a constant compensation temperature and executing directional calibrations using effective cooling velocities in order to resolve the conflicts identified in Section 1.2. This also entails defining an efficient operational calibration procedure that enables the merger of the temperature and directionality problems and can be applied daily without a substantial burden on laboratory operations. The results of the first objective will include calibration coefficients and their respective uncertainties. The second objective is to validate the calibration technique using a known parameter-space of flow angles and magnitudes in the freestream. Comparisons of the measured to the expected velocity components will define the error in the calibration while the component uncertainties will be calculated on a point-by-point basis based on the sensor and calibration uncertainties. The third and final objective is to collect cross-style hotwire boundary layer measurements in the wake of a micro-vortex generator (MVG) to showcase the application to complex velocity profiles. The resulting crosswire velocity component measurements will be compared to those of a single-normal hotwire to ensure agreement.

This thesis is organized as follows. Chapter 1 introduces hotwire anemometry and provides foundations in literature for temperature compensation in single-normal hotwires and for the directional calibration of cross-style hotwires. Chapter 2 provides details of the facility and methods used for data acquisition and analysis. Chapter 3 details the analytical basis of the calibration technique as well as the operational procedure. Chapter 4 details how sensor measurements and calibration coefficients are used to determine the velocity components and their uncertainties and error. Chapter 5 shows results of sample calibrations for measurements taken in the freestream for various flow conditions. Chapter 6 compares single-normal and cross-style velocity component measurements in the wake of an MVG. Finally, Chapter 7 provides concluding remarks.

2. FACILITY DESCRIPTION AND EXPERIMENTAL SETUP

2.1 Klebanoff-Saric Wind Tunnel

The experiments for the current research were conducted in the Klebanoff-Saric Wind Tunnel (KSWT) at Texas A&M University. The KSWT is a closed-loop, low-speed wind tunnel designed to produce low levels of freestream turbulence. Hunt *et al.* [24] provide a detailed description of the facility. An overhead perspective of the wind tunnel is depicted in Figure 2.1.

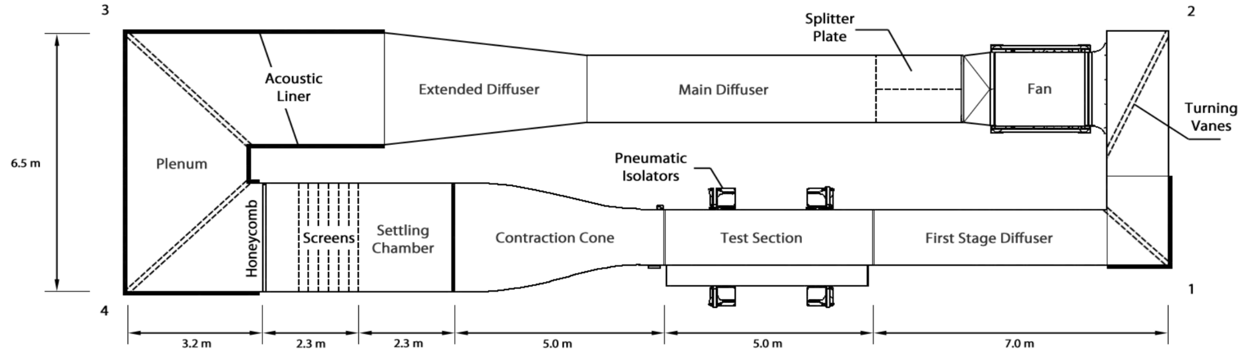

Figure 2.1: KSWT planview

The test section is 5.0 m long with cross section dimensions of 1.4 m × 1.4 m at its upstream entrance. The floor and ceiling of the test section diverge slightly to accommodate boundary layer growth along the tunnel walls, resulting in a 1.41 m × 1.4 m cross section at its downstream exit. The test section features a slotted viewing window compatible with a three dimensional traverse for high resolution hotwire scans. A pneumatic damping system supports the entire test section and traverse system to isolate them from building vibrations while duct tape couplings are used to connect the test section to the rest of the wind tunnel to reduce vibrational effects on hotwire measurements.

The flat plate installed in the test section is 4.4 m long and spans the height of the test section. It has an elliptic leading edge 343 mm long and is constructed with two 1 mm thick aluminum

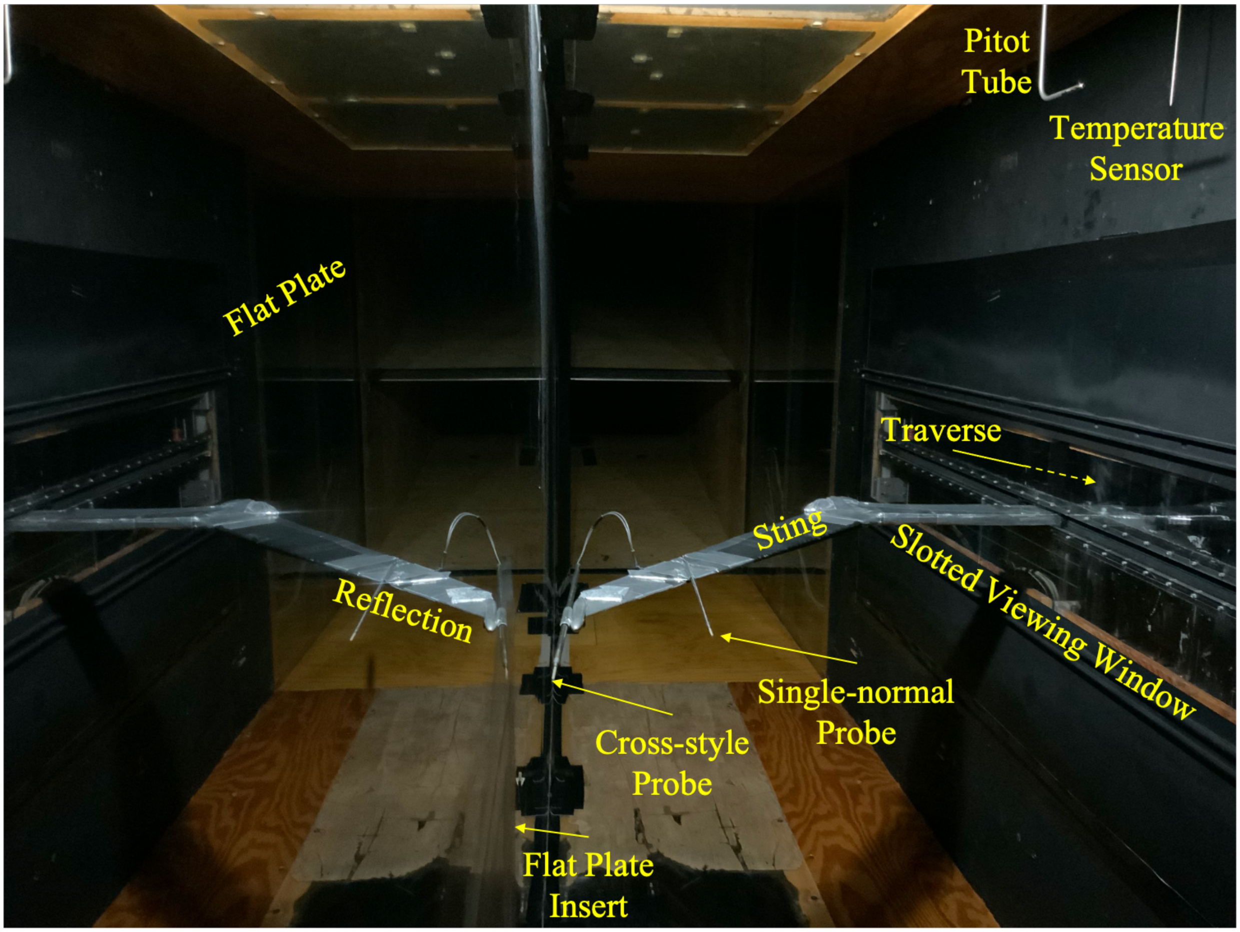

Figure 2.2: Test section layout and components.

skins surrounding a 20 mm thick honeycomb core. To ensure zero pressure gradient within the test region of the plate, a series of mounting brackets are used to manually adjust and fix its orientation. An adjustable trailing-edge flap is also used to shift the leading-edge stagnation point to the test side of the plate. A 0.23 m × 0.28 m rectangular hole is cut into the plate 0.85 m downstream of its leading edge to accommodate different disturbance configurations. For the experiment conducted in this research, the hole was filled by inserting a 3D printed flat plate and applying auto-body filler along the seams to ensure a smooth transition between surfaces.

Measurements of static and dynamic pressure, test section ambient air temperature, and hotwire anemometer signals are collected by three National Instruments USB data acquisition boards (Model USB-6211). Each board accepts 8 differential analog inputs with a -10 V to +10 V maximum range. One of the three boards are dedicated to tunnel state measurements to guide tunnel control including static pressure, dynamic pressure, and temperature. The other two boards are reserved for hotwire anemometer measurements.

The KSWT is controlled based on real-time tunnel measurements of the velocity and hotwire signals using an in-house C++ routine. Estimates of the test section freestream velocity are made using a Pitot tube located approximately 2.2 m downstream of the test section entrance. The Pitot tube measures the static pressure p and dynamic pressure q, and the velocity is estimated using Bernoulli's equation and the ideal gas assumption in the place of fluid density ρ such that.

$$U_0 = \sqrt{\frac{2q}{\rho}} = \sqrt{\frac{2qRT}{p}}, \tag{2.1}$$

where U_0 is the freestream velocity and T is the measured ambient temperature. Ambient temperature is measured using an Omega RTD sensor with a specified accuracy of 0.15°C ($\pm 3\sigma$). Freestream static and dynamic pressure are measured using an MKS Baratron 1000-Torr absolute pressure transducer and an MKS 10-Torr differential pressure transducer, respectively. Both of the transducers have specified accuracies of 0.05% of their respective readings ($\pm 3\sigma$). Using this series of sensor measurements, the KSWT control code can vary the motor rotations per minute to maintain constant velocities or Reynolds numbers up to approximately 31 m/s within an uncertainty of ± 0.1 m/s.

A three-axis traverse system is used to control the hotwire position within the test section. The traverse enables a high spatial resolution for velocity measurements within the boundary layer. Minimum step sizes are listed in Table 2.1. The traverse is separated from the flow-field by a slotted, moveable window whose position changes to avoid collision with the sting, which extends through the slot to support acquisition of hotwire measurements. The entire system is bounded by an additional pressure box which prevents flow entrainment through the slot.

Direction	Max Travel [mm]	Min Step Size [μm]
Streamwise (x)	1300	12
Wall-Normal (y)	90	1
Spanwise (w)	180	2

Table 2.1: Traverse span and resolution

2.2 Hotwire Measurement System

An AN-1003 Constant Temperature Anemometer system is used to collect high resolution velocity estimates of the flow field. Three different-style hotwire probes were used to conduct the present research. A Dantec 55P61 cross-style CTA is the focal point of the research and was calibrated and used to measure U and W components of the flow field. As will be elaborated upon in Chapters 3– 6, this style probe was used in the freestream for both calibration development and freestream validation experiments, but is used in the boundary layer for its application to complex flow measurements. A Dantec 55P11 single-normal CTA was used in the freestream as an edge velocity reference in boundary layer measurements. Lastly, a Dantec 55P16 single-normal CTA was used in the boundary layer application as a streamwise component datum for comparison with the Dantec 55P61 boundary layer measurements. Each hotwire was operated with an overheat ratio of 1.8.

For boundary layer measurements, hotwires are placed in both the freestream and in the boundary layer with a fixed separation distance of approximately 18 cm in the wall-normal direction. Both single-normal hotwires are mounted directly to a sting extending from the traverse system with their probe stems oriented and fixed along the freestream direction. The cross-style probe is mounted to a slender fixture, shown in Figure 2.3, with an adjustable pitch setting that can be changed to various probe angles with uncertainties of $\pm 0.1^\circ$ about a probe angle of 0° and $\pm 0.2^\circ$ otherwise. This fixture connects directly to the end of the sting to enable two-component measurements in the boundary-layer.

In typical experiments conducted in the KSWT, single-normal hotwires are submerged in the

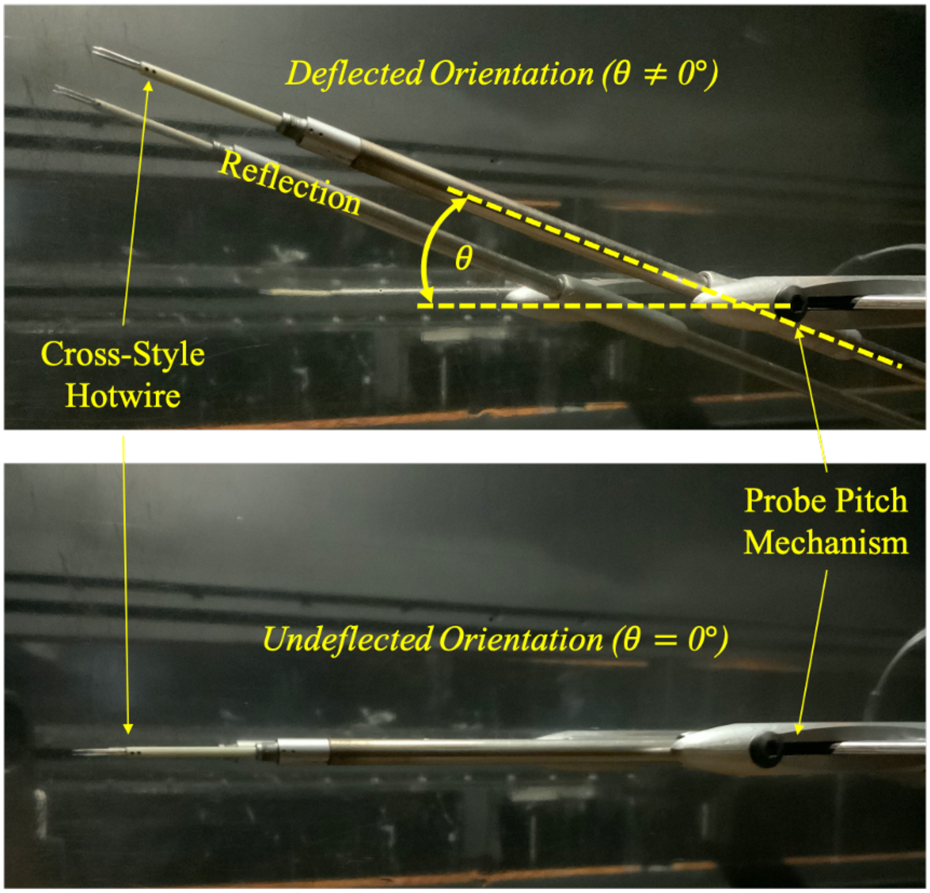

Figure 2.3: Cross-style hotwire probe pitch mechanism.

wake of some disturbance in which the U component of the local velocity field can be estimated from the hotwire voltage and the ambient temperature using a series of calibration coefficients found following the method developed by White [3]. Boundary layer scans are conducted by plunging a hotwire from the freestream into the boundary layer in the wall-normal direction. In laminar regions, points are collected as the traverse moves the hotwire progressively closer to the wall until the boundary layer hotwire measures a specified cutoff velocity, typically $0.12U_\infty$, where U_∞ is the velocity measured by the freestream wire. When the velocity ratio criteria is met, the boundary layer profile scan is terminated and proceeds to the next profile scan for a new spanwise coordinate. Relying upon the fixed velocity cutoff in laminar boundary layers is generally a safe technique because the velocity profile is well-behaved and linear near the wall, offering adequate information to avoid wall collision. In turbulent regions in the wake of a disturbance, higher wall shear moves the scan stopping criteria nearer to the wall which could result in collisions with the wall and breakage of hotwires. To prevent this collision in the turbulent boundary layer, a series of "wall finding" runs can be conducted in the laminar regions outside of the wake prior to running the boundary layer scan in the turbulent region. Using the linear portion of the laminar boundary layer profiles, the y_{wall} locations can be estimated at multiple spanwise locations on either side of the disturbance. A quadratic fit can then be used to estimate the y_{wall} location in the traverse-fixed coordinate system as a function of the spanwise coordinate, z. For measurements within the turbulent region, the boundary layer profile is conducted until the traverse position is within 0.25 mm of the estimated wall location. Based on previous experiments conducted in the KSWT, laminar boundary layers typically consist of approximately 70 two-second-averaged points while turbulent boundary layers can reach up to 120 points.

Prior to the current research, this boundary layer measurement control technique had only been applied using single-normal hotwires. For cross-style hotwires, the effective velocity of the wire nearest the wall can be used in the same way to estimate the distance from the wall. A ratio of the near-wall inclined wire's effective velocity measurement to the freestream single-normal wire's velocity measurement serves as the boundary layer cutoff criteria. The effective velocity measured by the inclined wire is generally smaller than that measured by the single-normal wire, so the ratio itself must be normalized prior to plunging into the boundary layer. The first measurement taken in the freestream of the scan defines the normalizing factor. From this point, measurements in both laminar and turbulent boundary layers can be measured using the same technique as described above for single-normal wires.

3. CALIBRATION APPROACH

3.1 Overview

Adding temperature compensation to the calibration of cross-style hotwires requires combining the two concepts described in Chapter 1. The calibration technique detailed in this chapter is demonstrated in the KSWT using a Dantec type 55P61 cross-style CTA and the experimental setup described in Section 2.2. Calibration of the cross-style probe takes place in the freestream, oriented along the x-direction, and is intended for two-dimensional flows whose wind-frame components are U, oriented along the x direction, and W, oriented along the z direction. The y direction wind-frame velocity component, V, is assumed to be of negligible amplitude and the plane onto which the projections of the cross-style probe's sensing elements form the characteristic "X" is coplanar with the x-z plane. Future work could extend the method to three-dimensional flows. This work will make the distinction of using Jorgensen's [8] formulation (Eq. 1.6) with $V_B = 0$ rather than Hinze's [9] formulation (Eq. 1.7) despite the fact that they are equivalent statements under the specified assumptions.

The calibration technique uses the V_e analysis detailed by Bruun [2] to address the wires' non-perpendicularity to the principle flow direction. The two slanted wires are treated independently during calibration and their responses are each calibrated by relating their respective effective velocities, V_e, as defined by Jorgensen [8] with $V_B = 0$ in Eq. 1.6 to those modeled using King's Law in Eq. 1.8:

$$V_e = \left(A + B\,E^2\right)^n = \left(V_N^2 + k^2 V_T^2\right)^{1/2}. \tag{3.1}$$

Following Bruun's nomenclature, the angle between an individual slanted wire and the wind-fixed z axis is given as

$$\alpha = \bar{\alpha} + \theta, \tag{3.2}$$

in which $\bar{\alpha}$ is the nominal slantwire wire angle, ±40°, and θ is the orientation of the hotwire probe axis with respect to the wind-fixed x axis. For the two-dimensional flow case and assumptions

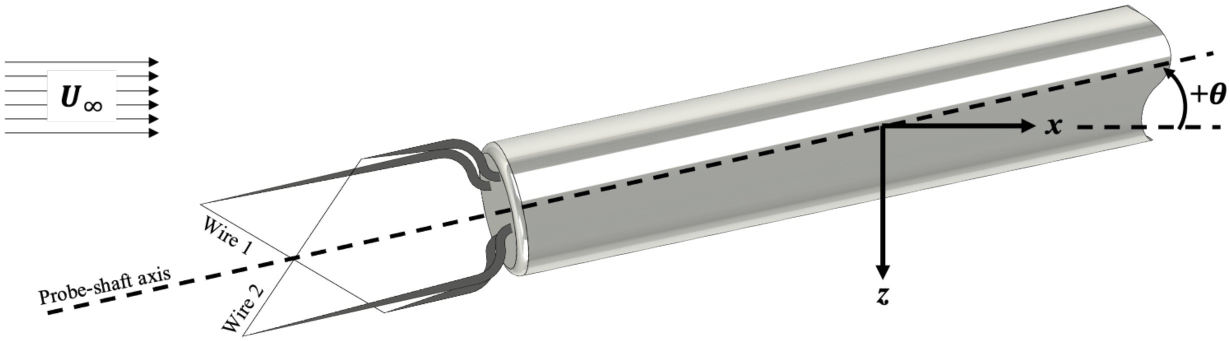

(a) Probe angle definition.

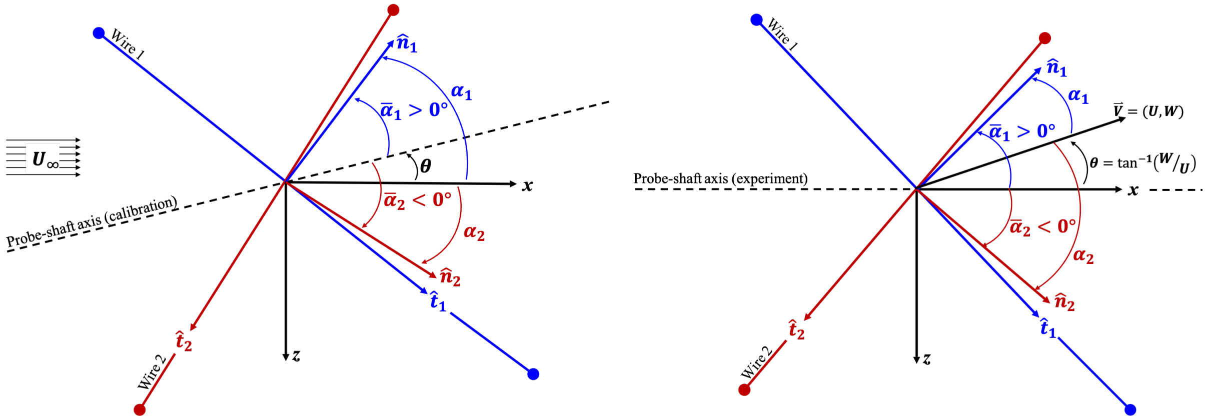

(b) Reference frames during calibration.

(c) Reference frames during experiments.

Figure 3.1: Reference frame definitions for wind-fixed (x and z axes) and wire-fixed coordinate systems ($\widehat{n}$ and $\widehat{t}$ axes). Figure 3.1a shows the probe angle sign convention. Figure 3.1b defines angles relative to the flow direction during calibration in which the probe angle is adjusted to simulate a known flow angle. Figure 3.1c defines angles relative to the flow direction during experiments in which the probe angle is set to zero and the flow angle is arbitrary.

described above, the wires' normal and tangential components are

$$V_N = U \cos\alpha - W \sin\alpha \quad \text{and} \tag{3.3}$$

$$V_T = W \cos\alpha + U \sin\alpha. \tag{3.4}$$

During an experiment, θ is zero and both U and W velocity components may exist. Alternatively, during calibration, W is zero in the freestream and θ is varied by changing the probe angle. This provides calibration input for the determination of each wire's k^2 value. Figure 3.1 depicts the difference in the reference frames between calibration and experiments.

The temperature compensation method developed by White [3] for single-normal hotwires is applied to address the variable ambient fluid temperature problem and adapted for inclined wires by making the correction term a function of the effective velocity, V_e, instead of the total velocity, V. As described in Chapter 1, the method uses a temperature compensation coefficient which relates the hotwire response to temperature as a function of velocity in order to interpolate measured anemometer voltages onto some compensation temperature. This process is summarized for single-normal hotwires in Eqs. 1.9 and 1.10, the respective inclined-wire versions of which are

$$\widehat{E}^2 = E^2 + C_T\left(V_e\right)\left(\widehat{T} - T\right) \quad \text{and} \tag{3.5}$$

$$C_T\left(V_e\right) = \frac{E_h^2 - E_c^2}{T_h - T_c} = -\widehat{A} - \widehat{B}\,V_e^{1/\widehat{n}}. \tag{3.6}$$

Applying White's adapted method enables the replacement of the anemometer voltage, E, in Eq. 3.1 with a temperature-compensated voltage, $\widehat{E}$, which is the voltage that would have been measured at the same effective velocity, V_e, if the ambient temperature were the compensation temperature, $\widehat{T}$, rather than the actual temperature, T. This correction is accomplished using the fit parameters $\widehat{A}$, $\widehat{B}$, and $\widehat{n}$ of Eq. 3.6 that give $C_T\left(V_e\right)$ at a particular temperature.

Calibration takes place while the probe is located in the uniform-velocity freestream, where the wind-fixed W component of the flow velocity is zero and the U component is measured using a Pitot-static tube. The calibration procedure consists of first making several calibration tests during which the flow velocity is varied from low to high speed for a series of crosswire probe angles, θ. These sweeps enable the determination of the yaw sensitivity coefficient, k^2, which is assumed independent of temperature. Then, the wind tunnel undergoes a heat-up period during which it is operated at a high speed. Immediately following the heat-up period, a final "high-temperature" calibration run is conducted by varying the velocity from high to low speed in an effort to maintain the elevated temperature. The difference between the effects of relatively high and low temperatures on the anemometer voltages as a function of velocity is used to generate the temperature-compensation coefficients. Finally, King's Law fit parameters A, B, and n are generated for the temperature-compensated voltages spanning all of the calibration sweeps. These operations result in the characterization of each wire via a series of best fit parameters, namely the yaw sensitivity coefficient k^2, temperature compensation coefficients $\widehat{A}$, $\widehat{B}$, and $\widehat{n}$, and the coefficients relating the temperature-compensated voltages to the effective velocities A, B, and n.

3.2 Calibration Data Collection

In practice at the KSWT, calibration data is collected in a total of four velocity sweeps as described in Table 3.1. The four velocity sweeps are nominally between freestream speeds of $U_\infty = 1$ m/s and 24 m/s across a number of setpoints. The setpoints are indexed as $j = 1...J$, with J typically equal to 13. Three "cold" sweeps are conducted at low temperature at $\theta = \pm 15°$ and 0° and provide directional calibration data to determine k^2, the yaw sensitivity coefficient. Hotwire probe angles are adjusted using a machined fixture that enables accurate and rapid angle setting. In the interest of efficient operation, the set points for these three sweeps are specified as wind-tunnel fan rotation speeds rather than specific velocities with tight tolerances. A final "hot" sweep at $\theta = 0°$ and an elevated temperature, usually about 5° higher, provides temperature compensation data for set points specified by the actual velocities reached in sweep 3 rather than the fan rotation speed. Velocity setpoints are used for sweep 4 because the elevated temperature can lead to notably different velocities for the same fan rotation speeds used in sweeps 1–3. Because the wind tunnel temperature generally increases throughout the day of operation, performing the low-temperature runs at the beginning of a day ensures they represent the coldest operating temperature of the day. The temperature of the high-temperature run is selected to be representative of the anticipated high temperature. After the high-temperature run is completed, a short period of cooling allows the tunnel temperature to fall before operations proceed at lower speeds. Then, throughout the day, the temperature climbs again towards the high-temperature morning calibration run.

As previously mentioned, each of the "cold" velocity sweep setpoints are governed by specifying the wind-tunnel fan rotations speeds while the "hot" sweep setpoints attempt to match those of the "cold" sweep taken at the same probe angle, $\theta = 0°$. The temperature compensation ap-

Table 3.1: Calibration sweeps cases

Sweep Index	θ	Temperature
$i = 1$	$+15°$	cold
$i = 2$	$-15°$	cold
$i = 3$	$0°$	cold
$i = 4$	$0°$	hot

proach requires measurements at two temperatures but equal velocity. However, for an intended constant-velocity setpoint across all sweeps, the actual velocity can vary on the order of 0.1 m/s. Following the approach by White [3], hotwire voltages obtained in each sweep are interpolated to their expected values at nominal freestream velocities corresponding to each setpoint. The nominal velocities used for this interpolation are chosen as those collected in calibration run 3, as this particular sweep is used in both the flow-direction and temperature-compensation portions of the calibration data analysis sequence. Because the differences between the nominal and actual velocities are very small, a linear interpolation is adequate. The interpolated voltages are found using

$$\widetilde{E}_{(i,j)} = E_{(i,j)} + \frac{E_{(i,j+1)} - E_{(i,j)}}{U_{\infty(i,j+1)} - U_{\infty(i,j)}} \left(U_{\infty(3,j)} - U_{\infty(i,j)}\right), \tag{3.7}$$

where j is the velocity setpoint, i is the calibration sweep index defined in Table 3.1, and $\widetilde{E}$ is the set of voltages interpolated to the run-3 freestream velocities, $U_{\infty(3,j)}$, that henceforth will be designated simply $U_{\infty(j)}$. For $j = J$, a backwards interpolation is used.

3.3 Calibration Data Analysis

Once calibration data is collected through the four velocity sweeps listed in Table 3.1, a series of nonlinear regression analyses are executed to generate the parameters that describe the calibration of each of the slanted hotwire elements of the cross-style probe. Once again, k^2 describes a wire's directional sensitivity and is assumed to be independent of temperature variation; $\widehat{A}$, $\widehat{B}$, and $\widehat{n}$ correct the measured voltage for temperature drift; and A, B, and n relate temperature-compensated voltage to the effective velocity.

Ambient temperature drifts within 1°C during the flow-angle calibration, coupling the effects of temperature and directional effects on the anemometer voltage. Though k^2 is independent of temperature, this coupling requires k^2 to be addressed in a coupled way with the other six calibration parameters. The calibration is centered around the relationship between the effective velocity and the flow characteristics (flow angle, magnitude, and temperature), and, as k^2 is necessary in the calculation of the effective velocity, requires the nonlinear regression steps responsible for generating the other six calibration coefficients to be repeated for several values of k^2 within its expected range. According to a study by Bruun and Tropea [4], values of k^2 for a single-inclined Dantec type 55P12 probe were found in the approximate range $-0.1 \leq k^2 \leq 0.04$. Taken individually, the Dantec type 55P61 probe's inclined wire geometries are very similar to the 55P12 probe, therefore bounds on the directional sensitivity parameter were generously chosen such that $-0.2 \leq k^2 \leq 0.2$ to accommodate the roles other factors might play in the magnitude of the range (e.g., prong effects, geometric differences, etc.).

For each of the prospective k^2 values, several data analysis steps are completed for each slanted hotwire element. First, the probe geometry is used to convert the $U_{\infty(j)}$ velocity setpoints to effective velocities, $V_{e(i,j)}$, using Eqs. 3.1– 3.4. The effective velocities are indexed both by freestream velocity setpoint, j, and velocity sweep, i, to include the effects of different probe orientations for each run. For simplicity of demonstration, rather than explicitly calculating the velocity components normal and tangential to the wire, the effective velocity can be calculated using Hinze's [9] formulation (Eq. 1.7)

$$V_{e(i,j)} = U_{\infty(j)} \left(\cos^2 \alpha_i + k^2 \sin^2 \alpha_i\right)^{1/2} \quad \text{where} \quad \alpha_i = \bar{\alpha} + \theta_i. \tag{3.8}$$

The measured hotwire voltages from all four sweeps are plotted in Figure 3.2. If the ambient temperature was invariant across the four sweeps, the voltage curves would all be expected to collapse onto a single curve which could then be modeled by King's Law as a function of the effective velocity. The temperature is known to vary throughout the calibration, therefore the temperature calibration must be conducted first in order to decouple the effects of temperature and flow angle by adjusting all of the voltages to a constant temperature.

First, prospective temperature compensation data are generated. The temperature compensation coefficient $C_T(V_e)$ is assumed to depend only on V_e. Because data from calibration runs $i = 3$ and $i = 4$ share the same probe angle, $\theta = 0$, they have equal effective velocities $V_{e(3,j)} = V_{e(4,j)}$ and can be used to generate $C_T(V_e)$ data. The coefficients are calculated using

$$C_T(V_{e(3,j)}) = \frac{\widetilde{E}^2_{(4,j)} - \widetilde{E}^2_{(3,j)}}{T_{(4,j)} - T_{(3,j)}} = -\widehat{A} - \widehat{B}\, V_{e(3,j)}^{1/\widehat{n}} \tag{3.9}$$

and are fit using a nonlinear least-squares minimization technique that yields coefficients $\widehat{A}$, $\widehat{B}$, and $\hat{n}$. An example fit is shown in Figure 3.3. Then, using these coefficients, temperature-compensated voltages are generated for all of the calibration data points using

$$\widehat{E}^2_{(i,j)} = \widetilde{E}^2_{(i,j)} + C_T(V_{e(i,j)}) \left(\widehat{T} - T_{(i,j)}\right). \tag{3.10}$$

In principle, the “compensation temperature,” $\widehat{T}$, to which all the voltage data are adjusted, could be any value. For consistency in practice, the the highest-speed data point of the third calibration run is used for this purpose, $\widehat{T} = T_{(3,J)}$, as this is usually the highest temperature of the “cold” calibration runs and is most typical of a day’s mean operating temperature.

Finally, using the temperature-compensated voltages, a nonlinear fit of the data from all four calibration runs to the King’s Law form is performed using

$$V_{e(i,j)} = \left(A + B\, \widehat{E}^2_{(i,j)}\right)^n. \tag{3.11}$$

An example fit is shown in Figure 3.4. Data from each of the four calibration runs effectively collapse onto a single curve which is well described by King’s Law. This final fit is the last step of a tentative calibration for a specified value of k^2 and completes the set of tentative temperature-compensated calibration coefficients for each slanted wire. The data fit to Eq. 3.11 also generates a χ^2 value that characterizes the goodness-of-fit that results from the originally specified k^2 value. Again, the value of k^2 is specified at the outset of the preceding steps and, rather than using a brute force method to navigate the parameter range, a least-squares minimization technique governed by the χ^2 value was employed to investigate the k^2 range with an initial condition of $k^2 = 0$. Ultimately, the k^2 value that minimizes χ^2 for a particular wire is selected to represent the calibration output, along with the associated $\widehat{A}$, $\widehat{B}$, and $\widehat{n}$, and A, B, and n values for that same wire.

3.4 Calibration Parameter Uncertainty Estimation

The sensors used in the experiment have associated uncertainties in their measurements, each of which are listed in Table 3.2. In order to observe the correlation between velocity component estimate uncertainties, a Monte Carlo simulation of M, typically 1000, sensor measurement realizations is employed during calibration to statistically determine a series of calibration coefficients and their corresponding covariance matrix. The method described in Section 3.3 is executed for each single-inclined hotwire for each realization of the measured conditions p, q, and T, as well as probe angle θ. Each realization yields coupled coefficients k^2, $\widehat{A}$, $\widehat{B}$, $\widehat{n}$, A, B, and n. The results of the Monte Carlo simulation are vectors of length M corresponding to each of the calibration coefficients, namely $\boldsymbol{k}$, $\widehat{\boldsymbol{A}}$, $\widehat{\boldsymbol{B}}$, $\widehat{\boldsymbol{n}}$, $\boldsymbol{A}$, $\boldsymbol{B}$, and $\boldsymbol{n}$.

Next, the series of calibration coefficients which best models the system is found by calculating the means of each of the coefficients vectors. The covariance matrix, ρ, relating all of the coefficients can also be calculated using

$$\rho_{i,j} = \sum_{m=1}^{M} \frac{\left(X_{i,m} - \bar{\boldsymbol{X}}_{\boldsymbol{i}}\right)\left(X_{j,m} - \bar{\boldsymbol{X}}_{\boldsymbol{j}}\right)}{M-1}, \tag{3.12}$$

where $\boldsymbol{X} = \left[\widehat{\boldsymbol{A}}, \widehat{\boldsymbol{B}}, \widehat{\boldsymbol{n}}, \boldsymbol{A}, \boldsymbol{B}, \boldsymbol{k}, \boldsymbol{n}\right]$, over-barred quantities denote the vector mean, and subscripts $i,\ j = 1, 2, ..., 7$.

An example Monte Carlo simulation was conducted for 1000 iterations. Figure 3.5 demonstrates the convergence of the mean k^2 parameters for each wire to their own respective values as the simulation progresses.

Table 3.2: Calibration input measurement uncertainties

Variable	**Measurement Uncertainty,** $\pm 3\sigma$
Static pressure, p	$\pm 0.05\%$ value
Dynamic pressure, q	$\pm 0.05\%$ value
Temperature, T	$\pm 0.15°$ C
Probe angle, θ	$\pm 0.1°$ about $\theta = 0°$ $\pm 0.2°$ otherwise

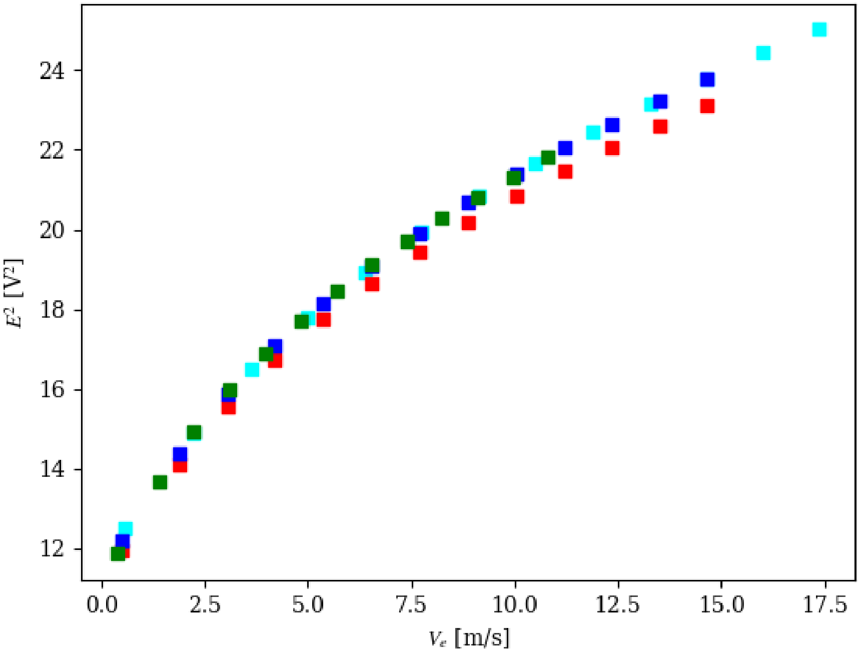

(a) Hotwire 1 directional calibration fit.

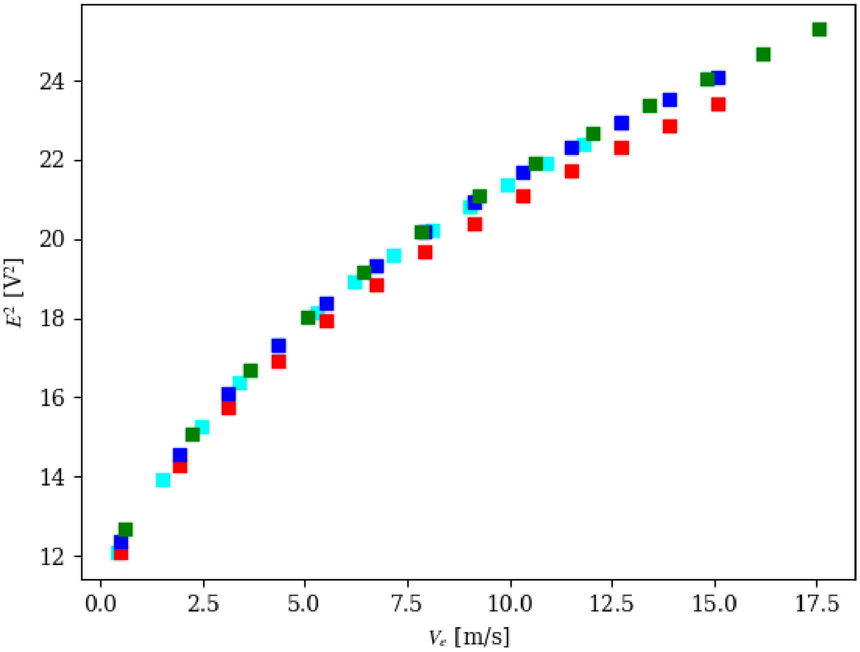

(b) Hotwire 2 directional calibration fit.

Figure 3.2: Raw directional calibration data as a function of effective velocity. Data points correspond to raw (E^2, V_e) pairs, where the temperature is not constant and colors green, cyan, blue, and red correspond to data collected from sweep cases 1–4, respectively.

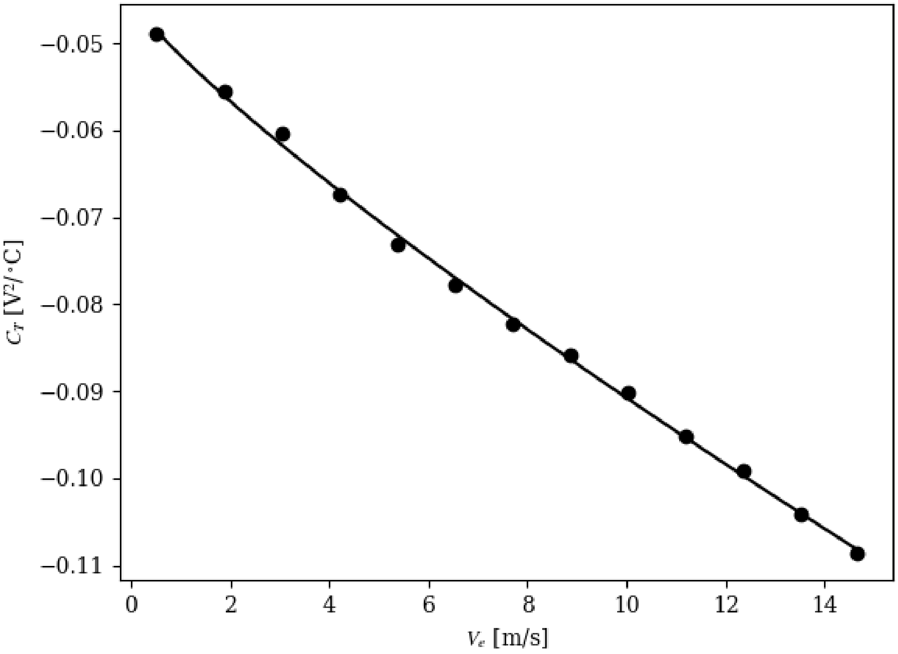

(a) Hotwire 1 temperature calibration fit.

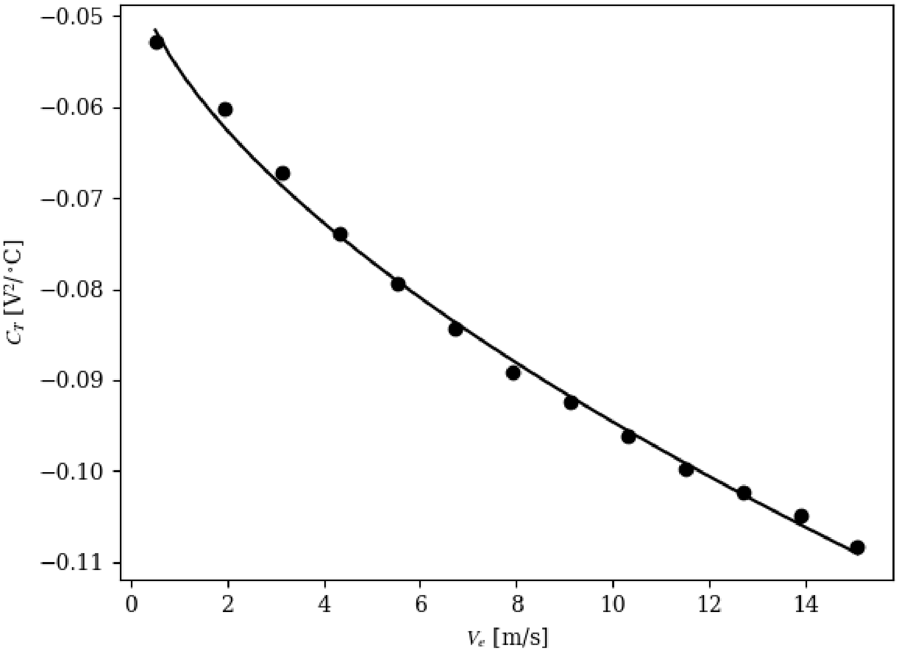

(b) Hotwire 2 temperature calibration fit.

Figure 3.3: Temperature compensation coefficient as a function of effective velocity. Data points correspond to calculated (C_T, V_e) pairs while the line corresponds to the King's Law fit using the respective wire's best-fit parameters $\widehat{A}$, $\widehat{B}$, and $\widehat{n}$ in Eq. 3.9.

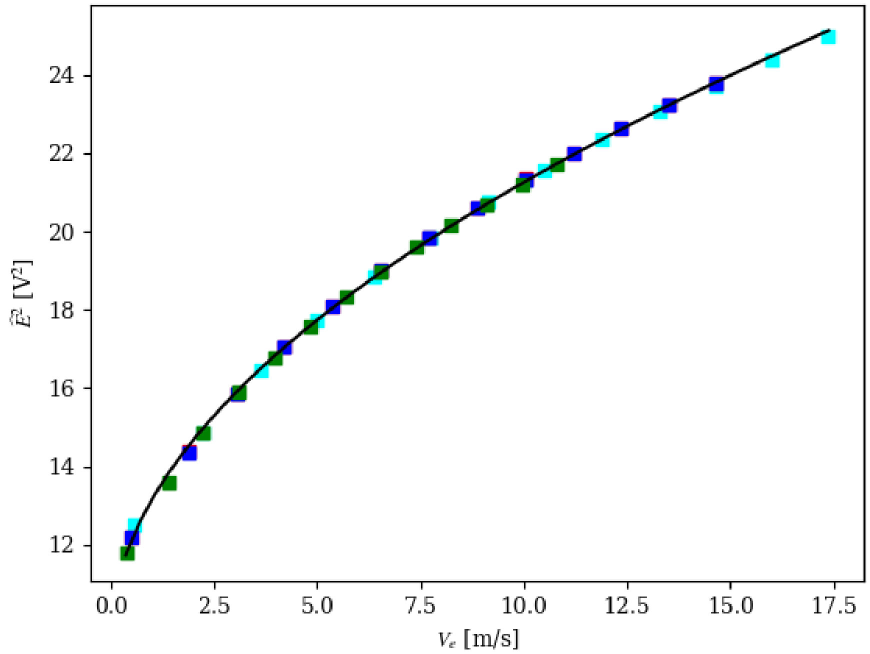

(a) Hotwire 1 directional calibration fit.

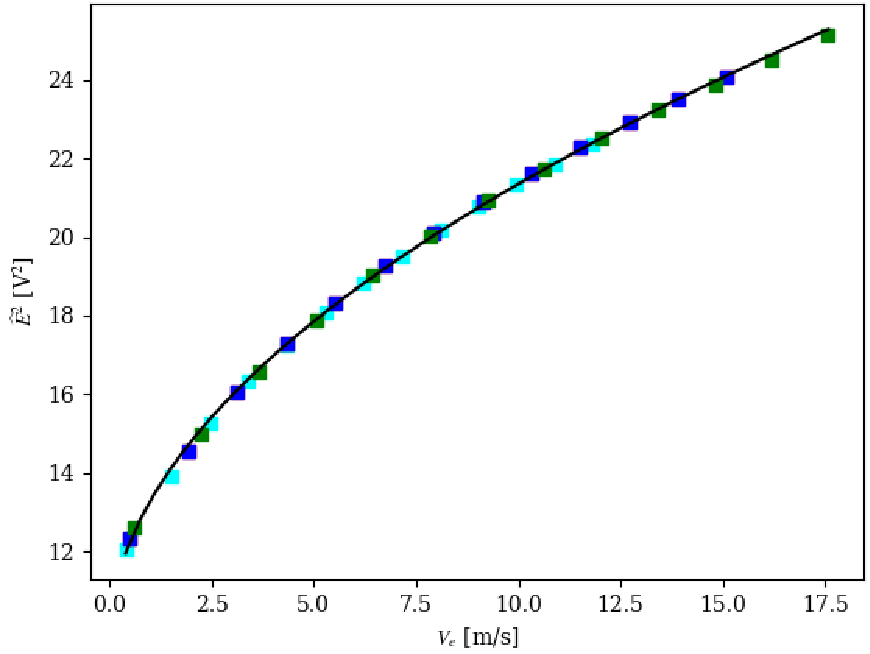

(b) Hotwire 2 directional calibration fit.

Figure 3.4: Directional calibration fit as a function of effective velocity. Data points correspond to calculated ($\widehat{E}^2$, V_e) pairs, where the colors green, cyan, blue, and red correspond to data collected from sweep cases 1–4, respectively. Cases 3 and 4 are hard to distinguish as they lie directly on top of one another. The solid line corresponds to the King's Law fit using the respective wire's best-fit parameters A, B, k^2 and n in Eq. 3.11.

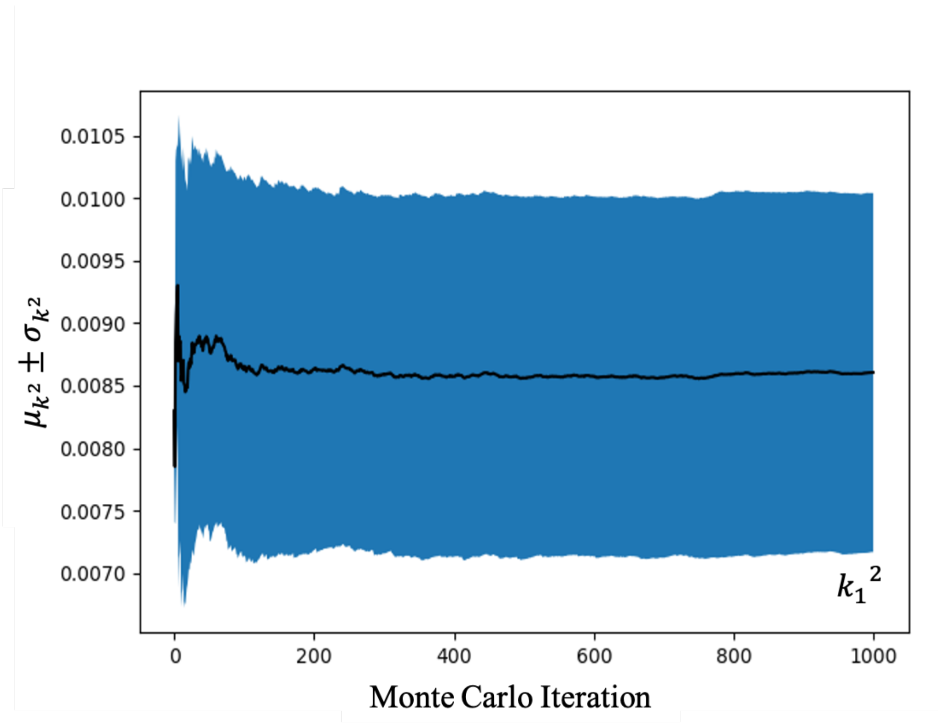

(a) Hotwire 1 k^2 convergence.

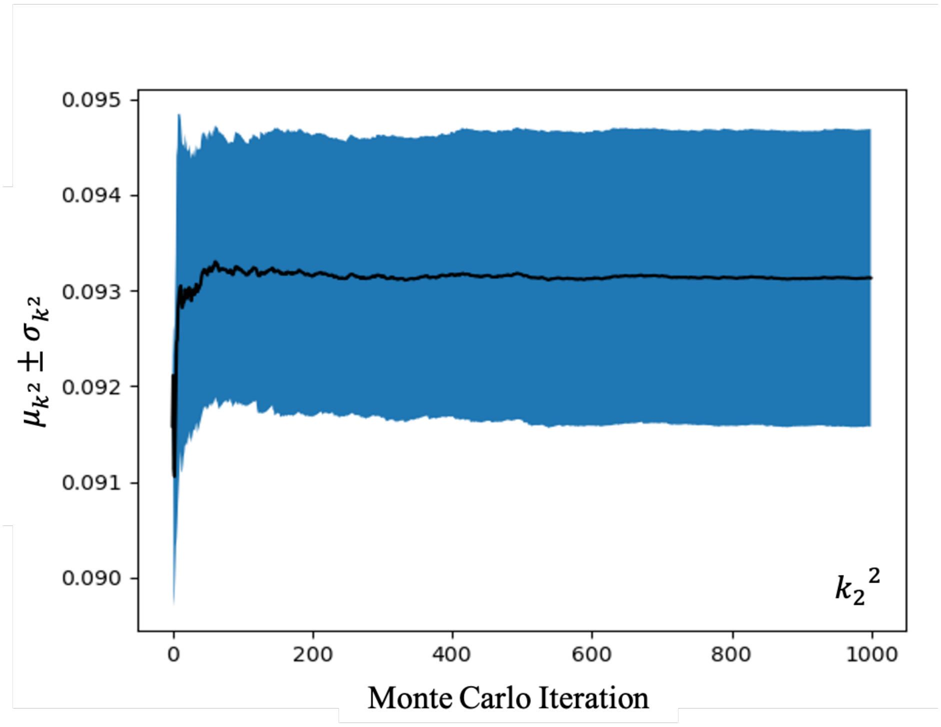

(b) Hotwire 2 k^2 convergence.

Figure 3.5: Demonstration of k^2 parameter convergence through Monte Carlo simulation iterations. The solid line represents the mean k^2 over all iterations up to the current iteration while the blue shaded region represents the standard deviation.

4. VELOCITY COMPONENTIZATION

The calibration technique described in Chapter 3 yields a set of most-probable coefficients and a covariance matrix which quantifies the relationship between their uncertainties for each single-inclined wire. The coefficients include the directional sensitivity parameter, k^2; voltage compensation coefficients for temperature variation, $\widehat{A}$, $\widehat{B}$, and $\widehat{n}$; and A, B, and n, which relate the temperature compensated voltages to the effective velocity. For a measurement point including the ambient temperature and both slantwire voltages, effective velocities for each of the wires can be determined using Eqs. 3.9 and 3.10 with the wires' respective coefficients using the technique developed by White [3]. Then, following the method detailed by Bruun [2], the effective velocities can be related using a modified sum and difference method to determine the two wind-frame velocity components; the streamwise, U, component is proportional to the sum of the effective velocities while the spanwise, W, component is proportional to the difference.

In each measurement of the velocity components, there exist both measurement uncertainty and model-form error. Because the calibration coefficients are determined using a restricted range of probe angles, the effects of model-form error arise in velocity component measurements as a function of the flow angle and grow with the extent to which realistic conditions are extrapolated from the calibration's simulated conditions. An *a priori* understanding of the model-form error trends can inform potential methods of component-wise corrections. On the other hand, the correlation of the calibration parameter uncertainties cascades into the U and W component uncertainties, which can be quantified *a posteriori* using a Monte Carlo simulation.

This chapter details the conversion from effective velocities to wind-frame velocity components and the calculation of the measurement error and uncertainty. The methods defined here will be applied to experimental data in the chapters to follow.

4.1 Velocity Component Calculation

For a single experimental data point taken in a homogeneous flow-field, each single-inclined hotwire senses an effective velocity which can be estimated using the measured ambient temperature and that wire's anemometer voltage and calibration coefficients using

$$V_{ei} = \left(A_i + B_i\ \widehat{E}_i^2\right)^{n_i}, \tag{4.1}$$

where i is now defined as the index of the single-inclined hotwire ($i = 1, 2$) and the temperature-compensated voltage explicitly written in terms of its best-fit coefficients is

$$\widehat{E}_i^2 = E_i^2 + \left(\widehat{A}_i + \widehat{B}_i\left(V_{ei}\right)^{1/\widehat{n}_i}\right)\left(T - \hat{T}\right). \tag{4.2}$$

As can be observed in Eqs. 4.1 and 4.2, the existence of the effective velocity in the definition of the temperature-compensated voltage necessitates the use of an iterative method for each wire. White [3] defined an iterative method for single-normal hotwires which can be used for single-inclined wires when the principle flow magnitude is replaced with the effective velocity. First, an initial estimate of V_e is generated by plugging the raw hotwire voltage, E, into Eq. 4.1 in the place of the currently unknown temperature-compensated voltage, $\widehat{E}$. With the resulting estimate of V_e, the first iteration of the temperature compensated voltage can be calculated using Eq. 4.2. The output compensated voltage is then plugged back into Eq. 4.1 to find an updated estimate of the effective velocity. The process is repeated until the difference between iterations of V_e is much less than the effective compensated velocity uncertainty. In this analysis, the stopping criteria has been set to a constant value of 10^{-4} m/s, which is much smaller than the velocity uncertainty. This procedure is applied to find effective velocity estimates for both single-inclined hotwires.

Bruun [2] provides a method of calculating the wind-frame U and W velocity components for cross-style hotwires under the assumption that the plane onto which the projections of the cross-style probe's sensing elements form the characteristic "X" is coplanar with the wind-fixed x-z

plane. For two-dimensional flows in which the wire-fixed $V_B = 0$ and wind-fixed $V = 0$, the relationship between the wire- and wind-frame velocity components from Eqs. 3.3 and 3.4 is

$$\begin{aligned} V_{Ni} &= U\,\cos\alpha_i - W\,\sin\alpha_i \quad \text{and} \\ V_{Ti} &= U\,\sin\alpha_i + W\,\cos\alpha_i . \end{aligned}$$

Also recalling Jorgensen's equation for effective velocity with $V_B = 0$

$$V_{ei}^2 = V_{Ni}^2 + k_i^2\, V_{Ti}^2 ,$$

expressions for V_N and V_T can be inserted, yielding

$$V_{ei}^2 = \left(U\,\cos\alpha_i - W\,\sin\alpha_i\right)^2 + k_i^2\,\left(U\,\sin\alpha_i + W\,\cos\alpha_i\right)^2 . \tag{4.3}$$

During calibration in the steady freestream, the wind frame velocity components can be described by a mean and a fluctuating component, the mean transverse component of which is assumed negligibly small. The following assumptions are made:

$$\begin{gathered} U = \bar{U} + u, \quad W = \bar{W} + w \\ u, w \ll \bar{U} \\ \bar{W} = 0, \end{gathered}$$

where barred quantities denote mean quantities and lowercase quantities are fluctuating components. Employing these assumptions and cancelling second order terms in the fluctuating components, Eq. 4.3 reduces to

$$\begin{gathered} {V_{ei}}^2 = \left(\bar{U}^2 + 2\bar{U}u\right)\left(\cos^2\alpha_i + {k_i}^2 \sin^2\alpha_i\right) + \\ + 2\bar{U}w\cos\alpha_i\sin\alpha_i\left({k_i}^2 - 1\right) \end{gathered} \tag{4.4}$$

The effective velocity estimated by a single-inclined hotwire is found by taking the first order terms of the series expansion of Eq. 4.4, assuming the form

$$V_{ei} = F_i \left[\bar{U} + u + wG_i\right], \tag{4.5}$$

where

$$F_i = \left(\cos^2\alpha_i + {k_i}^2 \sin^2\alpha_i\right)^{1/2} \quad \text{and}$$
$$G_i = \frac{\cos\alpha_i \sin\alpha_i \left({k_i}^2 - 1\right)}{\cos^2\alpha_i + {k_i}^2 \sin^2\alpha_i}.$$

For cross-style hotwires in two-dimensional flows, the wind frame U and W components are determined using

$$U = \frac{\frac{V_{e2}}{F_2}G_1 - \frac{V_{e1}}{F_1}G_2}{G_1 - G_2} \quad \text{and} \tag{4.6}$$

$$W = \frac{\frac{V_{e1}}{F_1} - \frac{V_{e2}}{F_2}}{G_1 - G_2}. \tag{4.7}$$

4.2 Velocity Component Uncertainties

Velocity component estimates calculated in Section 4.1 have associated uncertainties that are dependent upon calibration coefficient uncertainties as well as sensor measurement uncertainties in both the ambient temperature and the probe angle. The off-diagonal terms of the calibration coefficient covariance matrix, $\boldsymbol{\rho}$, indicate that the coefficient uncertainties are correlated. Consequently, the velocity component uncertainties are defined statistically using a Monte Carlo simulation of M, typically 1000, coefficient and sensor measurement realizations.

For a single measurement point, sensor measurements of the ambient temperature, probe angle, and two hotwire voltages are collected. The two hotwire voltages, E_1 and E_2, are assumed to be known exactly while the temperature, T, and angle, θ, have associated sensor uncertainties as defined in Table 3.2. Realizations of T and θ are randomly generated by adding a Gaussian perturbation to the respective sensor measurement

$$\begin{aligned} T^* &= T + \mathrm{gauss}\left(0,\ \sigma_T\right) && (4.8) \\ \theta^* &= \theta + \mathrm{gauss}\left(0,\ \sigma_\theta\right), && (4.9) \end{aligned}$$

where starred quantities represent realizations and the Gaussian perturbations are characterized by a zero mean and standard deviation of the sensor measurements, σ. Alternatively, the correlation between the calibration coefficients does not permit independent, random generation of realizations for each coefficient. Rather, a properly correlated perturbation governed by the calibration coefficient covariance matrix, $\boldsymbol{\rho}$, is added to the mean calibration coefficients found in Chapter 3. This operation is performed using Cholesky decomposition, which, for a known covariance matrix, returns a lower triangular matrix, $\boldsymbol{L}$, that can be multiplied by a random, unit-variance vector, $\boldsymbol{P}$, to generate a correlated perturbation. Thus the set of coefficients' realization is calculated using

$$\boldsymbol{X}^* = \boldsymbol{X} + \boldsymbol{L}\left(\boldsymbol{\rho}\right)\, \boldsymbol{P} \quad \text{and} \quad P_i = \mathrm{gauss}\left(0,\ 1\right), \tag{4.10}$$

where $\boldsymbol{X} = \left[\widehat{A}, \widehat{B}, \widehat{n}, A, B, k^2, n\right]$ and $i = 1, 2, ..., 7$.

For each set of realizations (T^*, θ^*, and $\boldsymbol{X}^*$) in addition to the measured voltages (E_1, E_2), wind-frame velocity components are calculated using the method described in Section 4.1. This yields M estimates of both U and W, whose means are the best estimates of the two respective components. The covariance matrix, $\boldsymbol{\rho_{UW}}$, between the M estimates of U and W demonstrates the correlation between the two components' uncertainties in the wind-fixed frame. The range of possible (U, W) candidate pairs can be described as an ellipse whose semi-major and minor axes lie along the principal directions of $\boldsymbol{\rho_{UW}}$ with lengths equal to the square root of the maximum and minimum principal values, respectively.

4.3 Velocity Component Error

Separate from their uncertainties, velocity component estimates are subject to calibration model form error. Model form error arises due to the fact that calibration is tailored to a small angle range relative to what could potentially be observed in experiments. Measurements within the calibration range can be measured with great accuracy while error increases with the extent to which realistic conditions are extrapolated from the calibration's simulated conditions. The error in the wind-frame velocity components is a consequence of error in the King's Law effective velocity fits for each single-inclined hotwire. These errors in effective velocity can be quantified for each hotwire during measurements in which the flow magnitude and angle are known. Using the relationship intended for calibration in Eq. 3.1 and simplifying for two-dimensional flows, the effective velocity error corresponding to the i^{th} hotwire ($i = 1,\ 2$) is

$$\epsilon_i = \left(A_i + B_i\, E_i^2\right)_i^n - \widetilde{V}\left(\cos^2\alpha + k_i^2 \sin^2\alpha\right)^{1/2} \quad \text{with} \quad \alpha_i = \bar{\alpha_i} + \theta, \tag{4.11}$$

where $\widetilde{V}$ is the principle flow magnitude and, for the simplifying assumptions employed, θ is the both the flow and probe angle. These errors in the effective velocities are compounded in the calculation of U and W velocity components.

5. FREESTREAM EXPERIMENT RESULTS

To quantify the accuracy of the proposed calibration procedure, a series of experiments are conducted in the freestream to record the crosswire response to various simulated flow angles and velocity magnitudes. In the freestream, the principle flow is oriented along the x direction and the velocity components are known to be $U = U_\infty$ and $W = 0$. Velocity magnitude, $\widetilde{V}$, is controlled by adjusting the freestream velocity as measured by the Pitot probe. Because $W = 0$ in the freestream, the flow angle is simulated by adjusting the probe's pitch angle, θ, relative to the freestream direction.

For a given ($\widetilde{V}$, θ) combination, the two single-inclined hotwire voltages, E_1 and E_2, and the ambient temperature, T, are found by taking the mean of the respective sensor measurements collected over a two-second acquisition period. Though the probe is set to a known arbitrary angle, θ, during analysis the probe angle is treated to be 0° and the mean sensor measurements are used to obtain estimates of the so-called "pseudo" U' and W' velocity components following the method explained in Section 4.1. The U' and W' velocity components are found in the probe-fixed frame during these freestream experiments, but they are equivalent to the U and W components that would be measured in the wind-fixed frame during an experiment in which the probe angle is actually set to 0° and there exists a measured flow angle, $\theta_m = \tan^{-1}(W/U)$, that is the same as the simulation probe angle, θ. The correlated uncertainties in the simulated velocity components can be determined using the Monte Carlo approach detailed in Section 4.2. Because the flow conditions are well known during these freestream experiments, a comparison between measured and expected hotwire effective velocities using Eq. 4.11 appropriately demonstrates the model-form error for each wire.

Two sets of calibration and experimental data are presented to demonstrate the velocity componentization with associated uncertainty and error with respect to both temperature and flow angle. For each set, the calibration was performed and the temperature was allowed to decrease prior to conducting the freestream experiments.

5.1 Experiment 1

A calibration was conducted with sweeps characterized by probe angles $\theta = [15.9°, -15.5°, 0°, 0°]$, temperature within the range $T = [20.9°\text{C}, 28.7°\text{C}]$, and compensation temperature $\widehat{T} = 22.5°\text{C}$. The coefficients returned from the calibration method described in Chapter 3 are tabulated below in Table 5.1. Figures 3.3 and 3.4 are generated using this dataset. The temperature calibration coefficients are notably different between the two hotwires. This could, in part, be due to slight differences in thermal properties or geometries between the two wires, however it is more likely due to the strong correlation between the individual wires' $\widetilde{A}$, $\widetilde{B}$, and $\widetilde{n}$ temperature calibration coefficients. For an arbitrary choice of $\widetilde{n}$, parameters $\widetilde{A}$ and $\widetilde{B}$ can adjust to result in an acceptable fit. The values of the temperature compensation parameters themselves are therefore relatively unimportant, but their values relative to one another are critical.

Table 5.1: Freestream experiment 1 calibration coefficients.

	Wire 1	**Wire 2**
$\boldsymbol{A}$	-1.848	-1.789
$\boldsymbol{B}$	0.222	0.215
$\boldsymbol{k^2}$	0.004	0.087
$\boldsymbol{n}$	2.184	2.220
$\widehat{\boldsymbol{A}}$	0.042	0.023
$\widehat{\boldsymbol{B}}$	0.008	0.028
$\widehat{\boldsymbol{n}}$	1.268	2.461

Figure 5.1 shows the results of the freestream experiment for a set of simulated flow angles and magnitudes described by $-35° \leq \theta \leq 35°$ and $2\,\text{m/s} \leq U_\infty \leq 14\,\text{m/s}$. The temperature during the measurements ranged from approximately 22.4°C to 23.1°C, well within the bounds of the temperature calibration. In Figure 5.1, the measured points are depicted by points while the expected conditions are represented by the intersections of the dotted lines, where the radial lines

indicate the intended flow angle and the arc lines indicate the intended velocity magnitude. The measured and expected values of the U and W components are in good agreement for $-20^\circ \leq \theta \leq 20^\circ$ and $U_\infty \geq 4\,\mathrm{m/s}$. This indicates that the calibration can afford extrapolation slightly beyond its angle bounds, however large extrapolations in flow angle from the calibration conditions can result in large deviations between measured quantities and the true flow conditions.

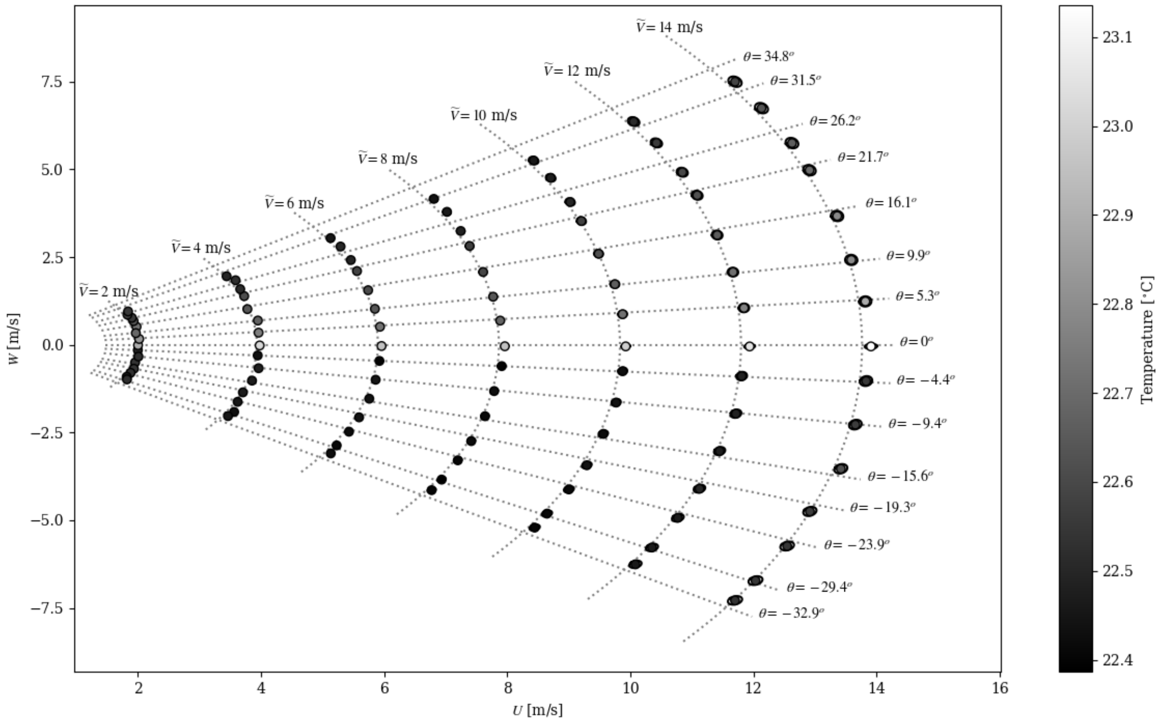

Figure 5.1: Freestream simulation and measurements of various flow angle and velocity magnitude combinations. Axes correspond to U and W component estimates, dotted arc lines denote the expected magnitude of the velocity vector estimate, and dotted radial lines denote the expected flow angle. Correlated velocity component uncertainties are represented by ellipses with semi-major and semi-minor axes corresponding to the 3σ uncertainty bounds of a Monte Carlo simulation. Point colors correspond to the mean ambient temperature during their collection.

The uncertainty in each measurement is calculated using the Monte Carlo-based method defined in Section 4.2 and the resulting 3σ uncertainty ellipses are included in Figure 5.1. The semi-major and minor axes of the ellipses are oriented along the principal axes of the velocity component covariance matrix for each measurement point. The rotation angle from the x- and

z-axes to the principal axes of each ellipse is shown as a function of the flow angle and velocity magnitude in Figure 5.2. For $\widetilde{V} \geq 4$ m/s, the rotation angle is linear with the intended flow angle with an approximately unit slope and an intercept of $-8°$. If the offset is assumed negligibly small, this relationship indicates that the semi-major and minor axes of the uncertainty ellipses are approximately oriented along the radial and tangential axes of the U-W component circles in Figure 5.1 and are therefore synonymous with the velocity magnitude and flow angle uncertainties. Using this logic, the flow angle uncertainties and nondimensional velocity magnitude uncertainties are presented in Figures 5.3 and 5.4, respectively. The flow angle 3σ uncertainty is in the range of $\pm 0.55°$ to $\pm 0.65°$ for all angles except $0°$, where the uncertainty is $\pm 0.30°$. The discontinuity at $0°$ is attributed to the fact that the angle-setting uncertainty is only $\pm 0.1°$ about $0°$ as opposed to $\pm 0.2°$ at any other angle, as listed in Table 3.2. The velocity magnitude 3σ uncertainty ranges from approximately $\pm 0.7\%$ at $\widetilde{V} = 14$ m/s to $\pm 1.1\%$ at $\widetilde{V} = 2$ m/s. This range is consistent with the freestream Pitot velocity uncertainty, which was found not to exceed $\pm 1.0\%$ across the $\widetilde{V}$ range.

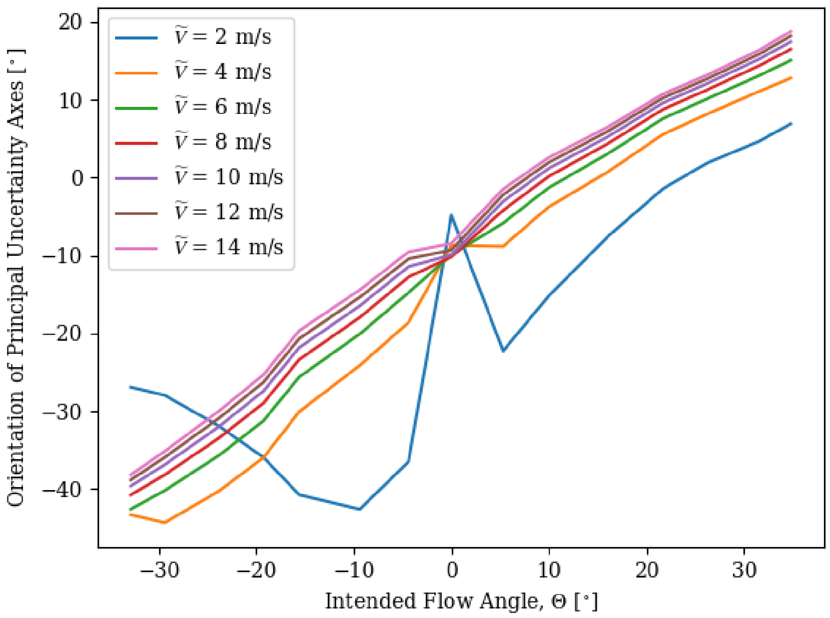

Figure 5.2: Principal uncertainty axes' orientation with respect to the x-z axes. Each colored line corresponds to measurements taken at a constant velocity magnitude for a variety of flow angles.

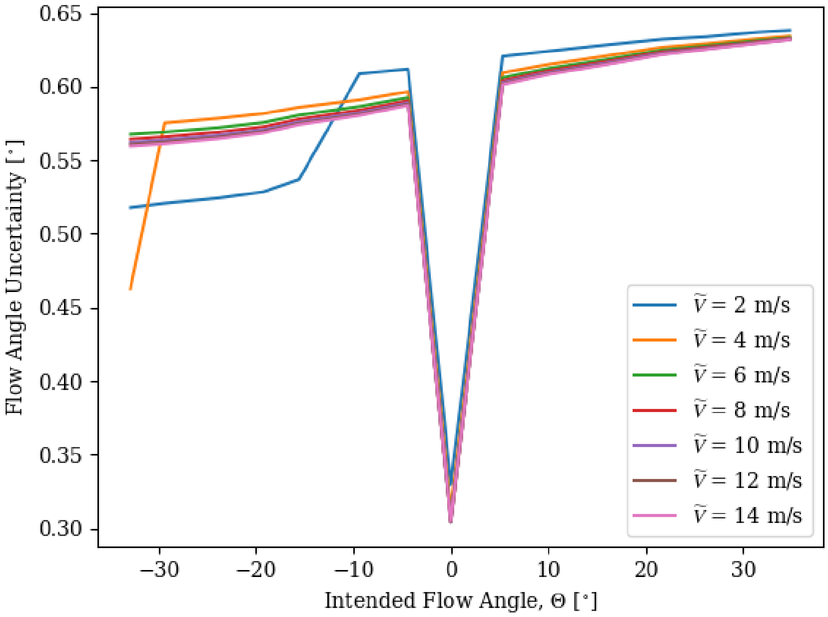

Figure 5.3: Flow angle 3σ uncertainty. Each colored line corresponds to measurements taken at a constant velocity magnitude for a variety of flow angles.

With the maximum uncertainty only reaching $\pm 1.15\%$ of the velocity magnitude, it is evident that model form error is the primary factor in the discrepancy between measured and expected velocity component magnitudes at large flow angles. The model form error is defined on a wire-by-wire basis using the method in Section 4.3. For the first single-inclined wire oriented $\bar{\alpha} = 40°$ with respect to the z axis, Figure 5.5 shows the non-dimensional error in its effective velocity, ϵ_1, as a function of the intended flow angle for a number of velocity magnitudes, $\widetilde{V}$. For $\widetilde{V} \geq 4\,\mathrm{m/s}$, the error is less than 2% for all simulated flow angles in the range $|\theta| \leq 15°$. This indicates that the calibration model selected a yaw sensitivity coefficient, k^2, that accurately predicts the hotwire's response within the range $|\alpha| \leq 55°$. For $|\alpha| \geq 55°$, however, the error exponentially increases to 30% at $\theta = 35°$. Similarly, Figure 5.6 shows non-dimensional error in the effective velocity for the second wire, ϵ_2, inclined $\bar{\alpha} = -40°$ with respect to the z axis. The hotwire's response within the range $|\alpha| \leq 55°$ is also predicted within 2% for $\widetilde{V} \geq 4\,\mathrm{m/s}$. In contrast to the first hotwire, for $|\alpha| \geq 55°$, the second hotwire's error maximum is as low as 8% at $\theta = -35°$. For both

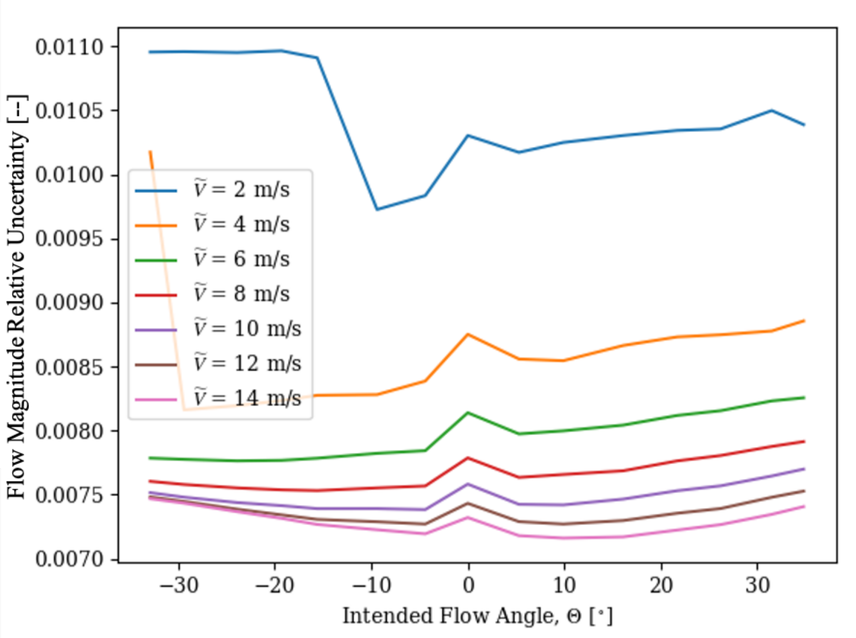

Figure 5.4: Velocity magnitude 3σ uncertainty. Each colored line corresponds to measurements taken at a constant velocity magnitude for a variety of flow angles.

hotwires, $\widetilde{V} = 2$ m/s raises a special case in which the error is considerably higher in a nondimensional sense. The effects of free convection are not known to play a role in measurements taken above approximately 0.2 m/s, therefore the utilization of King's Law calibration model for forced convection is probably not the source of the error because calibration was conducted for velocity magnitudes in excess of 1 m/s. The likely explanation is that the Pitot static tube accuracy during calibration at such low velocities deteriorates and the error is propagated through the calibration and experimental study. For the remainder of this experiment, the case of $\widetilde{V} = 2$ m/s will be excluded from discussion.

Considering the effective velocity error trends for each of the hotwires as depicted in Figures 5.5 and 5.6, the U and W component behavior in Figure 5.1 can be more clearly explained. In Figure 5.1, there is an apparent bias towards more accurate prediction in negative than positive flow angle measurements. For flow angles within the range $|\theta| \leq 15°$, velocity components U and W are accurately predicted because the two hotwire responses (V_{e1} and V_{e2}) both have very small errors. Beyond this range, however, accuracy in U and W predictions are unevenly affected due to

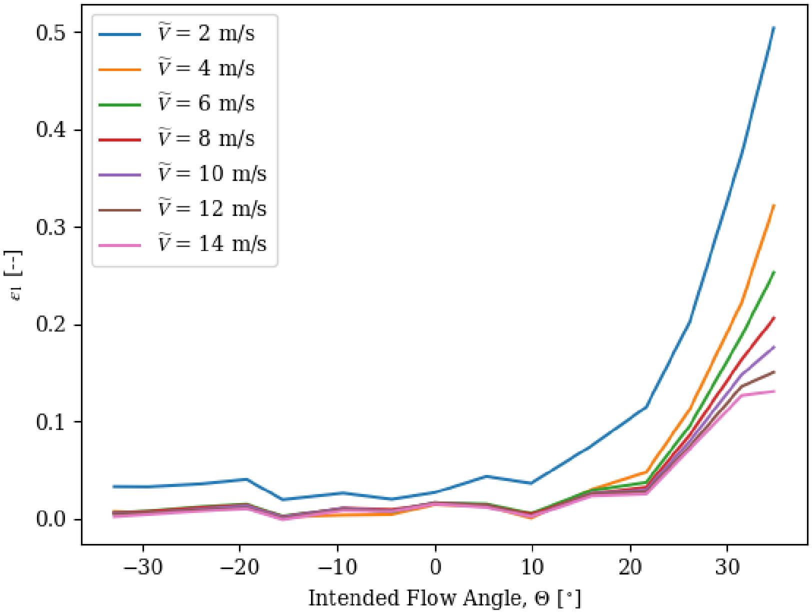

Figure 5.5: Effective velocity error for wire defined by $\bar{\alpha} = 40°$. Each colored line corresponds to measurements taken at a constant velocity magnitude for a variety of flow angles.

the asymmetric error in V_{e1} and V_{e2} as a function of θ. Because the error in hotwire 1's response to large positive flow angles is much larger than the error in hotwire 2's response to large negative flow angles, component measurements are less accurate at the large positive flow angles. The error asymmetry between the two hotwires is interesting and could be a consequence of assuming that the wires' orientations are equally displaced from the z axis by ±40°.

A case study was conducted to observe the effects of the choice of $\bar{\alpha}$ and the calibration θ range on the calibration coefficients and resulting effective velocity error. While $\bar{\alpha}$ is a geometric quantity that can be measured, it is a tedious process and there is still an associated uncertainty in that measurement. It is the intent of this calibration to offer merely an estimate of $\bar{\alpha}$ and allow the coefficients, mainly k^2, to adjust as necessary during calibration to compensate for any error in that estimate. As a reference, the angle between the two wire-normal directions was measured to be approximately 84°, so half-angles $\bar{\alpha} = \pm 40°$ or $\pm 45°$ are physically reasonable estimates. The study considers three cases for choices of $\bar{\alpha}$: two cases in which $\bar{\alpha}$ is fixed to $\pm 40°$ and

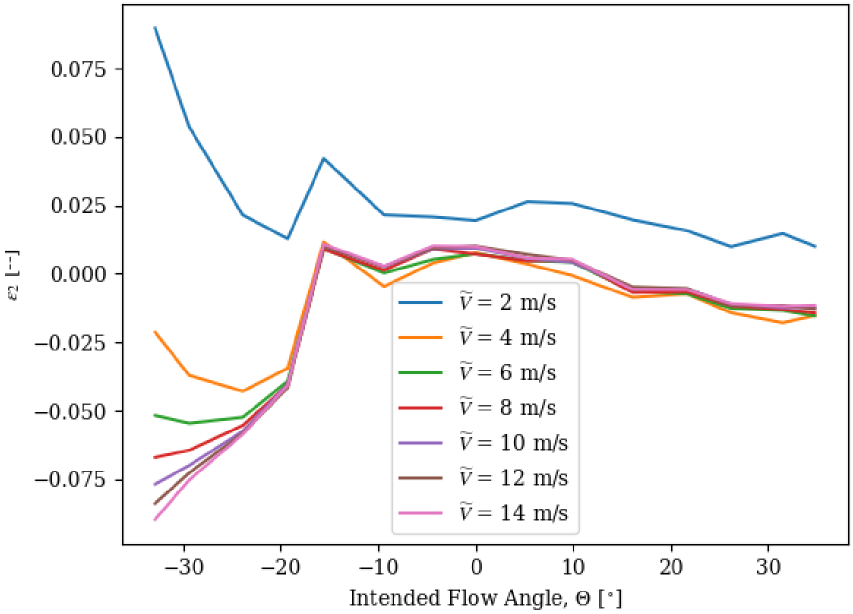

Figure 5.6: Effective velocity error for wire defined by $\bar{\alpha} = -40°$. Each colored line corresponds to measurements taken at a constant velocity magnitude for a variety of flow angles.

$\pm 45°$ and a final case in which $\bar{\alpha}$ is treated as an additional calibration coefficient. The study also considers three different calibration angles for determining the yaw sensitivity coefficients: $\theta = \pm 10°$, $\theta = \pm 15°$, and $\theta = \pm 20°$.

The general approach described in Chapter 3 was applied to determine the best estimates of the calibration coefficients for each of the nine case combinations examined in the study. The coefficients corresponding to the two hotwires for each of the cases are included in Table A.1. The first observation that can be made upon examination of the coefficients is that each hotwire's temperature calibration coefficients ($\widehat{A}$, $\widehat{B}$, and $\widehat{n}$) are independent of both selection of $\bar{\alpha}$ and calibration probe angle, $\pm\theta$. This is an expected result because the temperature calibration is conducted at $\theta = 0°$, whose dataset is constant for each of the three calibration $\pm\theta$ cases. The less trivial observation considers the role the selections of $\bar{\alpha}$ and calibration probe angle play in the determination of the yaw sensitivity coefficient, k^2. The value of k^2 is highly sensitive to changes in both $\bar{\alpha}$ and $\pm\theta$, spanning both positive and negative values as reported by Bruun and

Tropea [4]. There is no conclusive trend relating the effects of calibration $\pm\theta$ on k^2, but it is notable that k^2 is significantly more sensitive to selection of $\bar{\alpha}$ than calibration angle range. With the exception of Case 9, where $\bar{\alpha} = -38.13^\circ$ and $\theta = [\pm 20^\circ,\, 0^\circ]$, the value of k^2 decreases considerably as the absolute value of $\bar{\alpha}$ decreases for a constant calibration $\pm\theta$. Lastly, for Cases 3, 6, and 9 in which $\bar{\alpha}$ is treated as a calibration coefficient, its value which minimizes the error during calibration is approximately $\bar{\alpha} = \pm 36^\circ$. This angle doesn't reflect physical measurements which recorded a value within the range $\pm 40^\circ$ to $\pm 45^\circ$. In these cases, $\bar{\alpha}$ and k^2 are highly coupled in determining the wire's yaw sensitivity blurring comparisons of k^2 with others found in literature. To further compare the various cases, the coefficients corresponding to each case will be applied to the freestream experiment dataset to calculate the velocity components, their uncertainties, and the model form error.

Results corresponding to Cases 1, 4, and 7 where $\bar{\alpha} = \pm 45^\circ$ are considered first in Figures A.1 – A.3, A.10 – A.12, and A.19 – A.21, respectively. For a calibration range of $\pm 10^\circ$, measurements of the U and W components are found to align well with their expected values within the flow angle range $|\theta| \leq 15^\circ$. Outside of these bounds, model form error results in deviation between measured values and actual conditions. Hotwire 1 effective velocity estimates for $\theta < 15^\circ$ are within 2% while error in the range $\theta > 15^\circ$ increases to 20% at $\theta = 35^\circ$. Of the nine cases considered, this is the lowest error recorded for hotwire 1 at large positive angles. Considerable error in hotwire 2 effective velocities are observed for $|\theta| \geq 15^\circ$, reaching up to 5% in the range $\theta > 15^\circ$ and as high as 15% in the range $\theta < 15^\circ$. The preferred behavior of hotwire 2 error would exhibit values under 2% for all positive flow angles. For calibration ranges of $\pm 15^\circ$ and $\pm 20^\circ$, effective velocity error trends are rather consistent with the largest errors encountered for a calibration range of $\pm 20^\circ$. Additionally, the measurements of the U and W components show a decrease in velocity magnitude accuracy as the calibration angle range increases.

Next, results for Cases 2, 5, and 8 where $\bar{\alpha} = \pm 40^\circ$ are included in Figures A.4 – A.6, A.13 – A.15, and A.22 – A.24, respectively. Compared to the results for $\bar{\alpha} = \pm 45^\circ$, U and W component measurements show much better agreement between measured and expected velocity magnitudes across all calibration $\pm\theta$ ranges studied. Additionally, the flow angles within the range $|\theta| \leq 20^\circ$ are well predicted, with the most accurate measurements occurring for a calibration range of $\pm 15^\circ$. For all calibration ranges studied, the effective velocity error in hotwire 1 for $\theta < 15^\circ$ and the error in hotwire 2 for $\theta > -15^\circ$ remain under 2%. Beyond these ranges, hotwire 1 errors can increase rapidly to values greater than 80% at $\theta = 35^\circ$ and hotwire 2 errors can increase to values of $\pm 10\%$ at $\theta = -35^\circ$. The best accuracy of the U and W measurements occurring at a calibration range of $\pm 15^\circ$ is a consequence of this case featuring the smallest errors at the extremities of the flow angle range.

Finally, results for Cases 3, 6, and 9 where $\bar{\alpha}$ was defined during calibration are considered in Figures A.7 – A.9, A.16 – A.18, and A.25 – A.27, respectively. Compared to the results for $\bar{\alpha} = \pm 45^\circ$ and $\pm 40^\circ$, U and W component measurements show the best agreement between measured and expected velocity magnitudes across all calibration $\pm\theta$ ranges studied. For hotwire 1, the effective velocity errors for $\theta \leq 15^\circ$ are consistently smaller than those recorded in Cases 2, 5, and 8, which remained lower than 2% within the same range. However, hotwire 1 errors are much larger in the range $\theta > 15^\circ$ for the present cases than in Cases 2, 5, and 8, extending to as high as 175% in some instances. The error in hotwire 2 shows a similar increase in accuracy within the range $\theta \geq -15^\circ$ as compared to Cases 2, 5, and 8, but a disproportionate change in performance for $\theta < -15^\circ$ with respect to velocity magnitude. Based on these observations, U and W component accuracy seems more dependent upon the hotwires measuring their "regions of confidence" with better accuracy rather than improving performance outside the regions of confidence.

While the hotwire 1 effective velocity errors exhibited in Cases 4 and 7 are some of the lowest observed in the study, their overestimates of the velocity magnitudes occur throughout the expected flow angle range of future experiments and are grounds for dismissal from consideration. The only notable differences between Cases 2, 5, and 8 ($\bar{\alpha} = \pm 40^\circ$) are the two hotwires' effective velocity error distributions, of which Case 5 (calibration range $\theta = \pm 15^\circ$) exhibits the smallest error. Cases 3, 6, and 9 (with $\bar{\alpha}$ defined in calibration) provide the most accurate U and W component measurements of the cases studied, but treating $\bar{\alpha}$ as a calibration coefficient yields results for its value that disagree with physical measurements and greatly increases the complexity of the calibration model for little improvement compared to Cases 1 and 5. Based on the conclusion that better performance within the hotwires' regions of confidence is more important to the component estimate accuracy than the error outside, Case 5 is expected to outperform Case 1. Case 5, described by $\bar{\alpha} = \pm 40°$ and calibration range $\theta = \pm 15°$, is therefore the best calibration option based on the metrics used in this analysis and is the one detailed in Chapter 3.

5.2 Experiment 2

Experiment 1 showcases the accuracy of flow angle and magnitude measurements and was used to decide on calibration parameters of $\bar{\alpha} = \pm 40°$ and probe angle range $\theta = \pm 15°$. While the velocity components were accurately measured for small variations in the ambient temperature near the lower end of the temperature calibration range, it did not effectively address the method's robustness to large ambient temperature variations. On a separate day of operation, a second experiment was conducted in order to demonstrate the accuracy of the flow angle and magnitude measurements when exposed to higher ambient temperatures relative to the calibration temperature range. The calibration was conducted at the beginning of the day with sweeps characterized by probe angles $\theta = [14.9°, -14.9°, -0.1°, -0.1°]$, temperature within the range $T = [22.8°\text{C}, 29.6°\text{C}]$, and compensation temperature $\widehat{T} = 23.9°\text{C}$.

Figure 5.7 shows the results of a freestream experiment testing the directional calibration accuracy for a set of simulated flow angles and magnitudes described by $-35° \leq \theta \leq 35°$ and $2\,\text{m/s} \leq U_0 \leq 14\,\text{m/s}$, respectively. The temperatures corresponding to each of the measurements ranged from approximately 25.9°C to 27.5°C, approximately in the center of the temperature calibration range. As in the first experiment, the measured U and W components align very well with the expected flow conditions within the flow angle range $|\theta| \leq 20°$. Beyond these bounds, the model form error in the effective velocities of each hotwire result in discrepancies between the measured and expected velocity components. The effective velocity error is shown for each hotwire in Figure 5.8 as a function of both flow angle and magnitude. For $\widetilde{V} \geq 4$ m/s, effective velocity error was less than 2% for hotwire 1 within the flow angle range $\theta \leq 20°$ and for hotwire 2 within

$\theta \geq -20^\circ$. This indicates that very accurate measurements are made in for ambient temperatures in the center of the temperature calibration range.

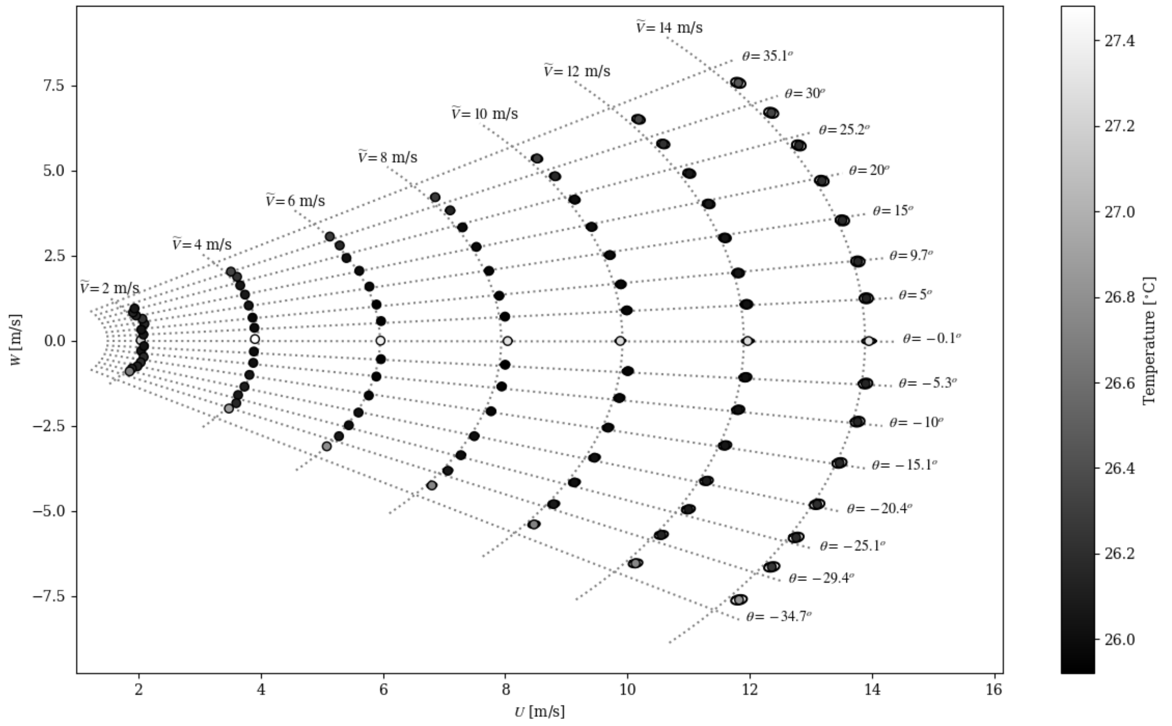

Figure 5.7: Freestream simulation and measurements of various flow angle and velocity magnitude combinations for ambient temperatures centered in the temperature calibration range.

The same day, a secondary set of measurements was collected to test the effects of temperature extending beyond the bounds of the temperature calibration. Figure 5.9 shows the results of a freestream experiment testing the directional calibration accuracy for a set of simulated flow angles and magnitudes described by $-35^\circ \leq \theta \leq 35^\circ$ and $2\,\mathrm{m/s} \leq U_0 \leq 14\,\mathrm{m/s}$, respectively. The temperatures corresponding to each of the measurements ranged from approximately 32.8°C to 34.0°C, approximately 3°–4° above the temperature calibration range. Under these conditions, the U and W components are accurate for flow angles within the range $|\theta| \leq 15^\circ$. The effective velocity error is shown for each hotwire in Figure 5.10 as a function of both flow angle and magnitude. For $\widetilde{V} \geq 4$ m/s, effective velocity error was typically found to remain less than 2% for

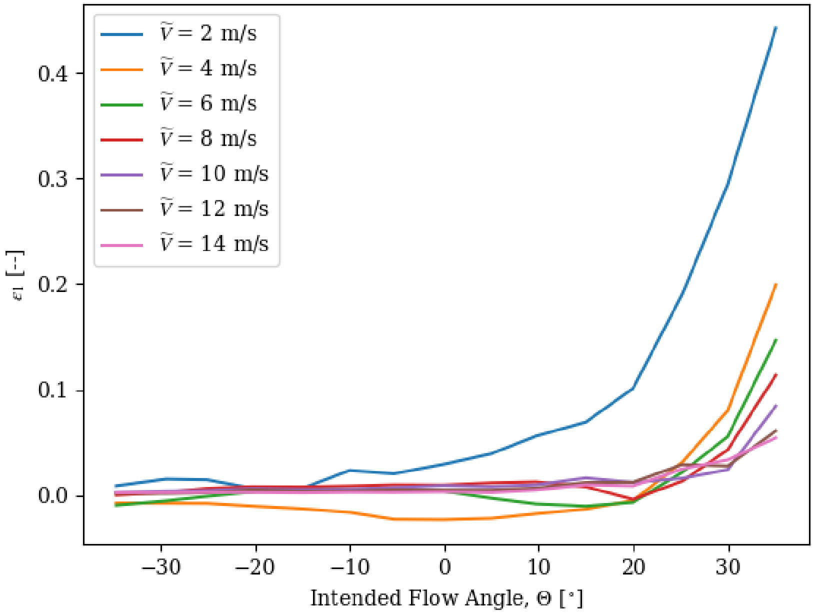

(a) Effective velocity error for wire defined by $\bar{\alpha} = 40°$.

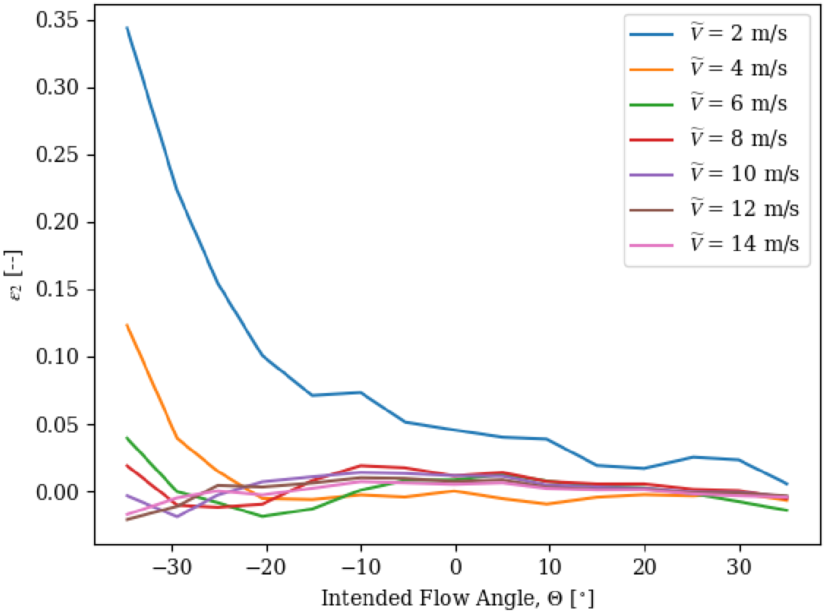

(b) Effective velocity error for wire defined by $\bar{\alpha} = -40°$.

Figure 5.8: Effective velocity error for each hotwire with ambient temperatures midway through the temperature calibration range. Each colored line corresponds to measurements taken at a constant velocity magnitude for a variety of flow angles.

hotwire 1 within the flow angle range $\theta \leq 20°$ and for hotwire 2 within $\theta \geq -20°$. These results are consistent with the results shown for ambient temperatures within the temperature calibration range in Figures 5.7 and 5.8.

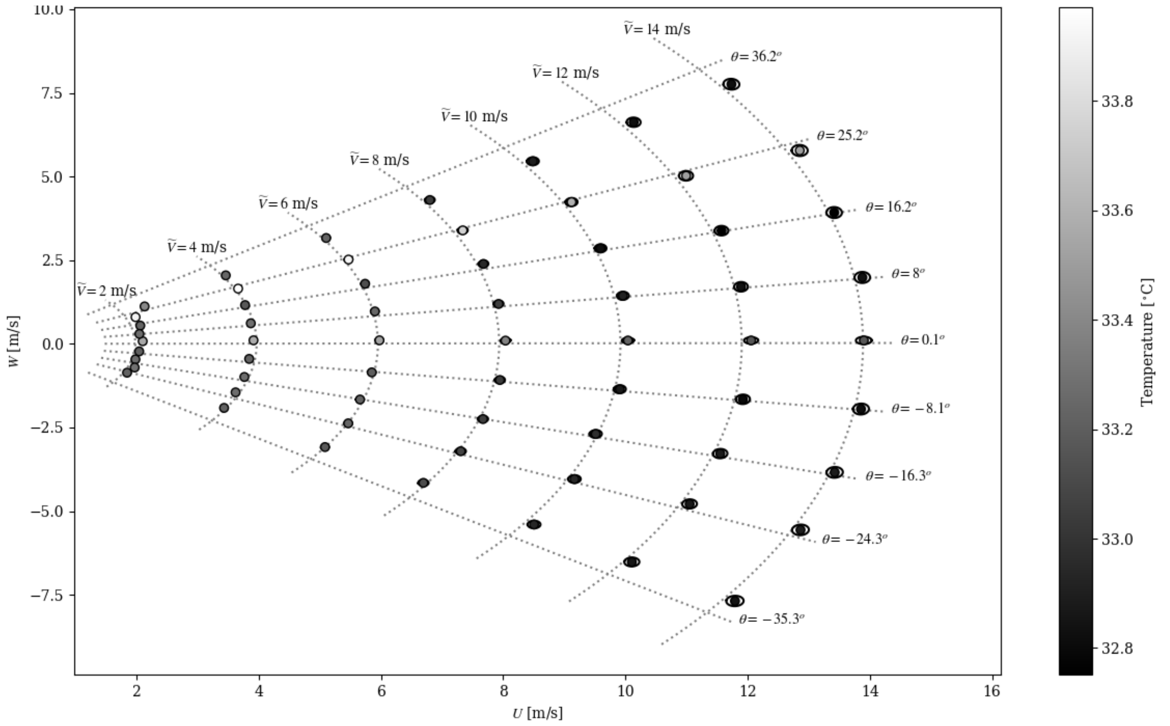

Figure 5.9: Freestream simulation and measurements of various flow angle and velocity magnitude combinations for ambient temperatures extending up to 4°C above the temperature calibration range.

To demonstrate the usefulness of temperature compensation, an alternative calibration analysis can be conducted which does not account for temperature effects on the hotwire voltage. The analysis is reduced merely to a directional calibration and temperature calibration coefficients $\widehat{A}$, $\widehat{B}$, and $\widehat{n}$ are removed from consideration. Figures 5.11 and 5.12 show the non-temperature compensated results of the measurements formerly taken within the temperature calibration range. Measurements would be expected to perform as well as previously indicated if the ambient temperature were to remain constant at the mean temperature recorded during the directional calibration, 23.0°C. However, all of the measurements are collected at ambient temperatures at least 3°C higher

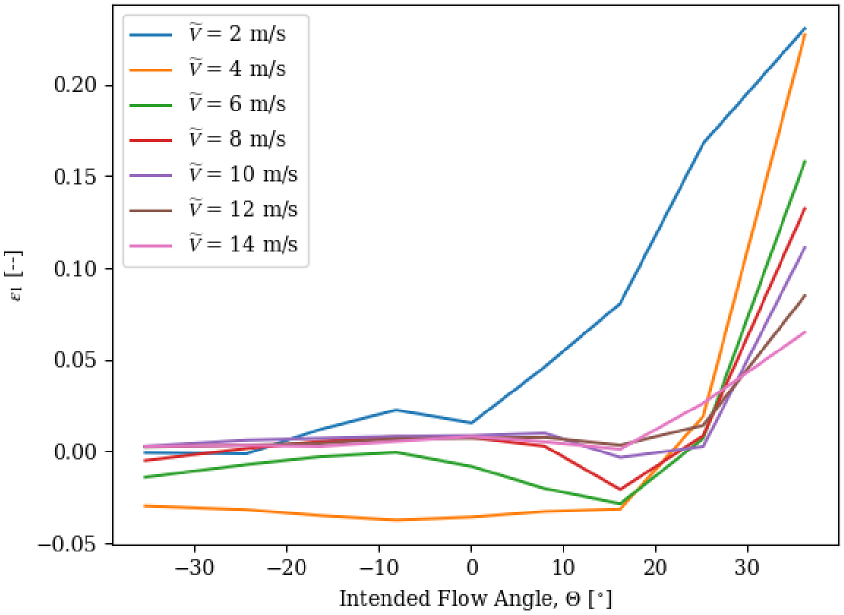

(a) Effective velocity error for wire defined by $\bar{\alpha} = 40°$.

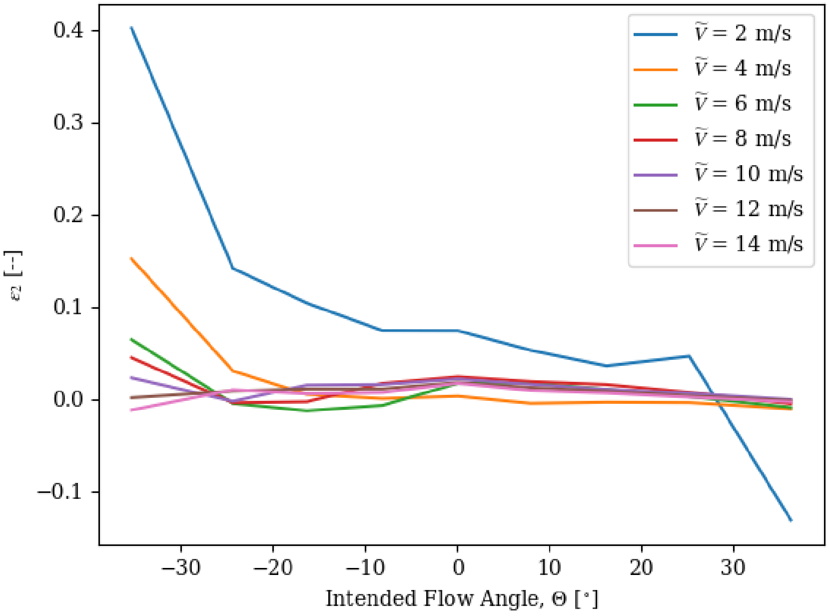

(b) Effective velocity error for wire defined by $\bar{\alpha} = -40°$.

Figure 5.10: Effective velocity error for each hotwire with ambient temperatures extending beyond the temperature calibration range. Each colored line corresponds to measurements taken at a constant velocity magnitude for a variety of flow angles.

than the mean calibration temperature. Without temperature compensation, the elevation of the ambient temperature is perceived by the CTAs as a decrease in flow velocity magnitude because less voltage is required to maintain the high temperature of the hotwire. This trend is evident in the U and W components, whose vector magnitudes are increasingly underestimated with increase in the measurement point ambient temperature. The effective velocity errors in both hotwires reflect this observation, with both remaining negative for most of the measurements and showing especially large negative error at $\theta = 0°$ where the temperature is highest.

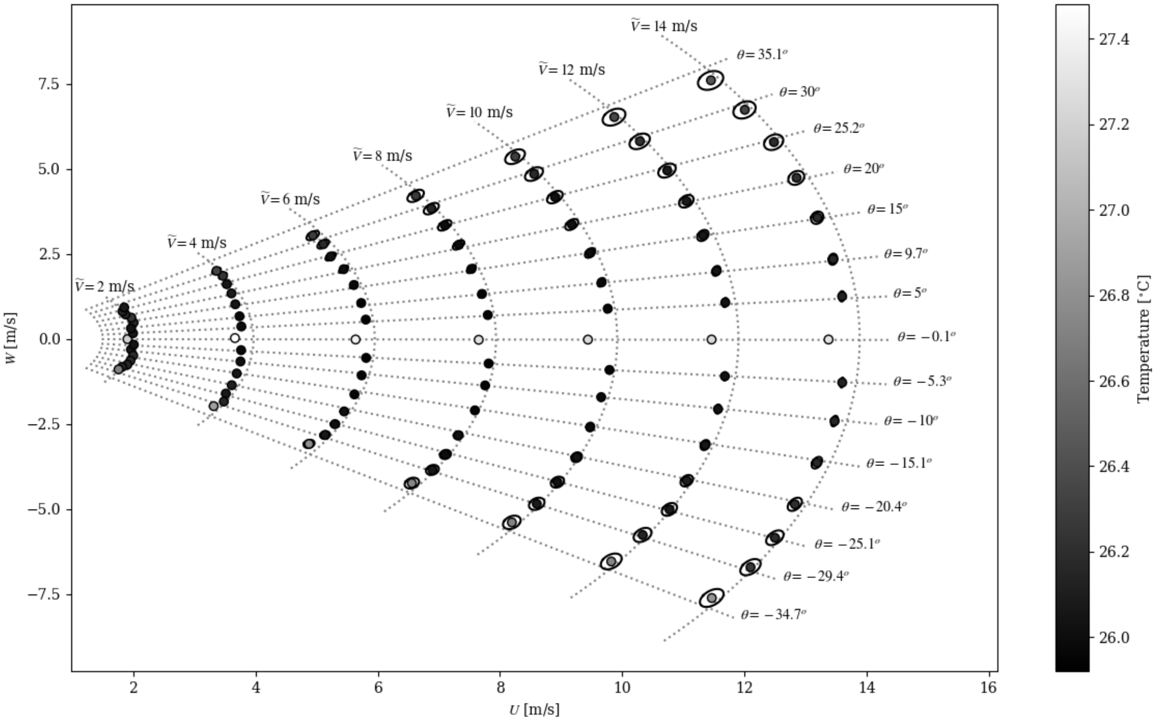

Figure 5.11: Freestream simulation and measurements of various flow angle and velocity magnitude combinations for relatively low ambient temperatures without temperature compensation.

The trends described for Figure 5.11 are only amplified with increasing ambient temperature. Figures 5.13 and 5.14 show the non-temperature compensated results of the measurements formerly taken 3°–4° above the temperature calibration range. The error in the velocity magnitude caused by large ambient temperature drift is quite apparent, but the flow angle measurements

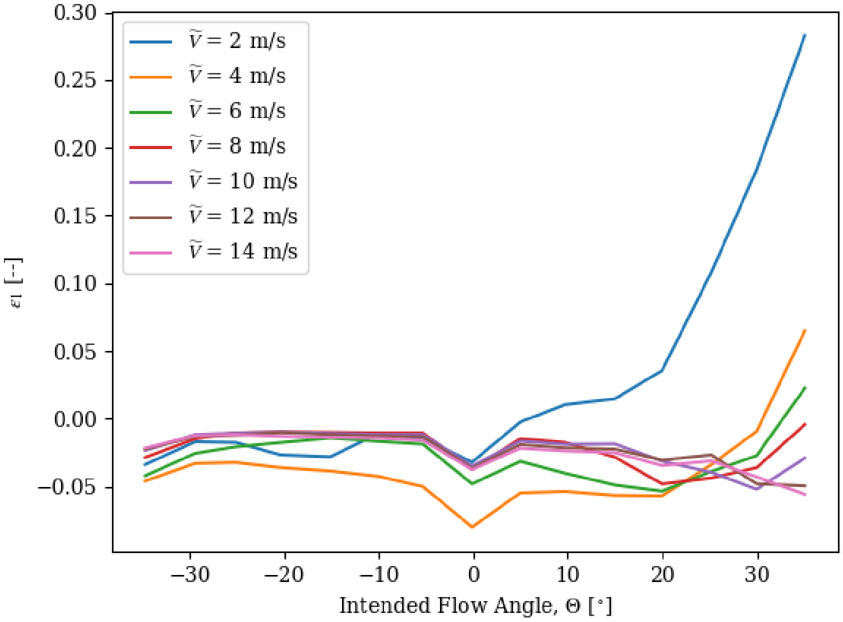

(a) Effective velocity error for wire defined by $\bar{\alpha} = 40°$.

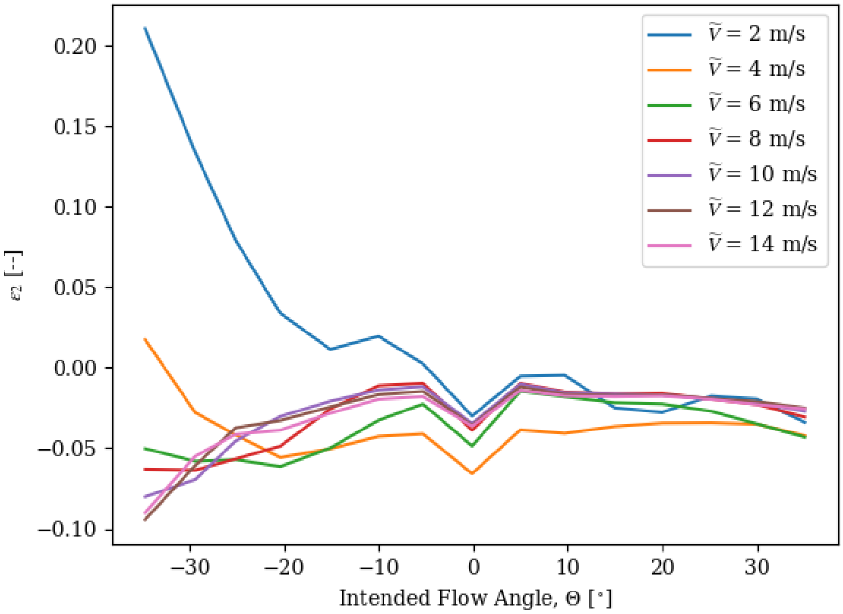

(b) Effective velocity error for wire defined by $\bar{\alpha} = -40°$.

Figure 5.12: Effective velocity error for each hotwire at relatively low ambient temperatures without temperature compensation. Each colored line corresponds to measurements taken at a constant velocity magnitude for a variety of flow angles.

are still in agreement with the intended flow conditions. A comparison of Figures 5.9 and 5.13 shows the importance of temperature compensation for CTA measurements conducted in non-temperature-controlled facilities.

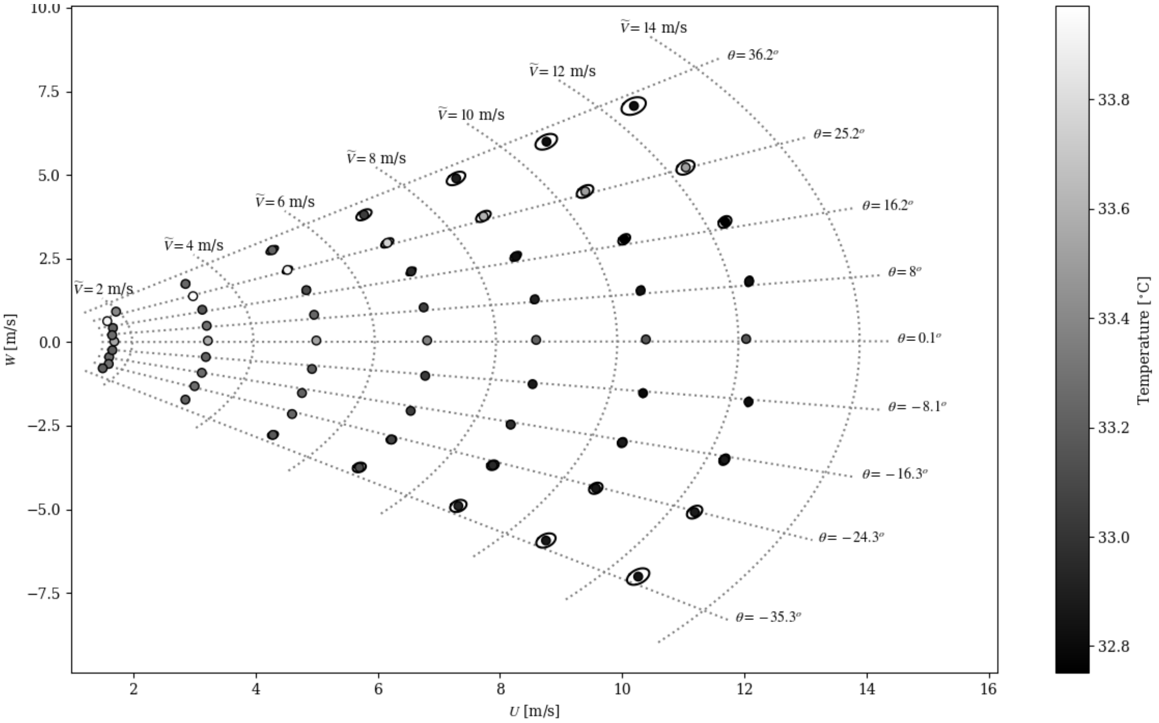

Figure 5.13: Freestream simulation and measurements of various flow angle and velocity magnitude combinations for high ambient temperatures without temperature compensation.

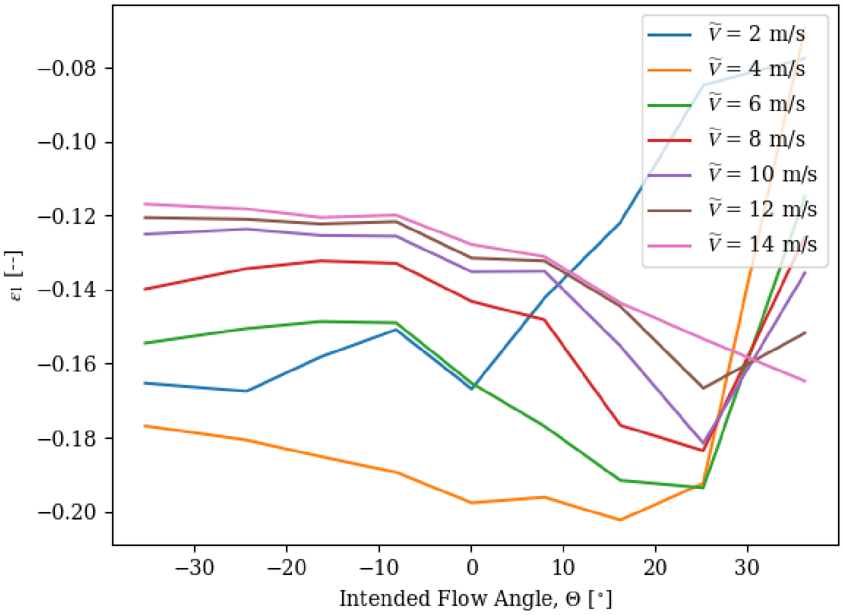

(a) Effective velocity error for wire defined by $\bar{\alpha} = 40°$.

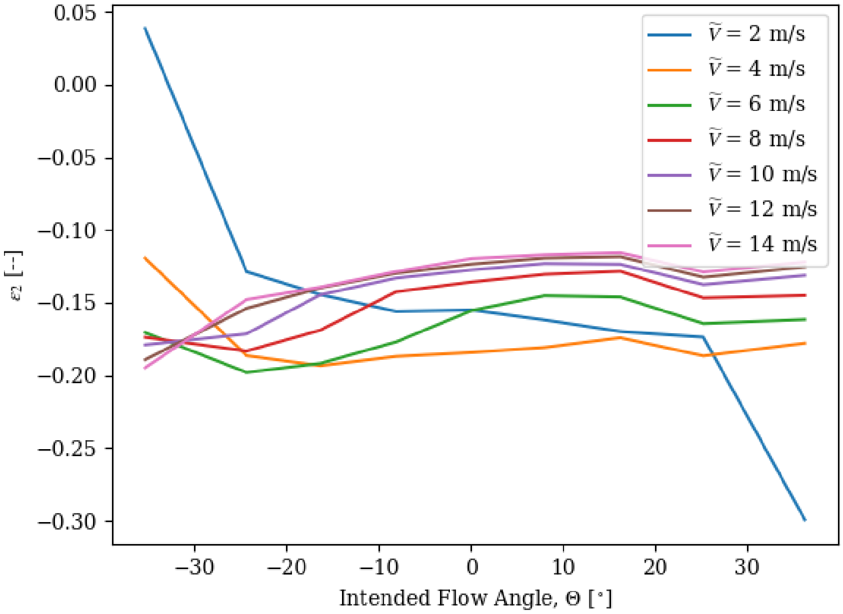

(b) Effective velocity error for wire defined by $\bar{\alpha} = -40°$.

Figure 5.14: Effective velocity error for each hotwire at high ambient temperatures without temperature compensation. Each colored line corresponds to measurements taken at a constant velocity magnitude for a variety of flow angles.

6. VORTEX GENERATOR WAKE MEASUREMENTS

The freestream experiments detailed in Chapter 5 compared hotwire U and W measurements to known, basic flow conditions controlled by adjusting the probe angle and motor speeds. During typical experiments, hotwires are exposed to potentially complex flows whose velocity fields are not known. Single-normal hotwires are extensively and reliably used to measure the streamwise component, U, of the velocity field with great accuracy. This chapter seeks to further validate the calibration model by comparing trusted single-normal U measurements to those estimated by the cross-style hotwire in a complex flow field. This comparison is conducted for measurements collected within a zero-pressure-gradient boundary layer in the wake of a vortex generator.

To generate the disturbance, a removable 6 mm tall by 24 mm long vortex generator was attached to the surface of the zero-pressure-gradient flat plate with an incidence angle of $2^\circ \pm 0.2^\circ$ to the principle flow direction. Figure 6.1 shows the vortex generator adhered to the plate with a trailing edge location with respect to the traverse coordinate system of $x = 1300$ mm and $z = -11$ mm. All measurements were collected at a fixed freestream unit Reynolds number of 500,000 1/m, approximately 7.5 m/s. Boundary layer y-z plane scans were conducted as described in Section 2.2. Measurements ranged 0.25 mm–18 mm from the plate in the y direction and spanned 20 mm in the z direction centered about the disturbance. Spanwise resolution (z step size) was chosen to be 1 mm for a total of twenty-one boundary layer scans comprising the data plane. These scans were conducted using both single-normal hotwires and cross-style hotwires for a series of five streamwise planes evenly spaced from 40 mm to 200 mm downstream of the vortex generator's trailing edge.

Single-normal hotwire measurements used a Dantec type 55P16 hotwire in the boundary layer position and a Dantec type 55P11 hotwire in the freestream. Both wires were calibrated following the method of White [3] which includes temperature compensation. To avoid wall collision, wall finding scans were conducted in the laminar regions outside of the vortex generator's wake. As described in Section 2.2, the boundary layer hotwire was plunged towards the wall until measuring

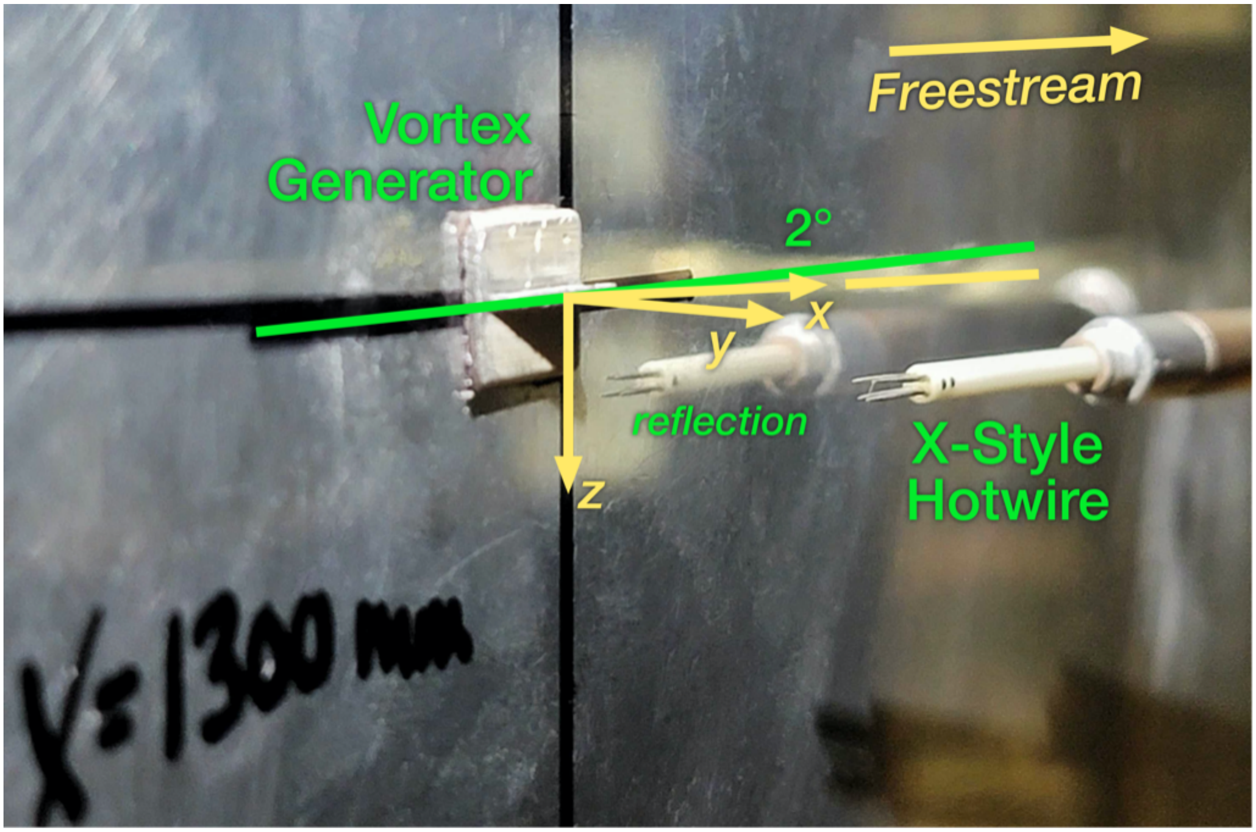

Figure 6.1: Vortex generator adhered to the Brunswick plate with an incidence angle of 2° $\pm$ $0.2°$ and trailing edge location of $x = 1300$ mm and $z = -11$ mm.

a velocity of 12% of that measured by the freestream wire, at which point the velocity profile was linear and used to extrapolate the wall location. After conducting the wall-finding scans, each of the planes of U component data were collected to within 0.25 mm of the estimated wall location.

Cross-style hotwire measurements used a Dantec type 55P61 hotwire in the boundary layer position and a Dantec type 55P11 hotwire in the freestream. The cross-style wire was calibrated using the method described in Chapter 3. In a similar fashion to the single-normal case, wall finding scans were conducted in the laminar regions outside of the vortex generator's wake. The laminar velocity ratio cutoff of 12% in this case, however, was determined using only the near-wall hotwire's effective velocity. The wall location was estimated as a function of the spanwise coordinate, z, enabling the collection of V_e data from the freestream down to the point at which the near-wall hotwire was approximately 0.25 mm from the estimated wall location. The geometry of the cross-style hotwire complicates the calculation of U and W component data because, while the near-wall hotwire records V_{e1} to within 0.25 mm of the wall, the far-wall hotwire can only record V_{e2} to within 1.25 mm of the wall. The U and W components can only be calculated when both V_{e1} and V_{e2} are known at a particular location. This issue is addressed in post-processing by interpolating both wires' effective velocities onto a fixed grid of y locations ranging from 1.25 mm to approximately 17 mm off of the wall. The U and W components are then calculated for each of the interpolated y grid points.

Figure 6.2 shows the comparison between trusted single-normal U/U_∞ measurements and the crosswire U/U_∞ at a single streamwise plane located $\Delta x = 80$ mm downstream of the vortex generator. Qualitatively, the single-normal and crosswire U/U_∞ measurements are in good agreement, capturing similar complex flow features and velocity gradients. Figure 6.3 shows the crosswire W/U_∞ measurements along with the resulting flow angles, $\theta = \tan^{-1}(W/U)$, for the same streamwise plane. With measured flow angles always remaining within the range $-10° \leq \theta \leq 3°$, the freestream experiment results from Chapter 5 indicate that the crosswire U and W measurements are not affected by calibration model form error. Ambient temperature during the measurements also stayed within the temperature range of the calibration, where the results from Chapter 5 indicate that the U and W components are accurately measured. Figures B.1–B.10 show similar results for streamwise measurement planes at $\Delta x = [40, 80, 120, 160, 200]$ mm downstream of the vortex generator trailing edge. All of the cases show close agreement in single-normal and cross-style streamwise components, and all transverse component measurements result in flow angles within the range of confidence.

The comparison of single-normal to cross-style hotwire streamwise component measurements serves as the final check in the development of the temperature compensation routine for cross-style hotwires. Streamwise component agreement with the trusted single-normal hotwire confirms the accuracy of the crosswire U component while the measured flow angle range and conclusions drawn from the freestream experiments add to confidence in the accuracy of the crosswire W component measurement. Additionally, these results indicate that the boundary layer scans can reliably be conducted with cross-style hotwires if wall cutoff conditions are based on the near-wall hotwire’s effective velocity.

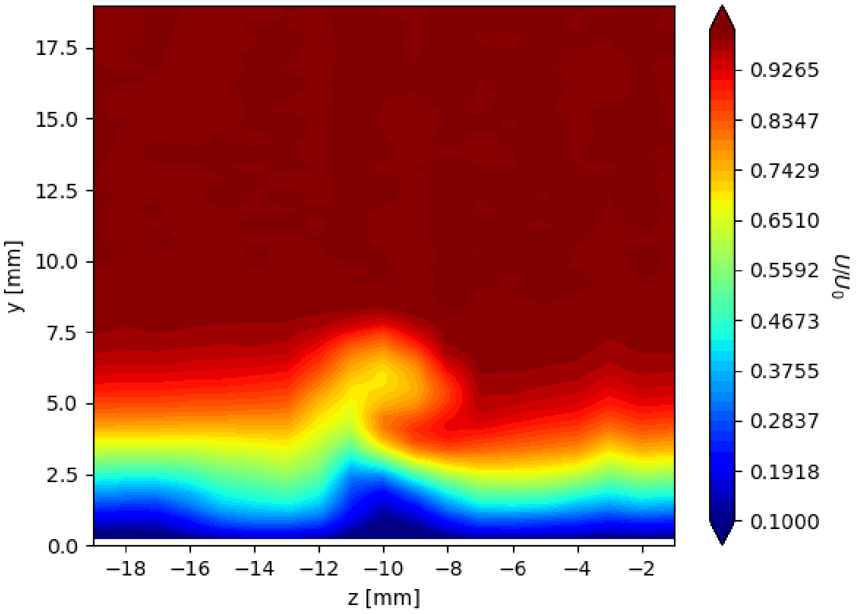

(a) Single-normal U/U_∞ measurement.

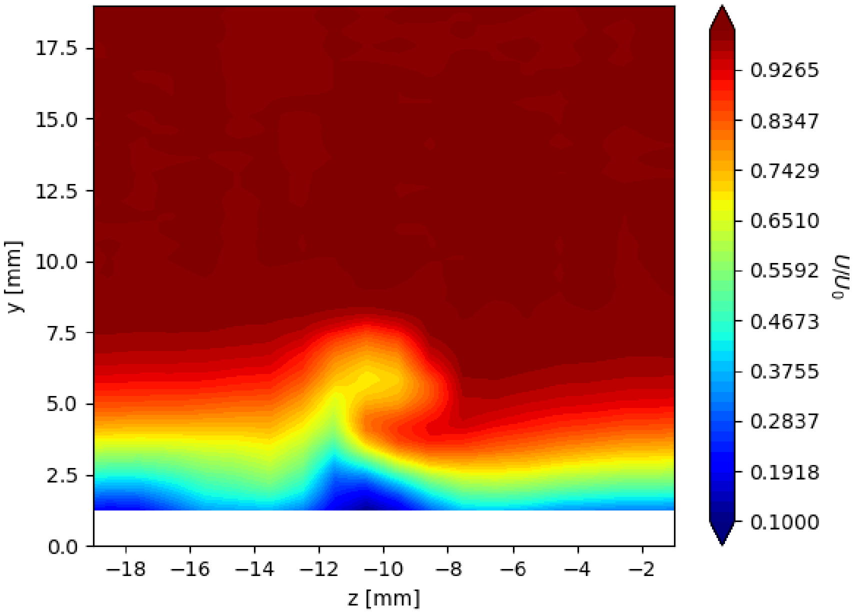

(b) Crosswire U/U_∞ measurement.

Figure 6.2: Single-normal and cross-style hotwire U component measurement comparison at $\Delta x = 80$ mm downstream of the vortex generator trailing edge. White space near the wall corresponds to where the hotwires don't have sufficient information to resolve the velocity components.

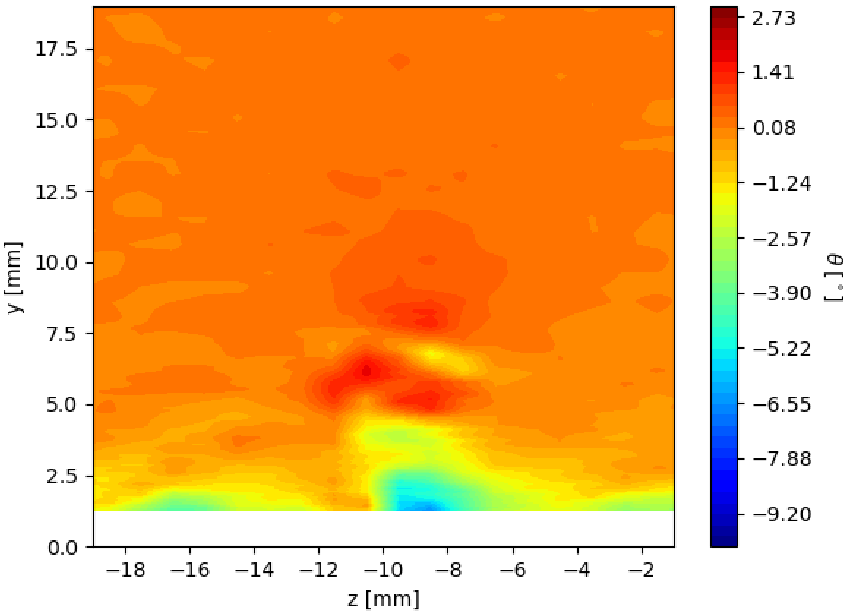

(a) Crosswire flow angle measurement.

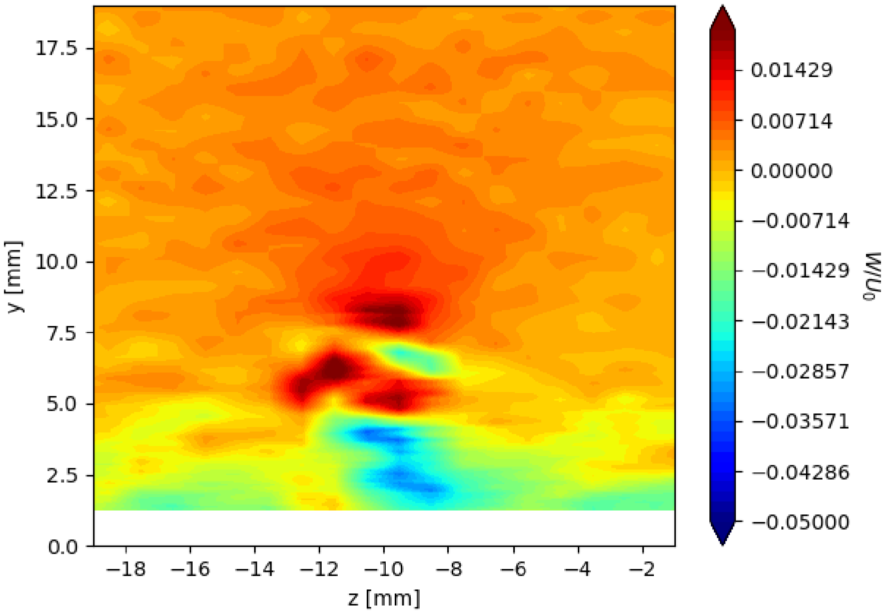

(b) Crosswire W/U_∞ measurement.

Figure 6.3: Cross-style hotwire W component measurement and flow angle, θ, at $\Delta x = 80$ mm downstream of the vortex generator trailing edge. White space near the wall corresponds to where the crosswire doesn't have sufficient information to resolve the velocity components.

7. CONCLUSIONS

Hotwire anemometer calibration techniques in the literature have addressed velocity and temperature variations using single-normal hotwires, velocity and flow angle using cross-style hotwires, and even flow angle and temperature variations at a fixed velocity using cross-style hotwires, but none have addressed velocity, flow angle, and temperature variation together in a rigorous way. The cross-style hotwire calibration technique detailed in this research provides a means of collecting temperature compensated, two-component velocity estimates and their respective correlated uncertainties. Several experiments have been conducted which demonstrate the method's accuracy in measuring streamwise, U, and spanwise, W, components of the flow field.

The calibration consumes approximately 45 minutes per day of operation. With a series of four calibration velocity sweeps, temperature and flow directionality effects on the hotwire voltage measurements are decoupled and addressed in the analyses of each inclined hotwire independently, resulting in a set of seven best-fit calibration parameters for each hotwire. Uncertainties in the calibration parameters were analyzed during development using a Monte Carlo simulation and yielded 3σ uncertainties in the relative velocity magnitude of up to approximately $\pm 1.1\%$ and in the flow angle of up to approximately $\pm 0.65°$.

Several combinations of flow angle, temperature, and velocity magnitude were simulated in the freestream to verify the accuracy of the temperature compensated, two-component velocity measurements. For probe calibration orientations of $\theta = [\pm 15°,\, 0°]$ and wire geometries described by $\bar{\alpha} = \pm 40°$, U and W velocity components within the flow angle range $|\theta| \leq 20°$ were measured with good accuracy. Beyond these bounds, model-form error is observed. Effective velocity measurement error is less than 2% for hotwire 1 ($\bar{\alpha_1} = 40°$) within the flow angle range $\theta \leq 15°$ and for hotwire 2 ($\bar{\alpha_2} = -40°$) within the flow angle range $\theta \geq -15°$. These large ranges of measurement accuracy demonstrate the effectiveness of the directional calibration and particularly the accuracy of the directional sensitivity coefficients, k^2, selected during calibration. Ambient temperature variation had no noticeable effect on the U and W components' accuracies for temperatures within, and even extending $4°$C beyond, the temperature range of the calibration. Effective velocity errors generally remained under 2% for each of the hotwires in their respective flow angle ranges of accuracy, showcasing the effectiveness of the temperature compensation routine.

As a final check of the cross-style hotwire accuracy, boundary-layer normalized streamwise velocity components measured by the cross-wire were compared to those measured by single-normal wires in the wake of a vortex generator. The agreement between the U component measurements gives confidence in both the cross-style U measurements and boundary layer scan technique. Though there was no direct comparison to justify the W component, flow angles measured in each of the boundary-layer scans were in the $\pm 20°$ range, within which the freestream experiments established that both U and W components are accurately measured.

While the technique described in this research provides accurate results for most of the conditions tested, future studies might extend the method to three-dimensions by incorporating the full extent of Jorgensen's effective velocity formulation in Eq. 1.6. Further studies could also investigate methods of increasing model accuracy at very low effective velocities, specifically the case in which $\widetilde{V} \leq 2$ m/s. Being able to more accurately measure the low velocity magnitude range is critical in boundary layer scans, where the velocity magnitude approaches 0 m/s at the wall. Both of these improvements could potentially require the use of additional calibration coefficients and increase the complexity of the problem. The results obtained from the current technique indicate that these additional considerations might decrease the model-form error, however the time required to implement these changes might not be worth the marginal improvement in performance.

REFERENCES

[1] L. V. King, “Xii. on the convection of heat from small cylinders in a stream of fluid: Determination of the convection constants of small platinum wires with applications to hot-wire anemometry,” *Philosophical Transactions of the Royal Society of London. Aeries A, Containing Papers of a Mathematical or Physical Character*, vol. 214, no. 509-522, pp. 373–432, 1914.

[2] H. Bruun, *Hot-wire anemometry principles and signal analysis*. Oxford University Press, 1995.

[3] E. B. White, *Breakdown of crossflow vortices*. 2000.

[4] H. Bruun and C. Tropea, “The calibration of inclined hot-wire probes,” *Journal of Physics E: Scientific Instruments*, vol. 18, no. 5, p. 405, 1985.

[5] P. Stainback and K. Nagabushana, “Review of hot-wire anemometry techniques and the range of their applicability for various flows,” *a a*, vol. 1, p. 4, 1993.

[6] G. Comte-Bellot, “Hot-wire anemometry,” *Annual review of fluid mechanics*, vol. 8, no. 1, pp. 209–231, 1976.

[7] A. Perry, *Hot-wire anemometry*. Oxford University Press, 1982.

[8] F. Jorgensen, “Directional sensitivity of wire and fiber film,” *DISA information*, vol. 11, pp. 31–37, 1971.

[9] J. Hinze, *Turbulence. An introduction to its mechanism and theory.* McGraw-Hill, New York, 1959.

[10] H. H. Al-Kayiem and H. Bruun, “Evaluation of a flying x hot-wire probe system,” *Measurement Science and Technology*, vol. 2, no. 4, p. 374, 1991.

[11] R. Downs, *Environmental influences on crossflow instability*. PhD thesis, 2012.

[12] A. Talamelli, K. Westin, and P. H. Alfredsson, “An experimental investigation of the response of hot-wire x-probes in shear flows,” *Experiments in fluids*, vol. 28, no. 5, pp. 425–435, 2000.

[13] A. V. Johansson and P. H. Alfredsson, “On the structure of turbulent channel flow,” *Journal of Fluid Mechanics*, vol. 122, pp. 295–314, 1982.

[14] G. Morrison, A. Perry, and A. Samuel, “Dynamic calibration of inclined and crossed hot wires,” *J. Fluid Mech*, vol. 52, no. part 3, pp. 465–474, 1972.

[15] P. Mulhearn and J. Finnigan, “A simple device for dynamic testing of x-configuration hot-wire anemometer probes,” *Journal of Physics E: Scientific Instruments*, vol. 11, no. 7, p. 679, 1978.

[16] W. Kuhn and B. Dressler, “Experimental investigations on the dynamic behaviour of hot-wire probes,” *Journal of Physics E: Scientific Instruments*, vol. 18, no. 7, p. 614, 1985.

[17] R. Adrian, R. Johnson, B. Jones, P. Merati, and A.-C. Tung, “Aerodynamic disturbances of hot-wire probes and directional sensitivity,” *Journal of Physics E: Scientific Instruments*, vol. 17, no. 1, p. 62, 1984.

[18] K. Talluru, V. Kulandaivelu, N. Hutchins, and I. Marusic, “A calibration technique to correct sensor drift issues in hot-wire anemometry,” *Measurement Science and Technology*, vol. 25, no. 10, p. 105304, 2014.

[19] M. Hultmark and A. J. Smits, “Temperature corrections for constant temperature and constant current hot-wire anemometers,” *Measurement Science and Technology*, vol. 21, no. 10, p. 105404, 2010.

[20] S. Takagi, “A hot-wire anemometer compensated for ambient temperature variations,” *Journal of Physics E: Scientific Instruments*, vol. 19, no. 9, p. 739, 1986.

[21] J. Cimbala and W. Park, “A direct hot-wire calibration technique to account for ambient temperature drift in incompressible flow,” *Mineralium Deposita*, vol. 29, no. 1, pp. 299–300, 1994.

[22] K. Bremhorst, "Effect of fluid temperature on hot-wire anemometers and an improved method of temperature compensation and linearisation without use of small signal sensitivities," *Journal of Physics E: Scientific Instruments*, vol. 18, no. 1, p. 44, 1985.

[23] C. G. Bowers, D. H. Willits, H. D. Bowen, *et al.*, "Comparison of temperature correction methods for hot wire anemometers," *Transactions of the ASAE*, vol. 31, no. 5, pp. 1552–1555, 1988.

[24] L. Hunt, R. Downs, M. Kuester, E. White, and W. Saric, "Flow quality measurements in the klebanoff-saric wind tunnel," in *27th AIAA Aerodynamic Measurement Technology and Ground Testing Conference*, p. 4538, 2010.

APPENDIX A

CASE STUDY: WIRE ORIENTATION AND CALIBRATION ANGLE

This section contains the results of the case study used to determine the best conditions of the wire angle, $\bar{\alpha}$, and the calibration probe angles, θ. A discussion is provided in Section 5.1.

Case	**1**	**2**	**3**	**4**	**5**	**6**	**7**	**8**	**9**
$\boldsymbol{\theta}$	$[\pm 10°, 0°]$			$[\pm 15°, 0°]$			$[\pm 20°, 0°]$		
$\bar{\alpha}$	**45.0**°	**40.0**°	**34.2**°	**45.0**°	**40.0**°	**36.8**°	**45.0**°	**40.0**°	**35.9**°
$\boldsymbol{A}$	-1.789	-1.830	-1.878	-1.772	-1.848	-1.895	-1.678	-1.817	-1.928
$\boldsymbol{B}$	0.216	0.220	0.225	0.214	0.222	0.226	0.207	0.219	0.228
$\boldsymbol{k^2}$	0.074	-0.009	-0.148	0.077	0.004	-0.057	0.047	-0.022	-0.100
$\boldsymbol{n}$	2.190	2.187	2.182	2.202	2.184	2.174	2.244	2.197	2.163
$\widehat{\boldsymbol{A}}$	0.042	0.042	0.042	0.042	0.042	0.042	0.042	0.042	0.042
$\widehat{\boldsymbol{B}}$	0.008	0.008	0.008	0.008	0.008	0.008	0.008	0.008	0.008
$\widehat{\boldsymbol{n}}$	1.268	1.268	1.268	1.268	1.268	1.268	1.268	1.268	1.268

(a) Wire 1 Calibration Coefficients

Case	**1**	**2**	**3**	**4**	**5**	**6**	**7**	**8**	**9**
$\boldsymbol{\theta}$	$[\pm 10°, 0°]$			$[\pm 15°, 0°]$			$[\pm 20°, 0°]$		
$\bar{\alpha}$	**-45.0**°	**-40.0**°	**-36.6**°	**-45.0**°	**-40.0**°	**-35.9**°	**-45.0**°	**-40.0**°	**-38.1**°
$\boldsymbol{A}$	-1.751	-1.784	-1.807	-1.732	-1.789	-1.834	-1.739	-1.842	-1.878
$\boldsymbol{B}$	0.211	0.215	0.218	0.210	0.215	0.220	0.210	0.219	0.222
$\boldsymbol{k^2}$	0.156	0.086	0.022	0.151	0.087	0.014	0.135	0.080	0.120
$\boldsymbol{n}$	2.223	2.221	2.219	2.233	2.220	2.211	2.231	2.201	2.190
$\widehat{\boldsymbol{A}}$	0.023	0.023	0.023	0.023	0.023	0.023	0.023	0.023	0.023
$\widehat{\boldsymbol{B}}$	0.029	0.028	0.028	0.029	0.028	0.028	0.029	0.028	0.028
$\widehat{\boldsymbol{n}}$	2.461	2.461	2.461	2.461	2.461	2.461	2.461	2.461	2.461

(b) Wire 2 Calibration Coefficients

Table A.1: Calibration parameters returned from various methods of calibration for each hotwire. All cases with $\bar{\alpha} \neq \pm 40°$ nor $\pm 45°$ correspond to those which treat $\bar{\alpha}$ as a calibration coefficient, the result of which is the value listed.

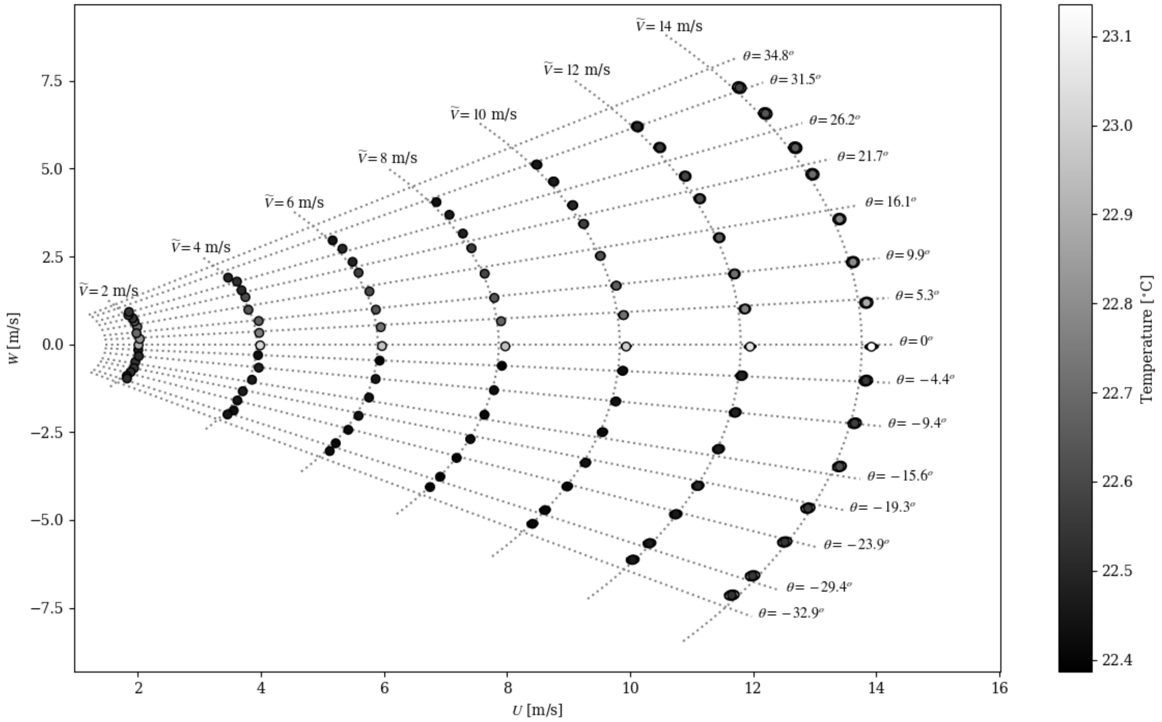

Figure A.1: Case 1: Freestream simulation component results and uncertainties.

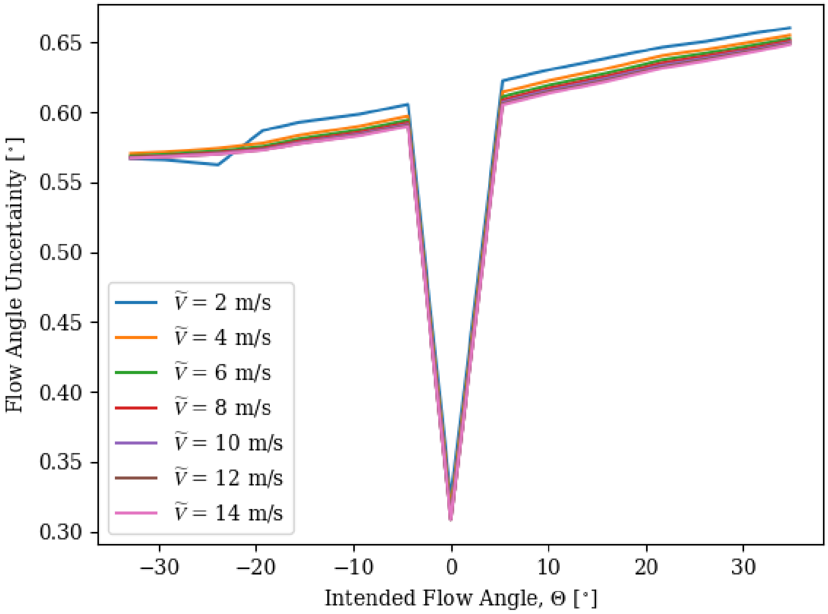

(a) Uncertainty in flow angle, θ.

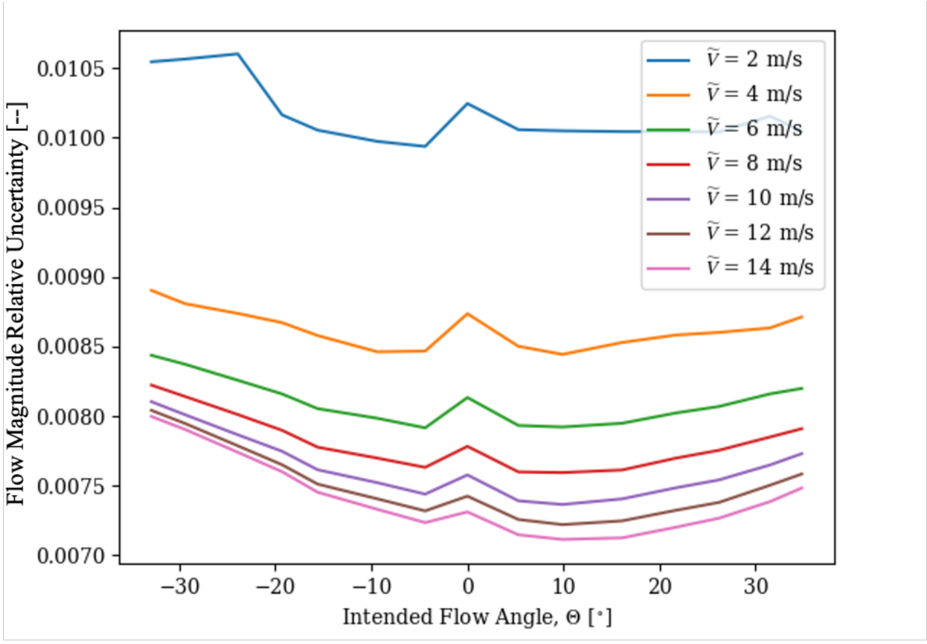

(b) Uncertainty in flow magnitude, $\widetilde{V}$.

Figure A.2: Case 1: Freestream simulation uncertainty in velocity magnitude and flow angle. Each colored line corresponds to measurements taken at a constant velocity magnitude for a variety of flow angles.

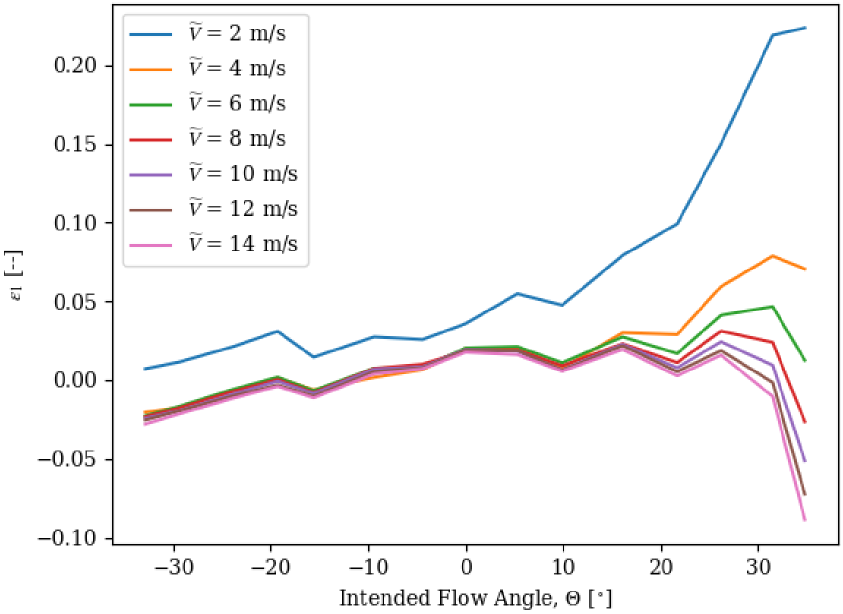

(a) Effective velocity error, $\epsilon_1\left(\widetilde{V},\theta\right)$.

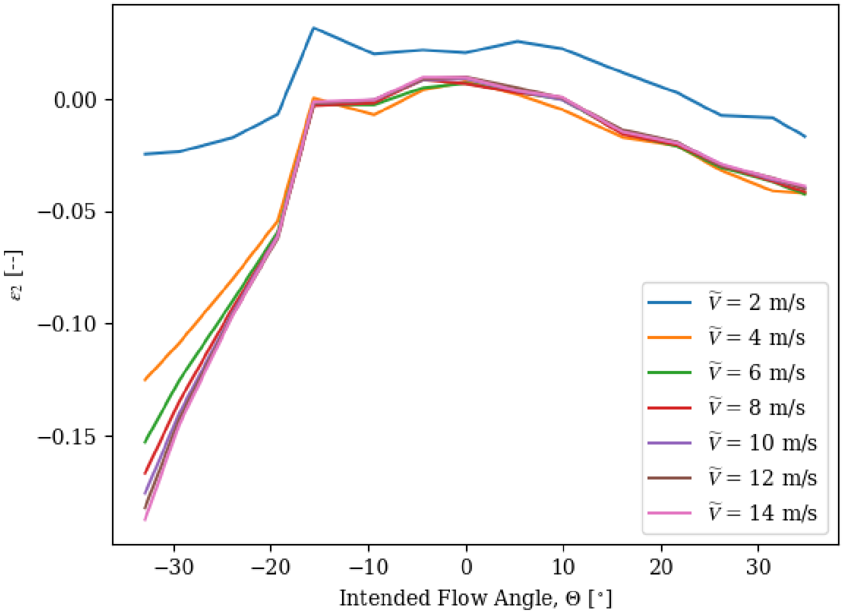

(b) Effective velocity error, $\epsilon_2\left(\widetilde{V},\theta\right)$.

Figure A.3: Case 1: Freestream simulation model-form error in effective velocities. Each colored line corresponds to measurements taken at a constant velocity magnitude for a variety of flow angles.

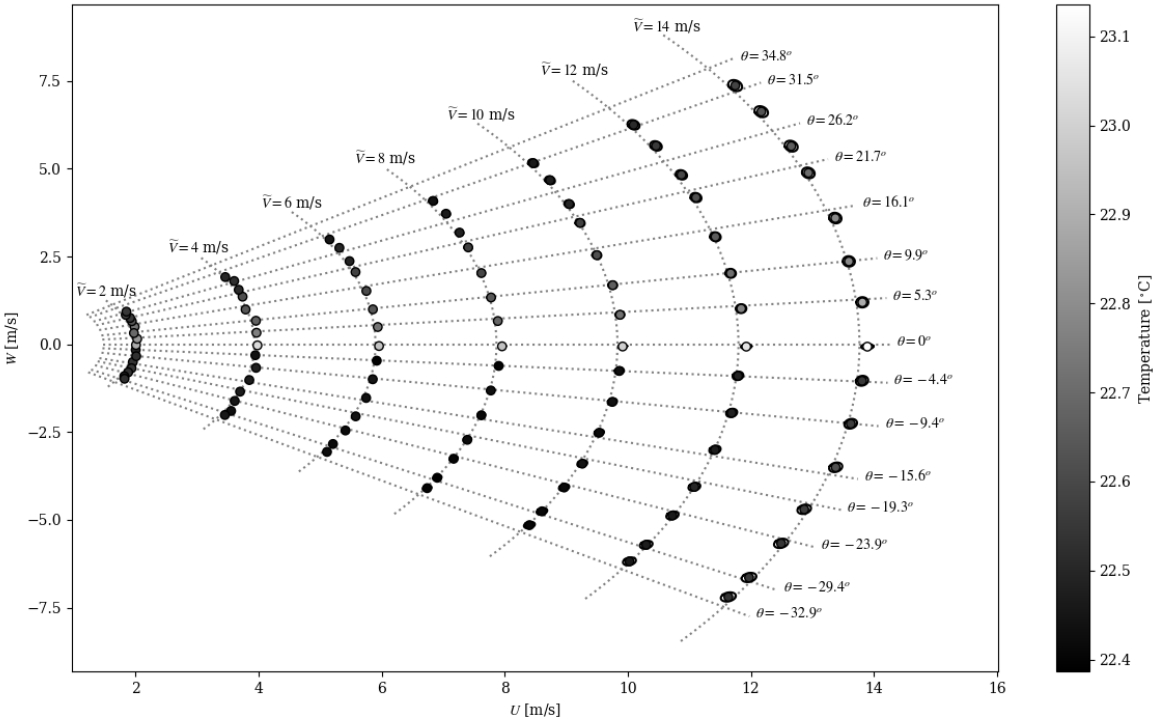

Figure A.4: Case 2: Freestream simulation component results and uncertainties.

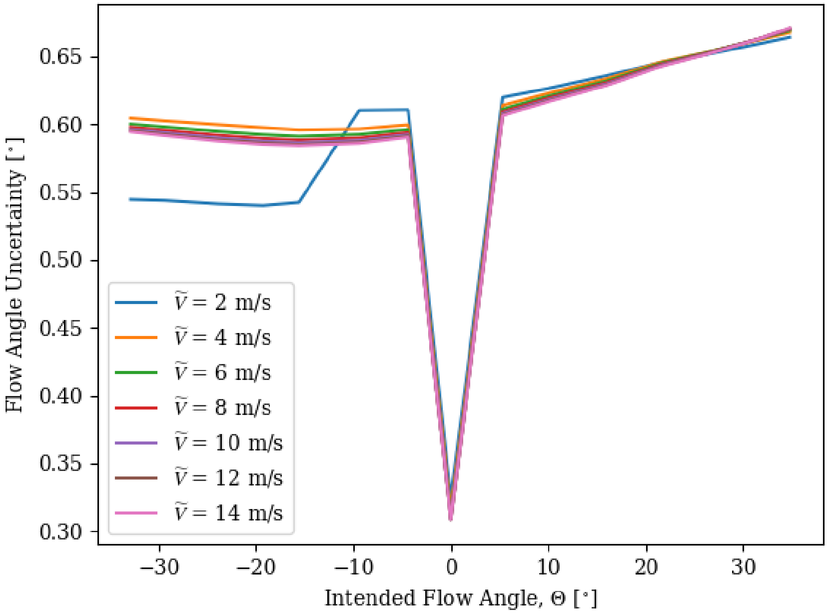

(a) Uncertainty in flow angle, θ.

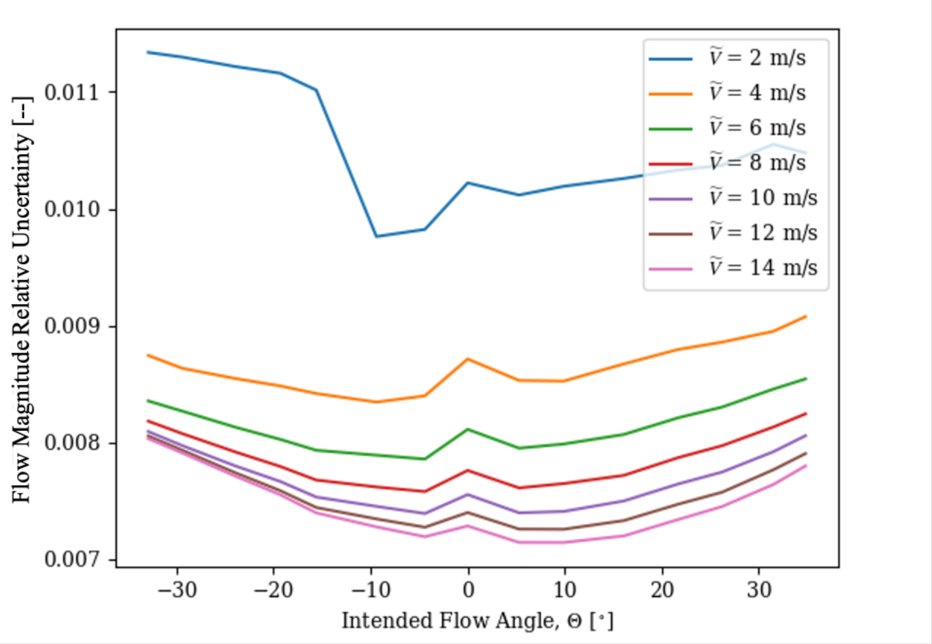

(b) Uncertainty in flow magnitude, $\widetilde{V}$.

Figure A.5: Case 2: Freestream simulation uncertainty in velocity magnitude and flow angle. Each colored line corresponds to measurements taken at a constant velocity magnitude for a variety of flow angles.

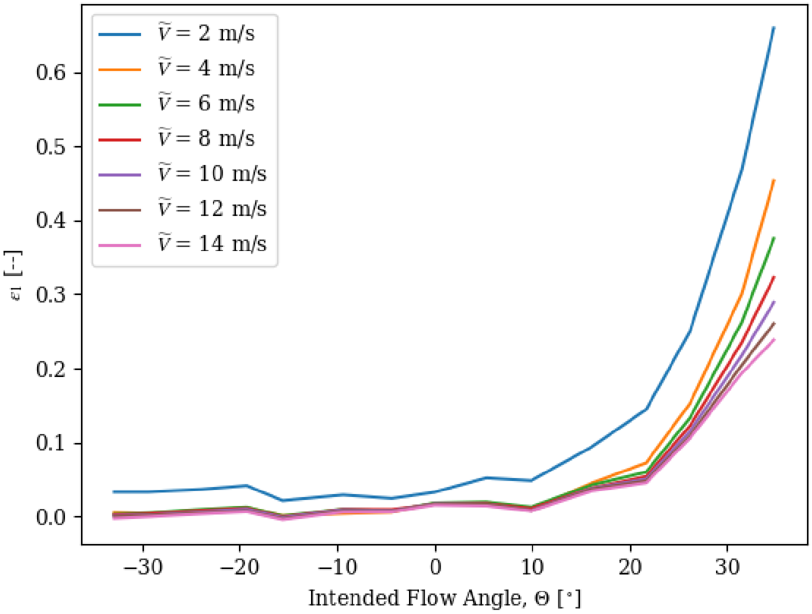

(a) Effective velocity error, $\epsilon_1\left(\widetilde{V}, \theta\right)$.

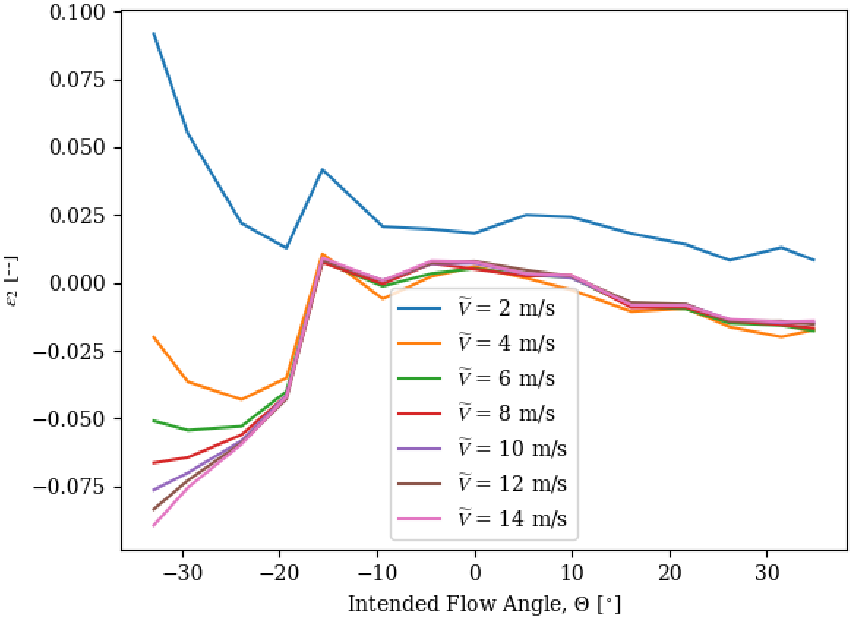

(b) Effective velocity error, $\epsilon_2\left(\widetilde{V}, \theta\right)$.

Figure A.6: Case 2: Freestream simulation model-form error in effective velocities. Each colored line corresponds to measurements taken at a constant velocity magnitude for a variety of flow angles.

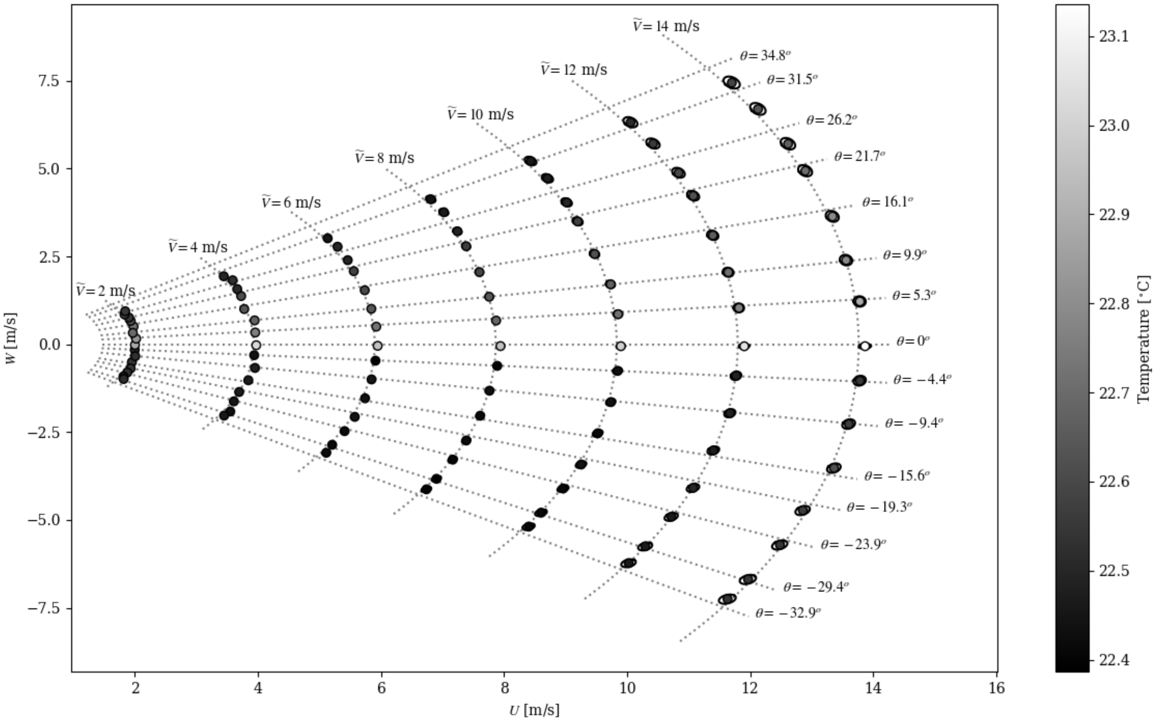

Figure A.7: Case 3: Freestream simulation component results and uncertainties.

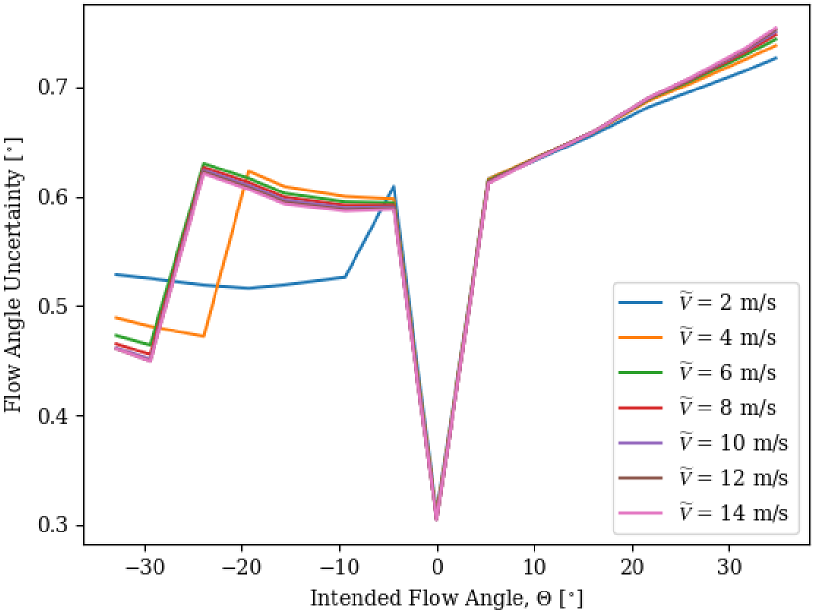

(a) Uncertainty in flow angle, θ.

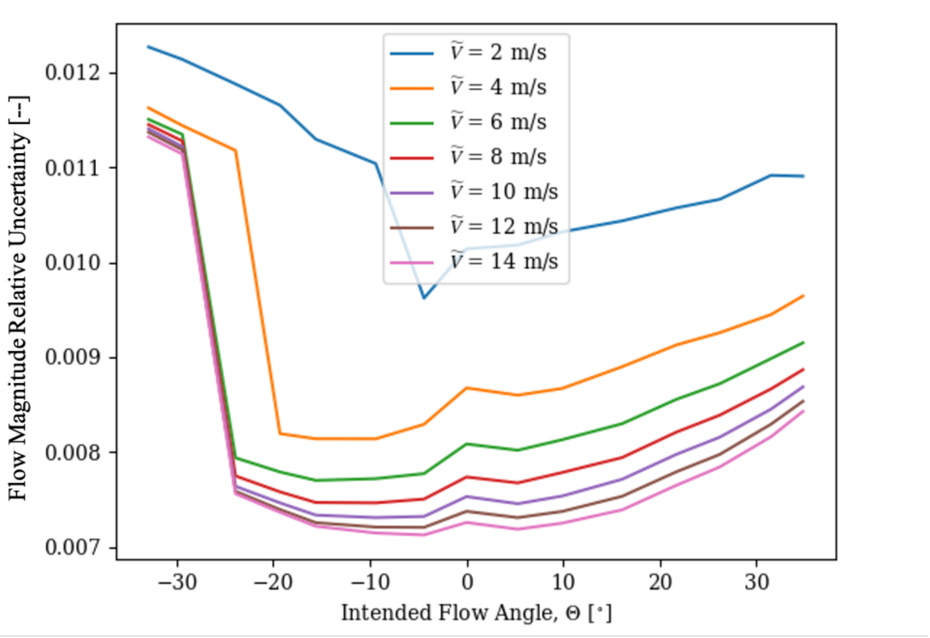

(b) Uncertainty in flow magnitude, $\widetilde{V}$.

Figure A.8: Case 3: Freestream simulation uncertainty in velocity magnitude and flow angle. Each colored line corresponds to measurements taken at a constant velocity magnitude for a variety of flow angles.

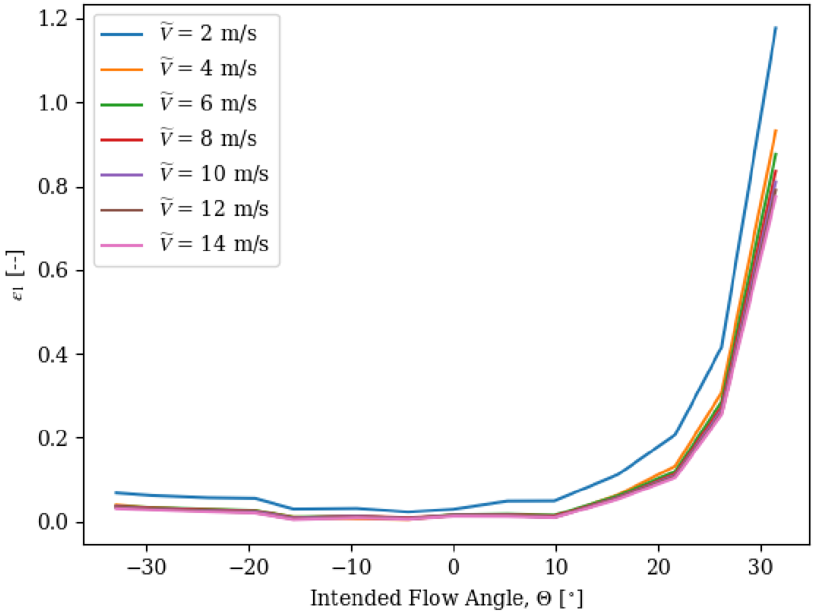

(a) Effective velocity error, $\epsilon_1\left(\widetilde{V}, \theta\right)$.

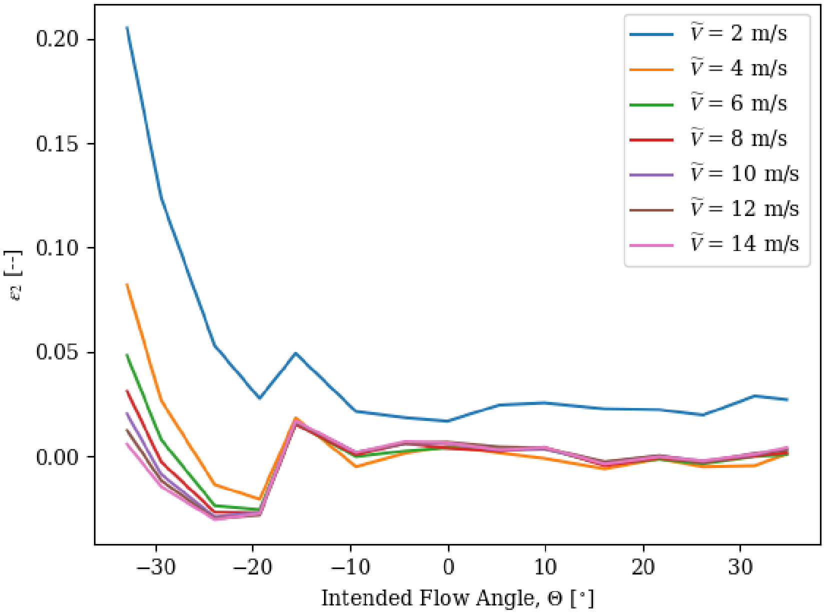

(b) Effective velocity error, $\epsilon_2\left(\widetilde{V}, \theta\right)$.

Figure A.9: Case 3: Freestream simulation model-form error in effective velocities. Each colored line corresponds to measurements taken at a constant velocity magnitude for a variety of flow angles.

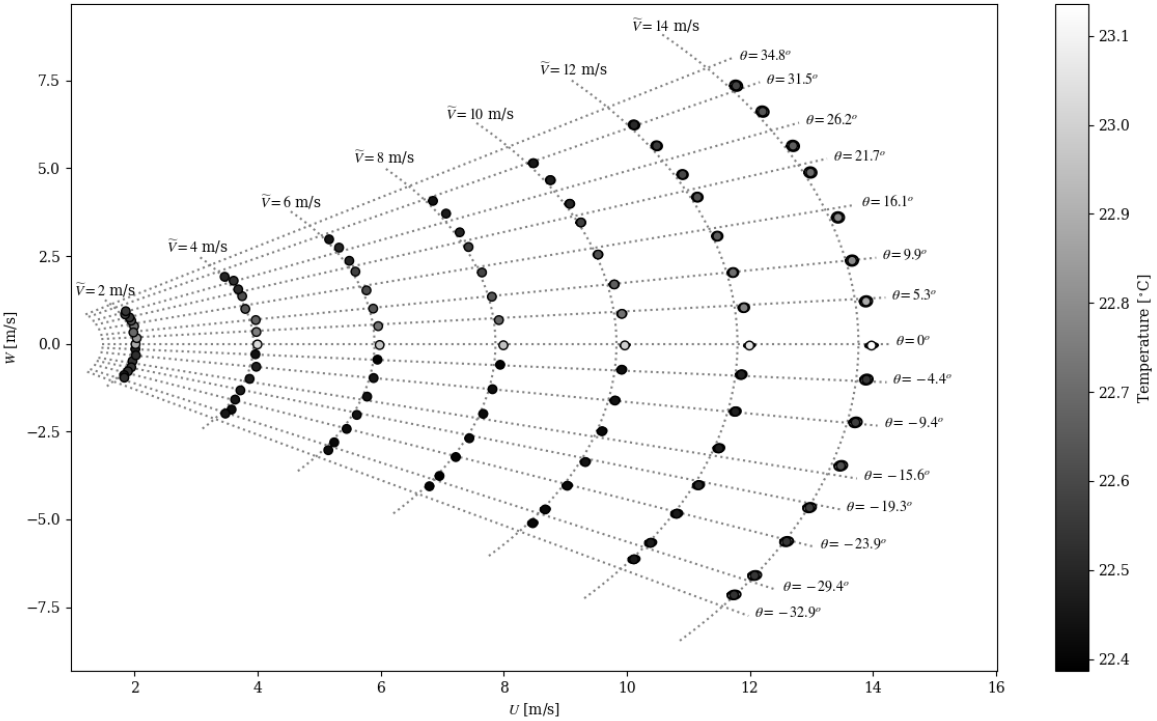

Figure A.10: Case 4: Freestream simulation component results and uncertainties.

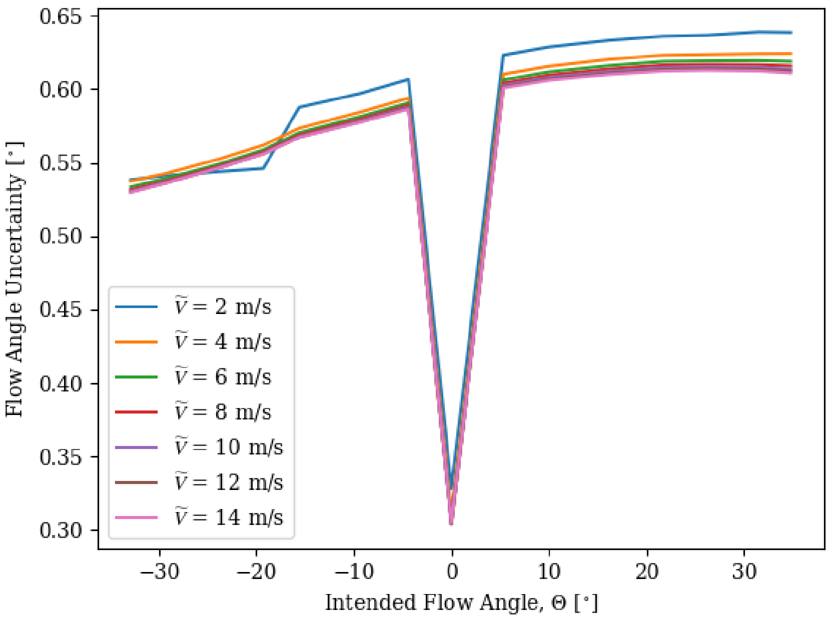

(a) Uncertainty in flow angle, θ.

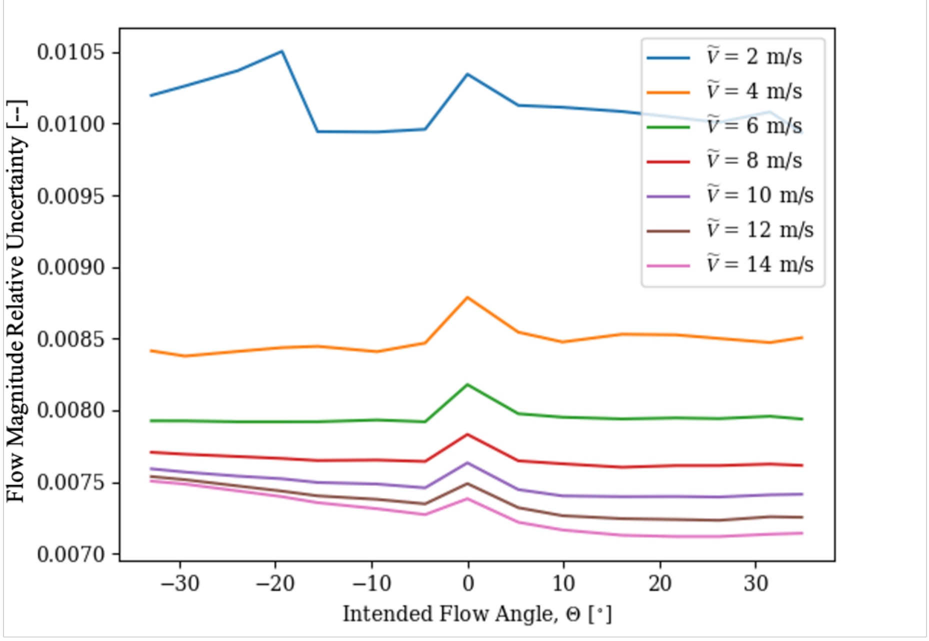

(b) Uncertainty in flow magnitude, $\widetilde{V}$.

Figure A.11: Case 4: Freestream simulation uncertainty in velocity magnitude and flow angle. Each colored line corresponds to measurements taken at a constant velocity magnitude for a variety of flow angles.

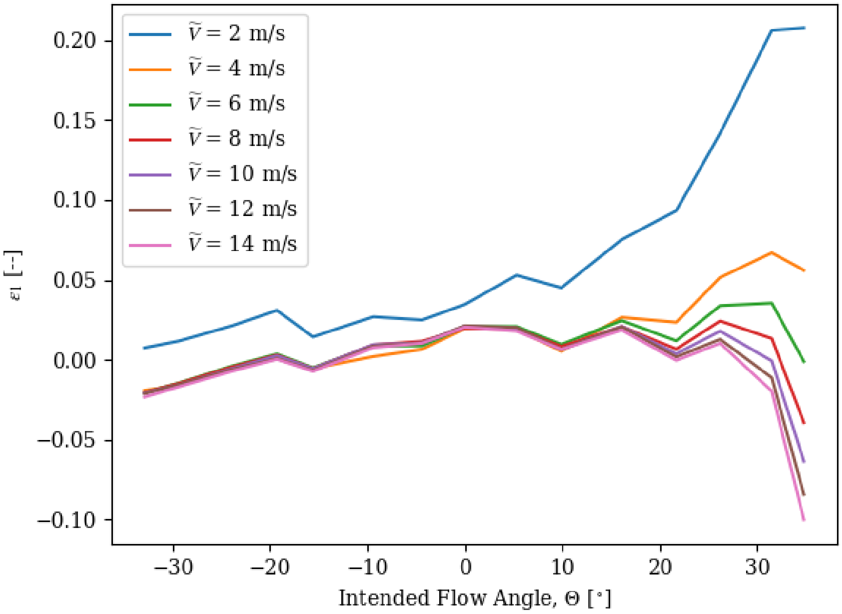

(a) Effective velocity error, $\epsilon_1\left(\widetilde{V},\theta\right)$.

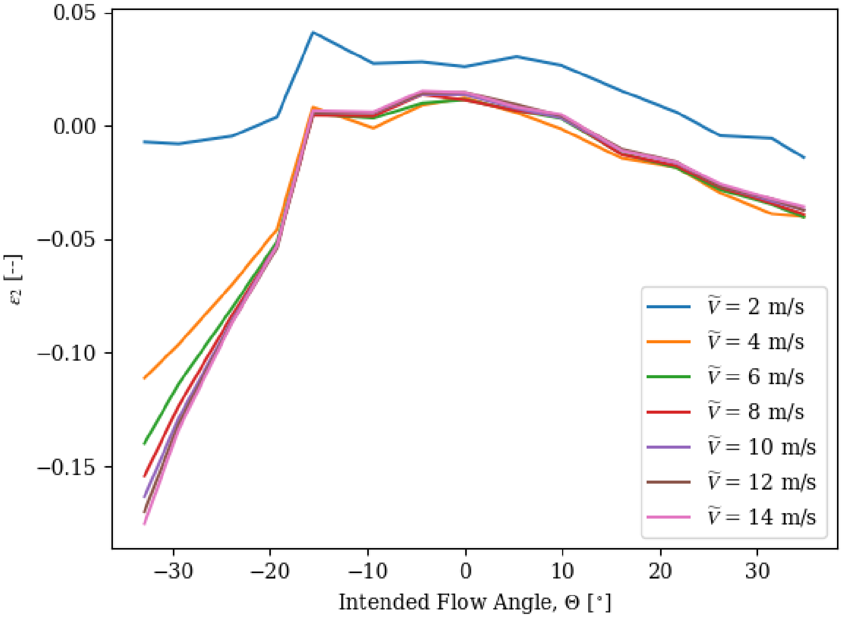

(b) Effective velocity error, $\epsilon_2\left(\widetilde{V},\theta\right)$.

Figure A.12: Case 4: Freestream simulation model-form error in effective velocities. Each colored line corresponds to measurements taken at a constant velocity magnitude for a variety of flow angles.

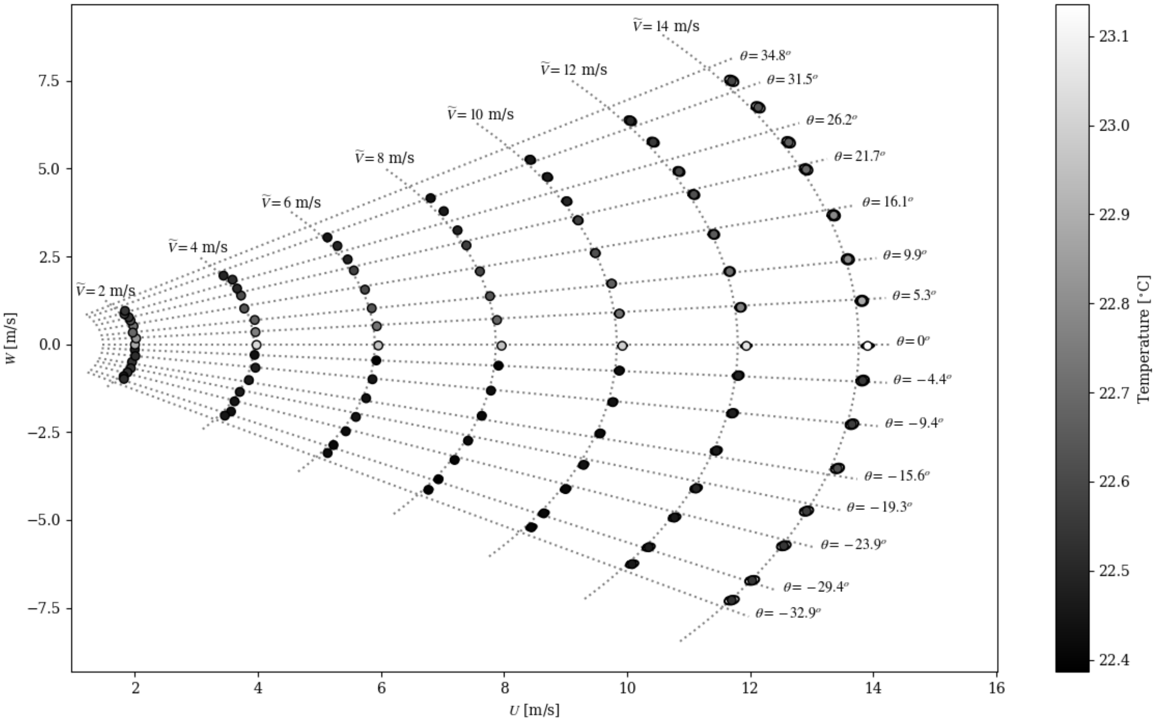

Figure A.13: Case 5: Freestream simulation component results and uncertainties.

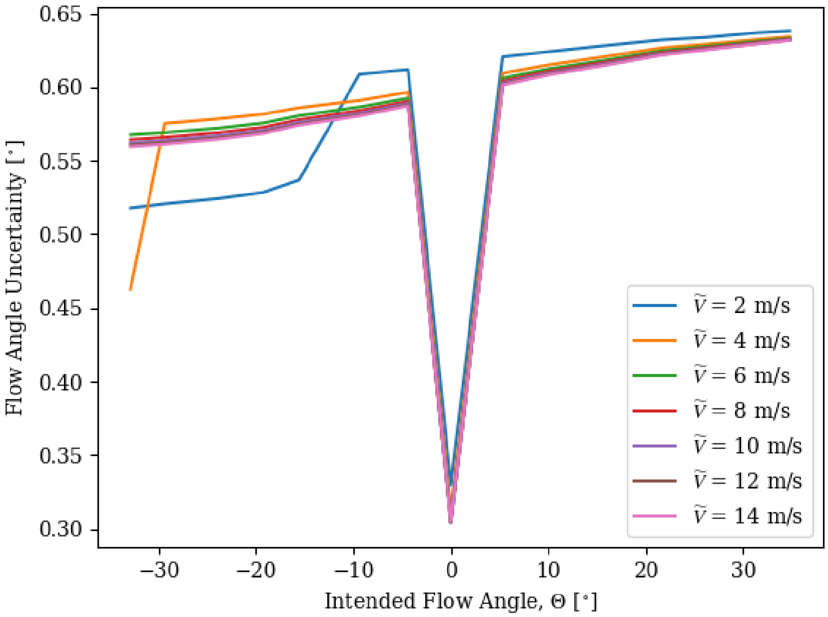

(a) Uncertainty in flow angle, θ.

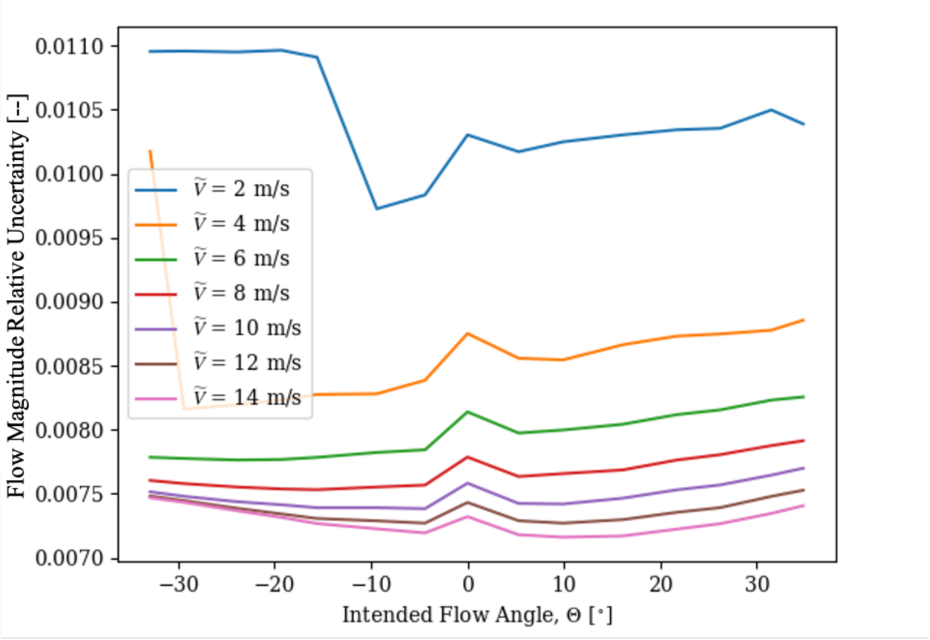

(b) Uncertainty in flow magnitude, $\widetilde{V}$.

Figure A.14: Case 5: Freestream simulation uncertainty in velocity magnitude and flow angle. Each colored line corresponds to measurements taken at a constant velocity magnitude for a variety of flow angles.

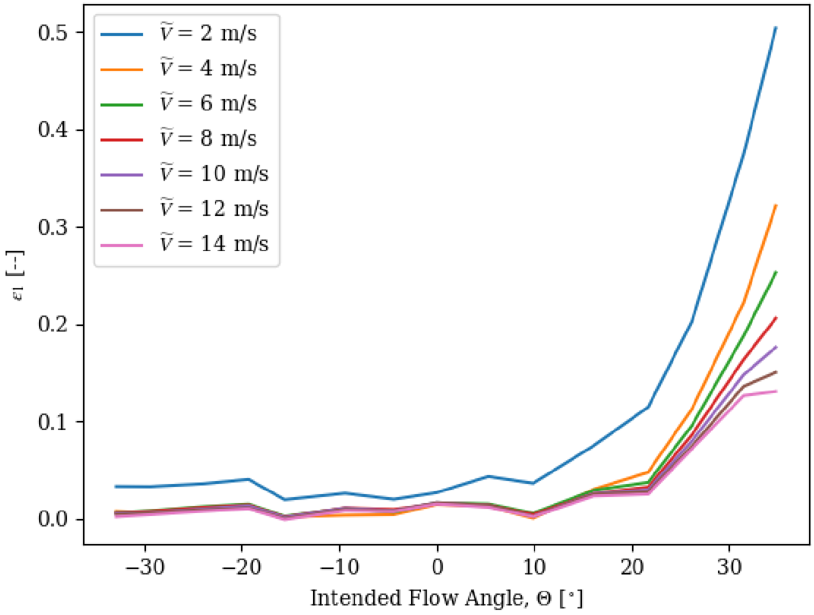

(a) Effective velocity error, $\epsilon_1\left(\widetilde{V},\theta\right)$.

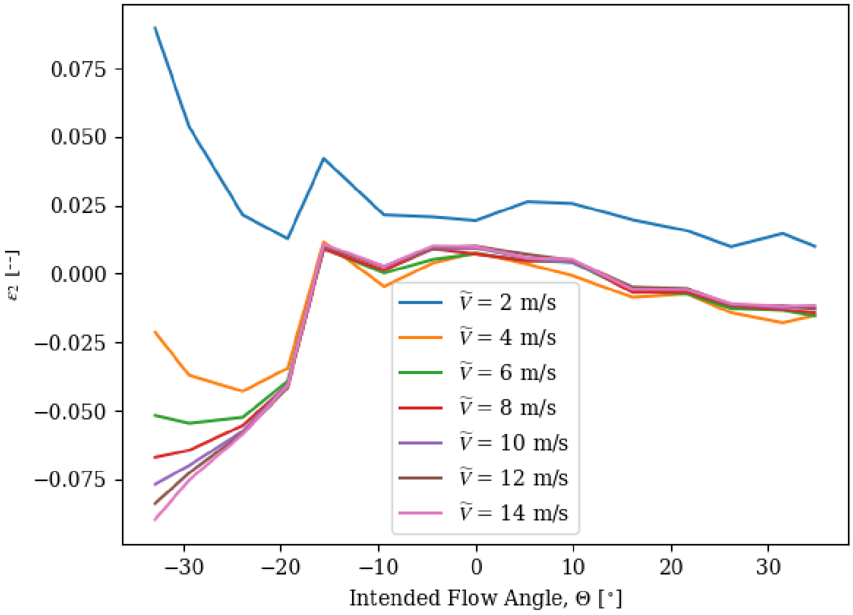

(b) Effective velocity error, $\epsilon_2\left(\widetilde{V},\theta\right)$.

Figure A.15: Case 5: Freestream simulation model-form error in effective velocities. Each colored line corresponds to measurements taken at a constant velocity magnitude for a variety of flow angles.

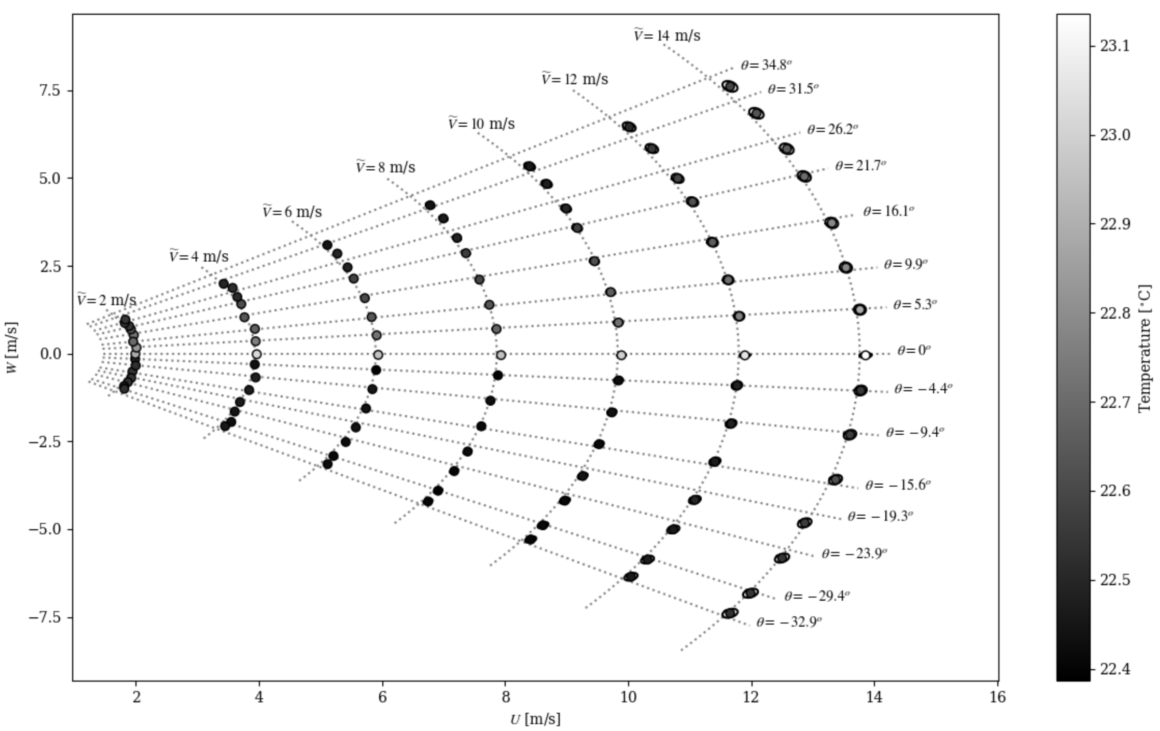

Figure A.16: Case 6: Freestream simulation component results and uncertainties.

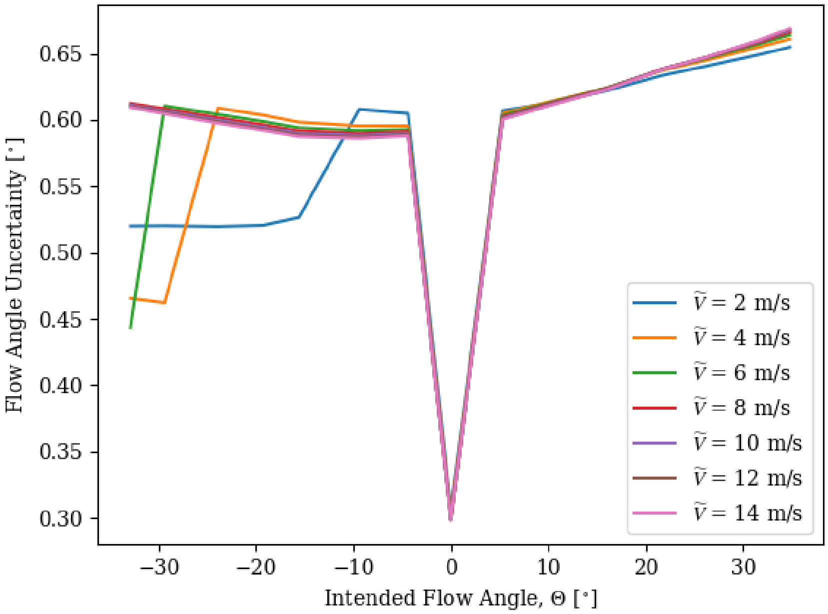

(a) Uncertainty in flow angle, θ.

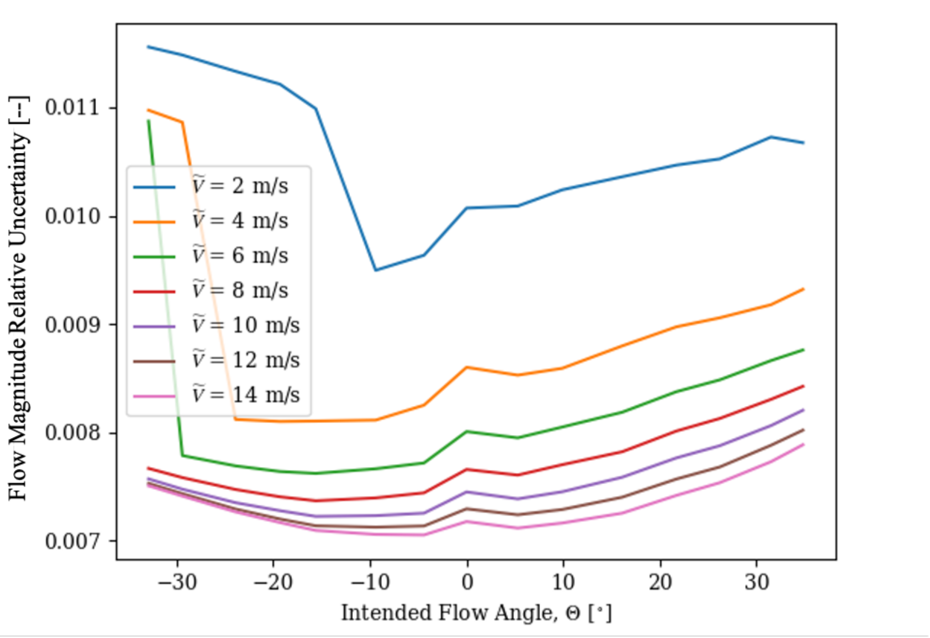

(b) Uncertainty in flow magnitude, $\widetilde{V}$.

Figure A.17: Case 6: Freestream simulation uncertainty in velocity magnitude and flow angle. Each colored line corresponds to measurements taken at a constant velocity magnitude for a variety of flow angles.

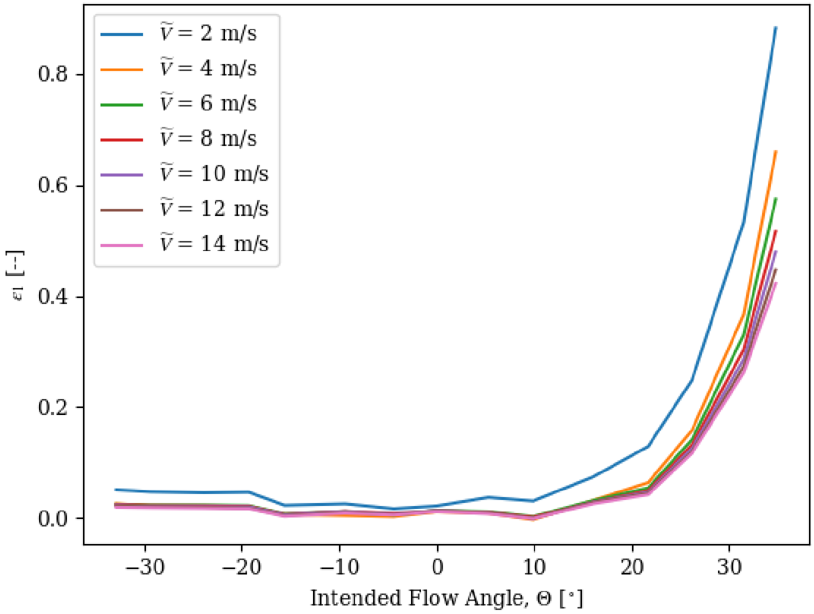

(a) Effective velocity error, $\epsilon_1\left(\widetilde{V}, \theta\right)$.

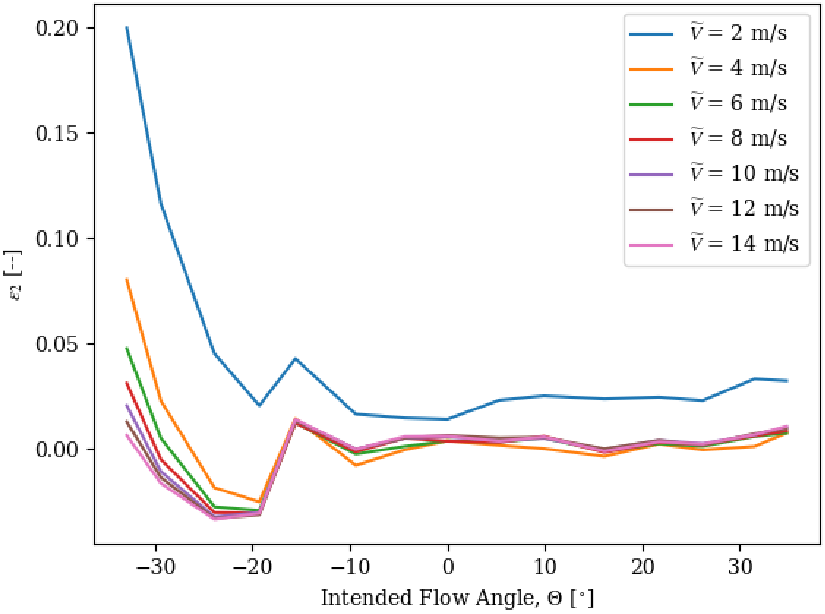

(b) Effective velocity error, $\epsilon_2\left(\widetilde{V}, \theta\right)$.

Figure A.18: Case 6: Freestream simulation model-form error in effective velocities. Each colored line corresponds to measurements taken at a constant velocity magnitude for a variety of flow angles.

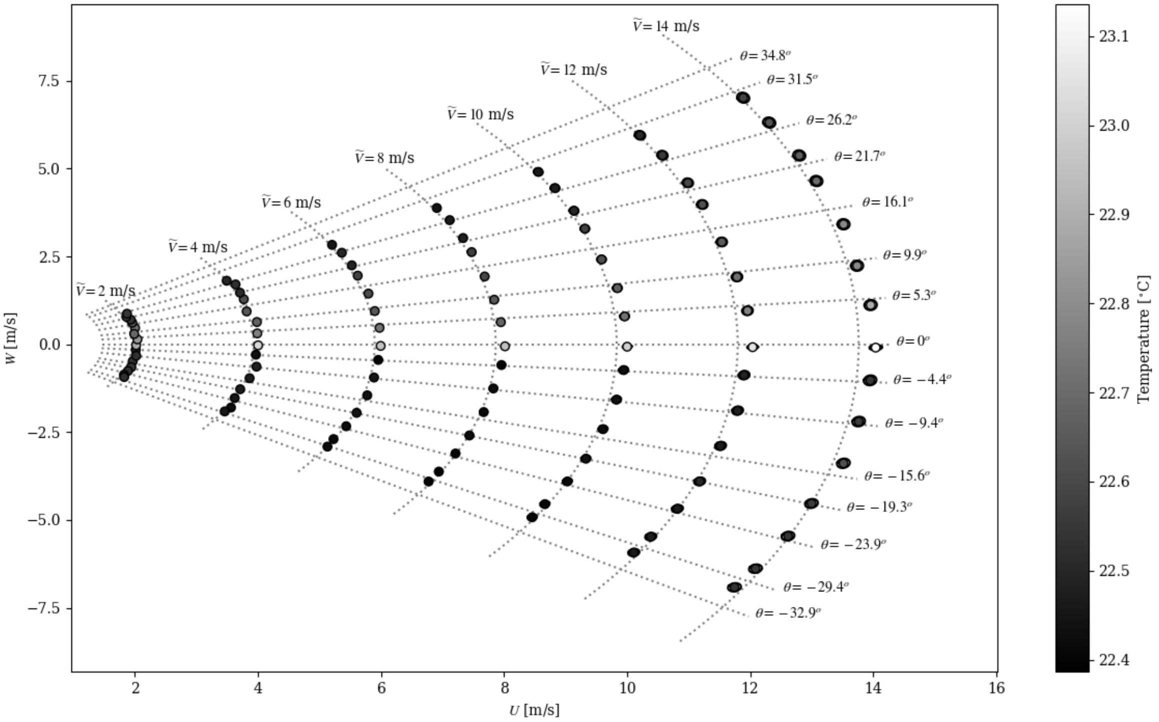

Figure A.19: Case 7: Freestream simulation component results and uncertainties.

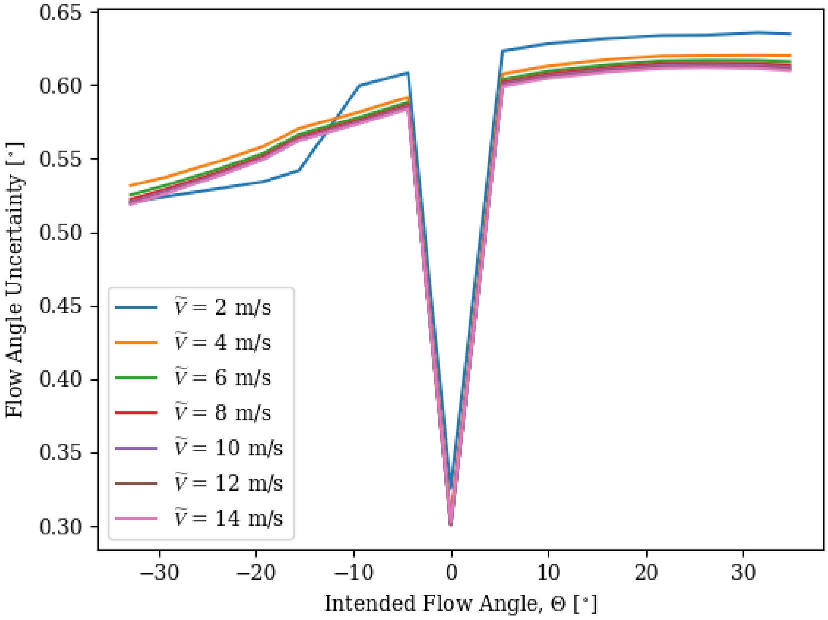

(a) Uncertainty in flow angle, θ.

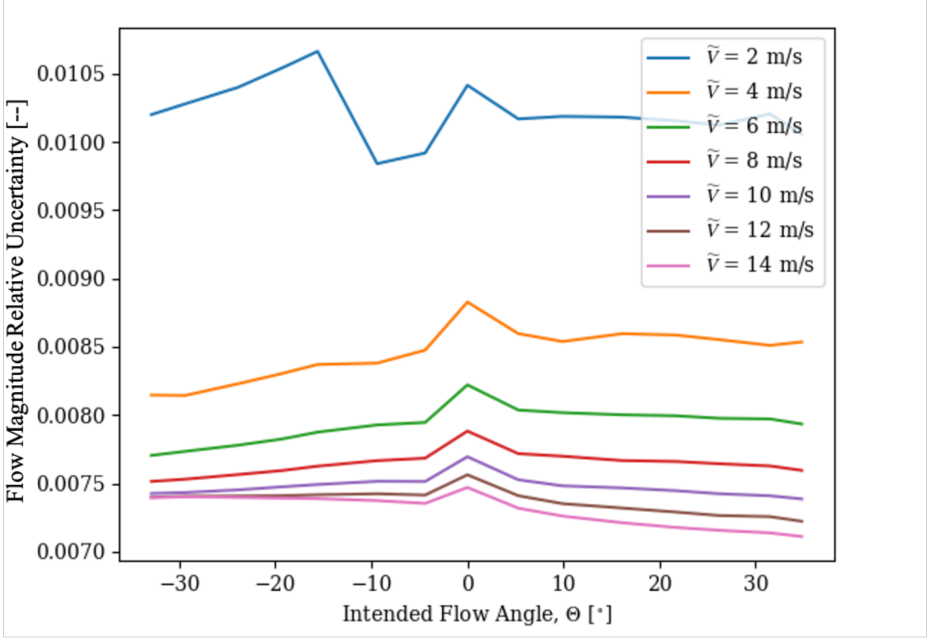

(b) Uncertainty in flow magnitude, $\widetilde{V}$.

Figure A.20: Case 7: Freestream simulation uncertainty in velocity magnitude and flow angle. Each colored line corresponds to measurements taken at a constant velocity magnitude for a variety of flow angles.

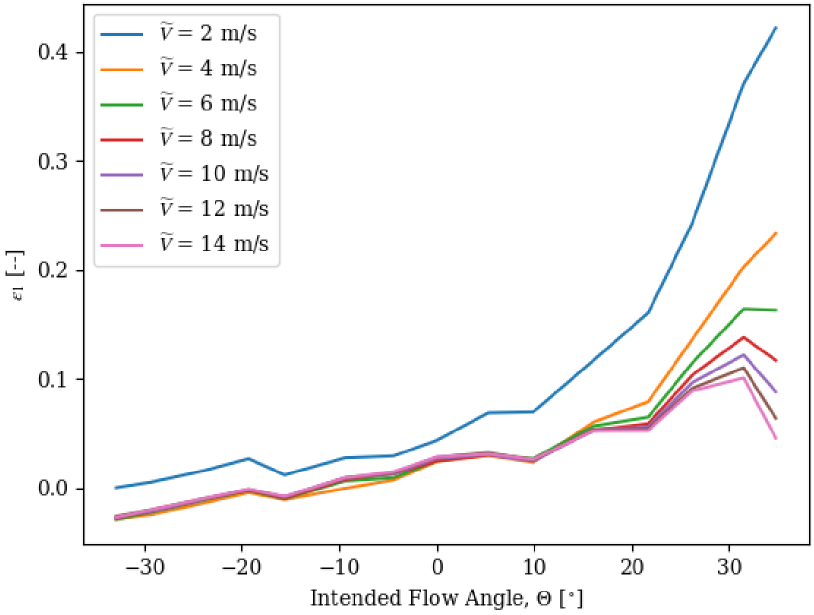

(a) Effective velocity error, $\epsilon_1\left(\widetilde{V},\theta\right)$.

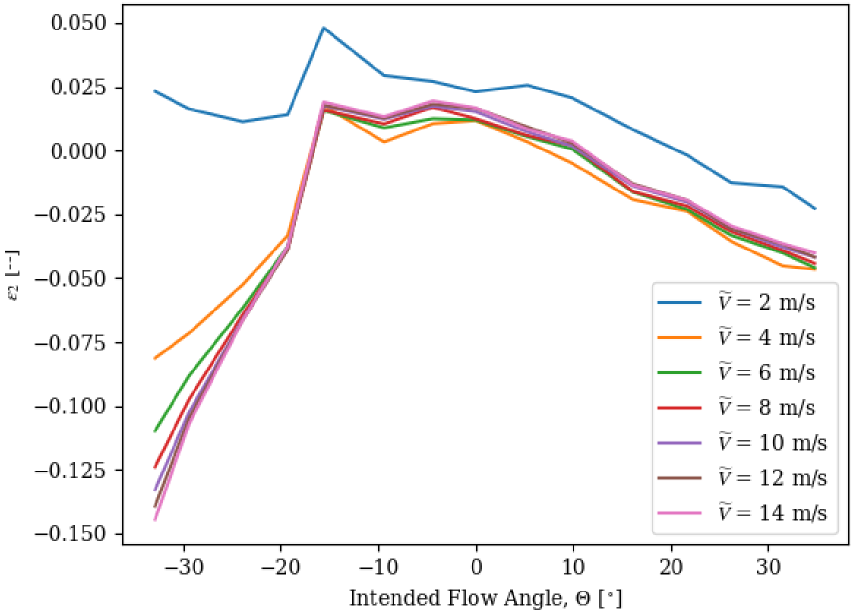

(b) Effective velocity error, $\epsilon_2\left(\widetilde{V},\theta\right)$.

Figure A.21: Case 7: Freestream simulation model-form error in effective velocities. Each colored line corresponds to measurements taken at a constant velocity magnitude for a variety of flow angles.

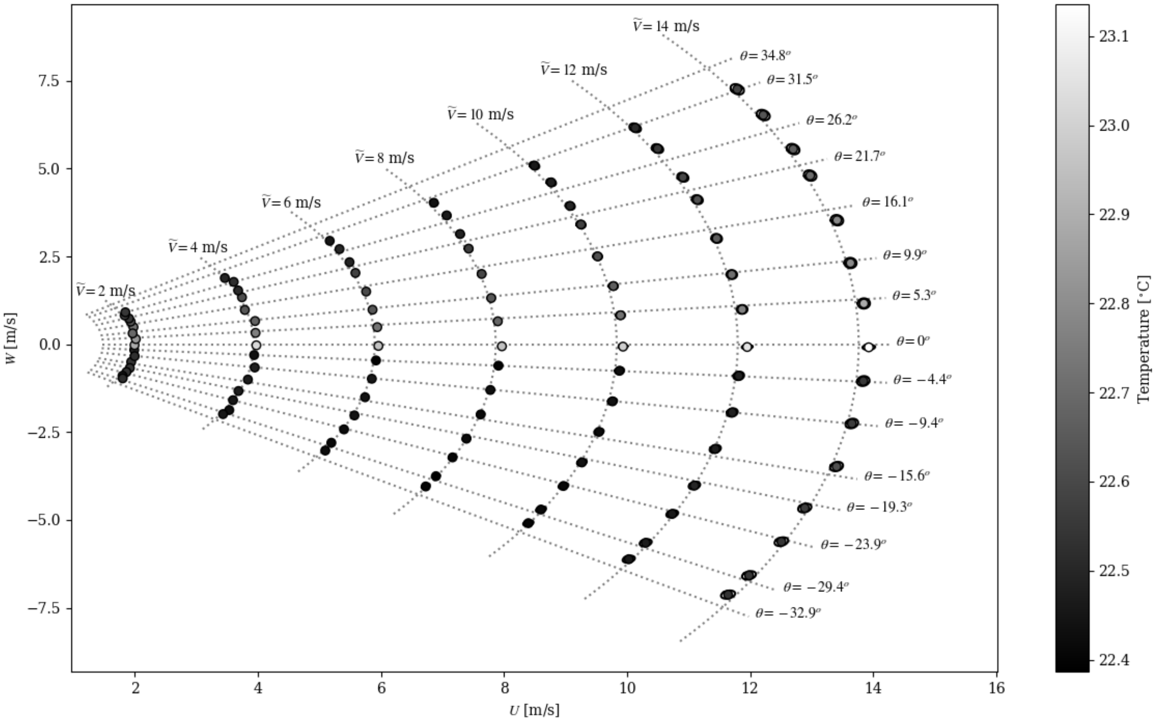

Figure A.22: Case 8: Freestream simulation component results and uncertainties.

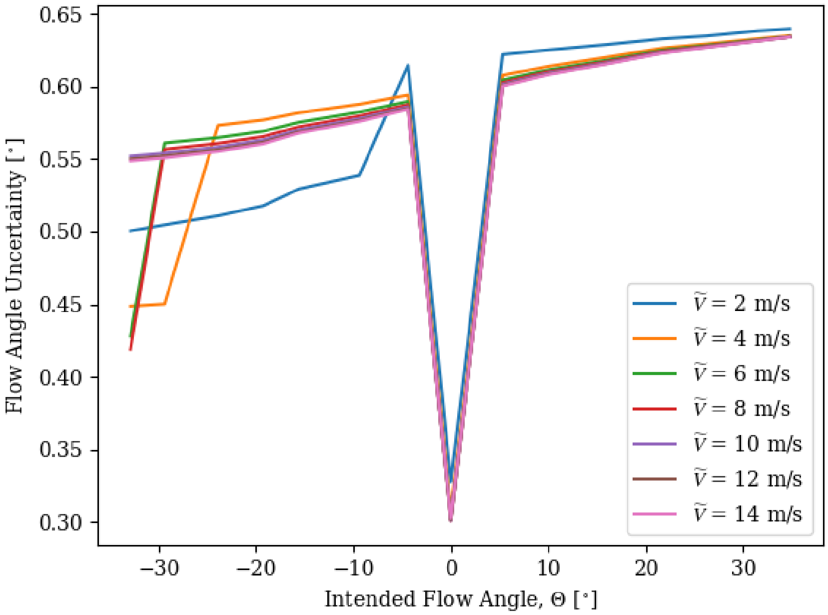

(a) Uncertainty in flow angle, θ.

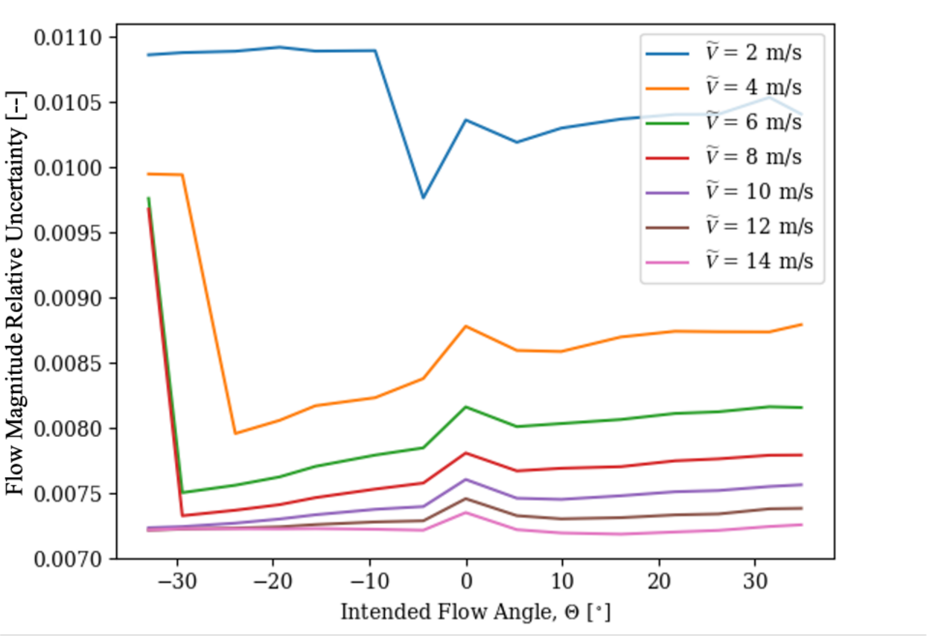

(b) Uncertainty in flow magnitude, $\widetilde{V}$.

Figure A.23: Case 8: Freestream simulation uncertainty in velocity magnitude and flow angle. Each colored line corresponds to measurements taken at a constant velocity magnitude for a variety of flow angles.

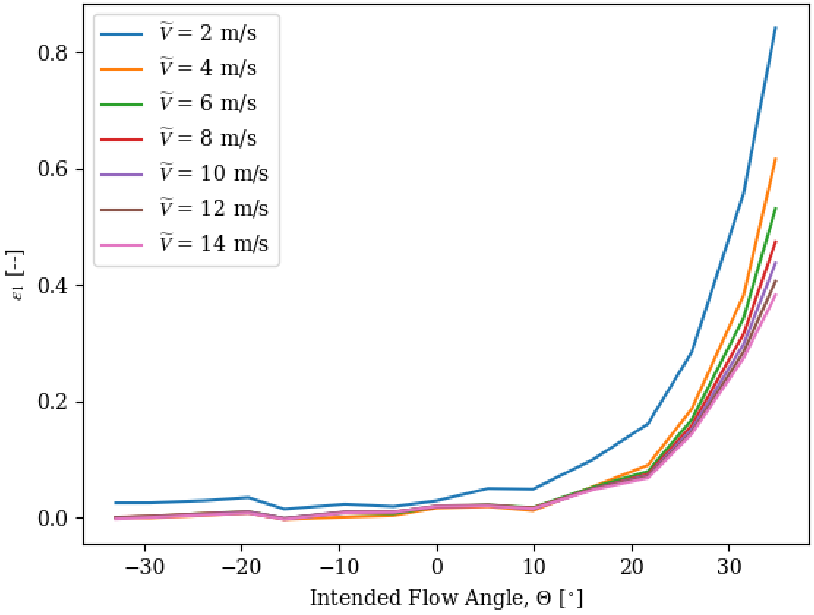

(a) Effective velocity error, $\epsilon_1\left(\widetilde{V}, \theta\right)$.

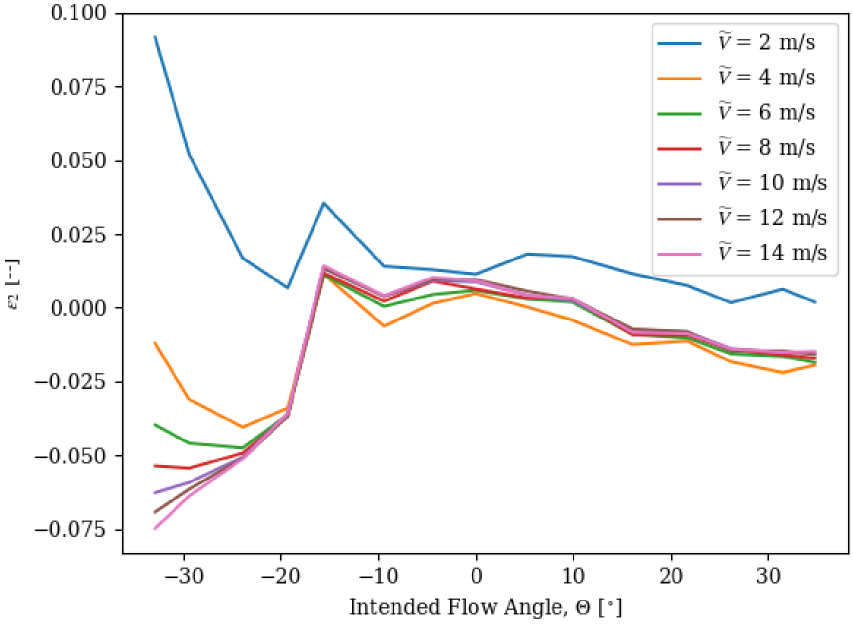

(b) Effective velocity error, $\epsilon_2\left(\widetilde{V}, \theta\right)$.

Figure A.24: Case 8: Freestream simulation model-form error in effective velocities. Each colored line corresponds to measurements taken at a constant velocity magnitude for a variety of flow angles.

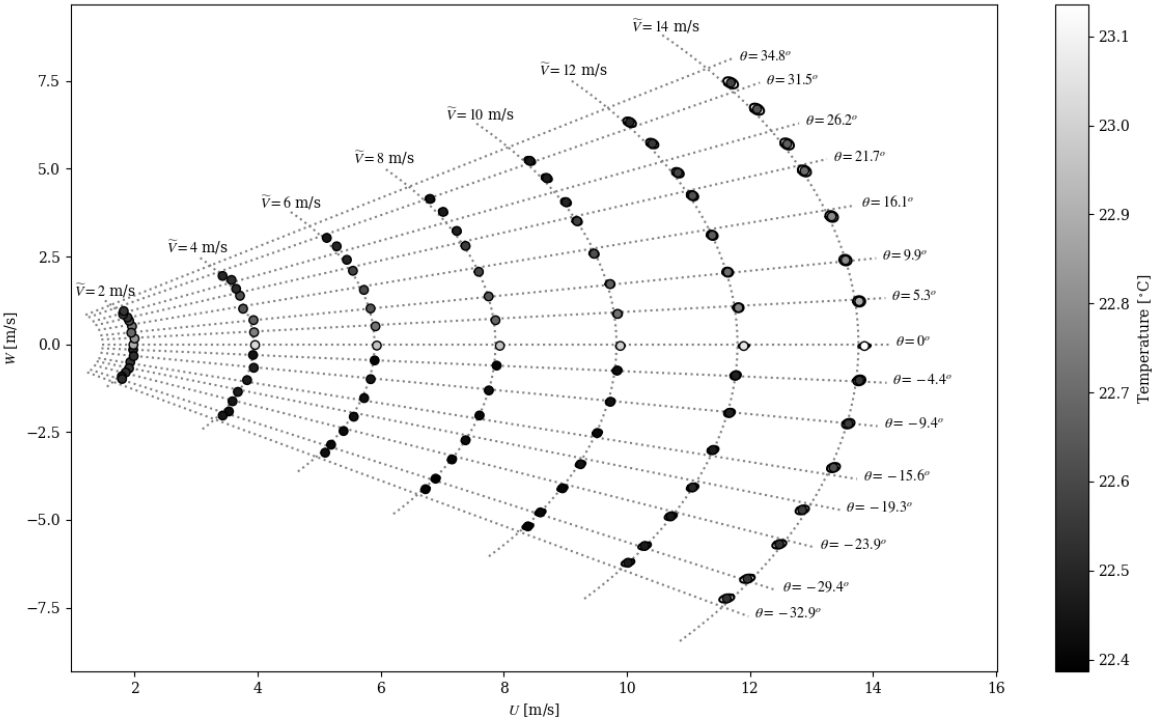

Figure A.25: Case 9: Freestream simulation component results and uncertainties.

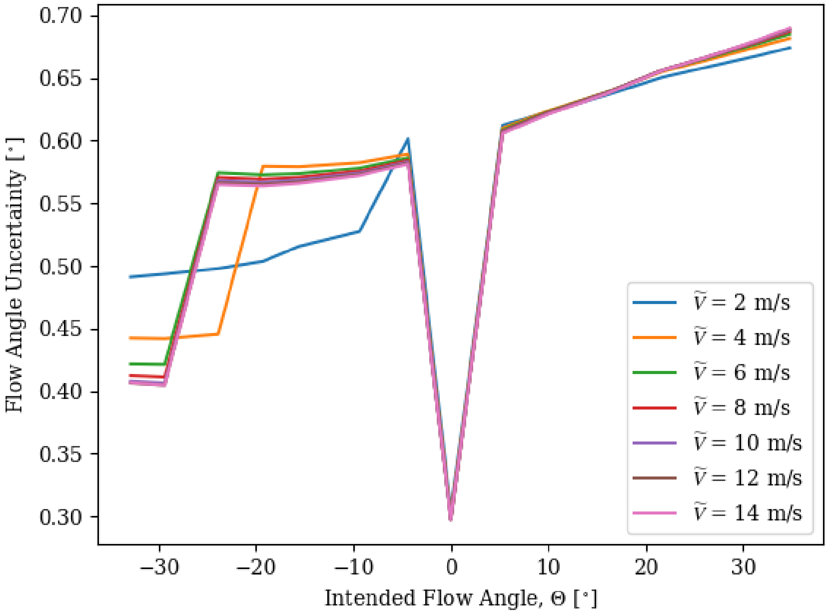

(a) Uncertainty in flow angle, θ.

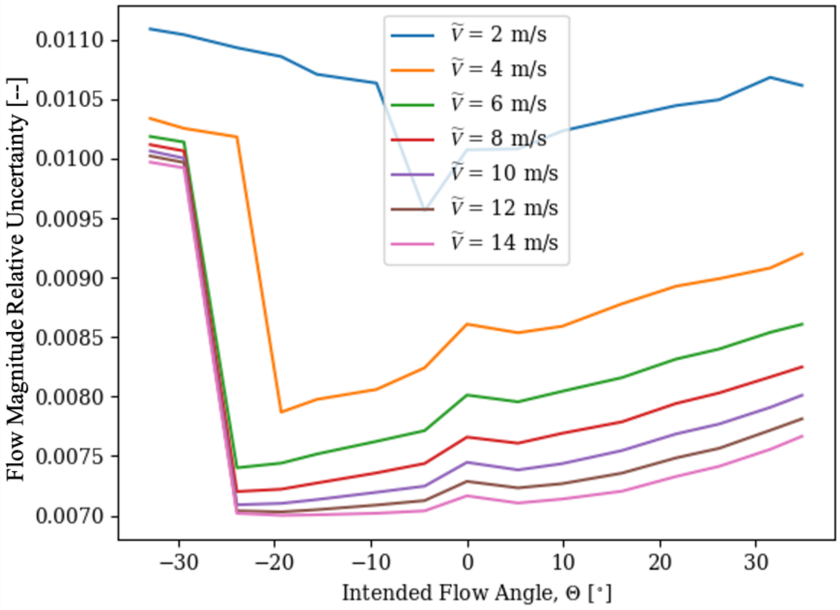

(b) Uncertainty in flow magnitude, $\widetilde{V}$.

Figure A.26: Case 9: Freestream simulation uncertainty in velocity magnitude and flow angle. Each colored line corresponds to measurements taken at a constant velocity magnitude for a variety of flow angles.

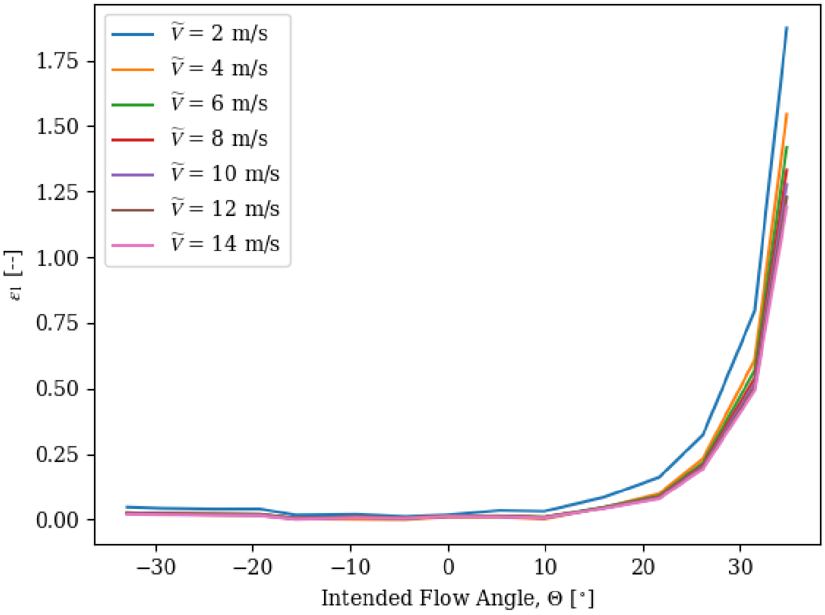

(a) Effective velocity error, $\epsilon_1\left(\widetilde{V},\theta\right)$.

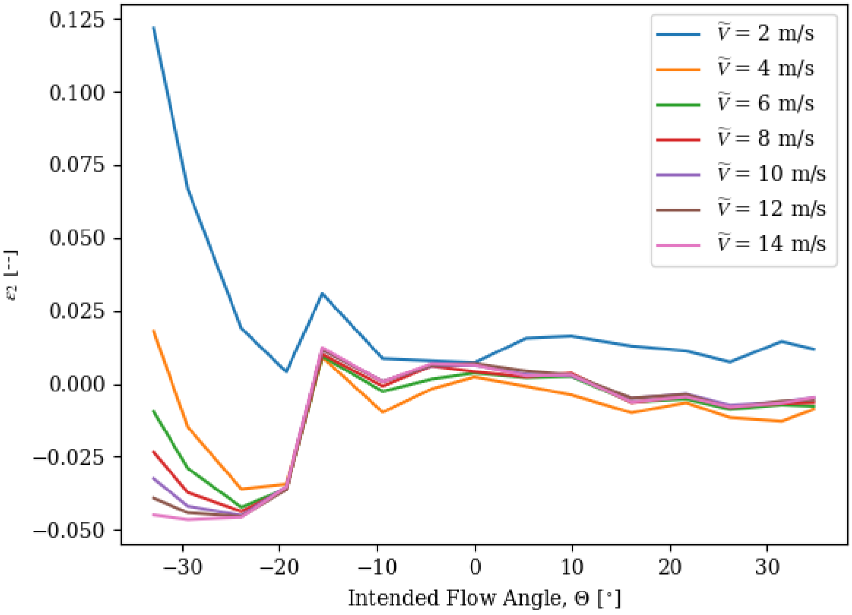

(b) Effective velocity error, $\epsilon_2\left(\widetilde{V},\theta\right)$.

Figure A.27: Case 9: Freestream simulation model-form error in effective velocities. Each colored line corresponds to measurements taken at a constant velocity magnitude for a variety of flow angles.

APPENDIX B

ADDITIONAL VORTEX GENERATOR WAKE RESULTS

This section contains the results of cross-style and single-normal hotwire scans in the wake of a vortex generator. Measurements were collected for a series of streamwise planes $\Delta x = [40,\ 80,\ 120,\ 160,\ 200]$ mm downstream of the vortex generator trailing edge and are discussed in Chapter 6.

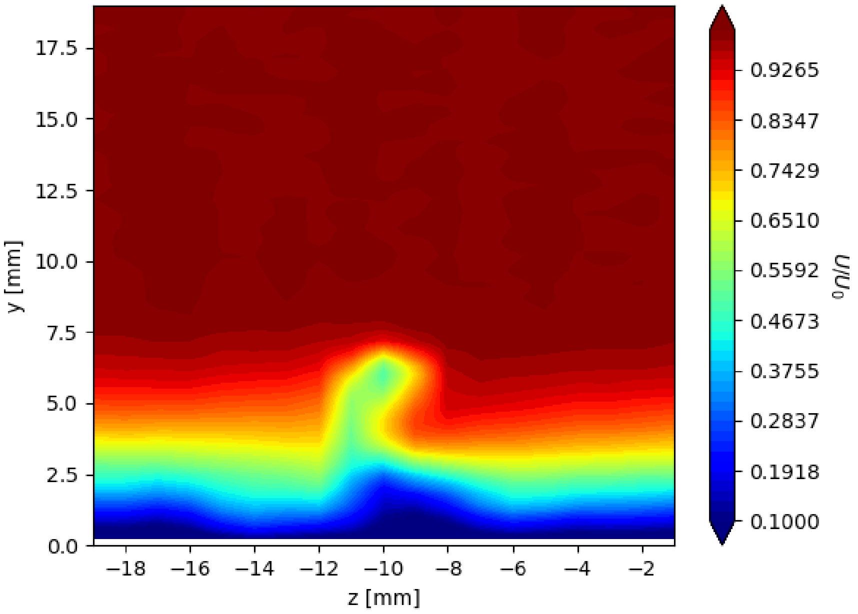

(a) Single-normal U/U_∞ measurement.

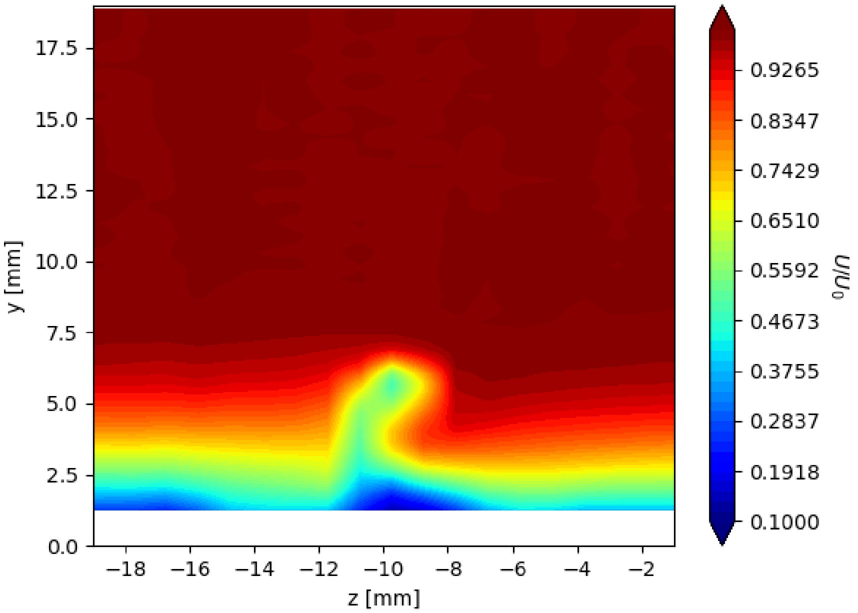

(b) Crosswire U/U_∞ measurement.

Figure B.1: Single-normal and cross-style hotwire U component measurement comparison at $\Delta x = 40$ mm downstream of the vortex generator trailing edge. White space near the wall corresponds to where the hotwires don't have sufficient information to resolve the velocity components.

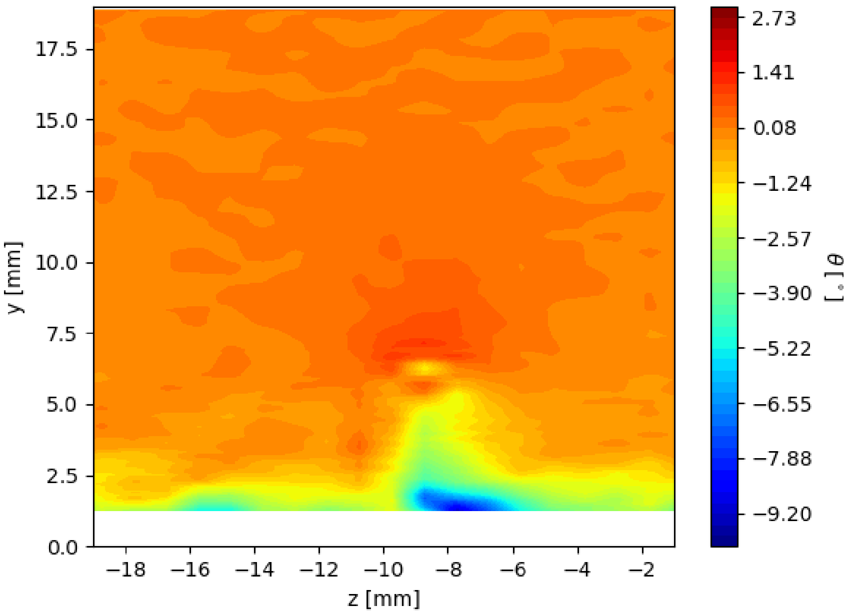

(a) Crosswire flow angle measurement.

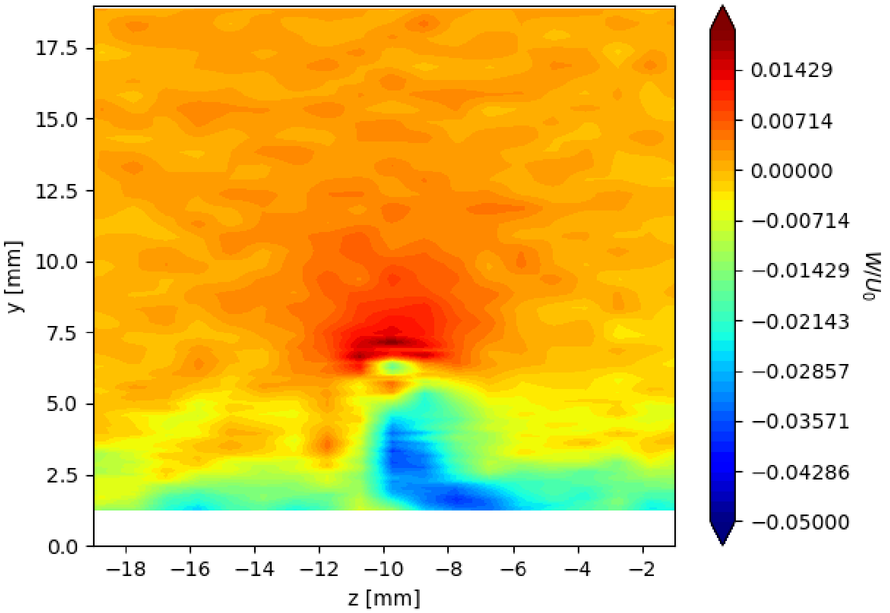

(b) Crosswire W/U_∞ measurement.

Figure B.2: Cross-style hotwire W component measurement and flow angle, θ, at $\Delta x = 40$ mm downstream of the vortex generator trailing edge. White space near the wall corresponds to where the crosswire doesn't have sufficient information to resolve the velocity components.

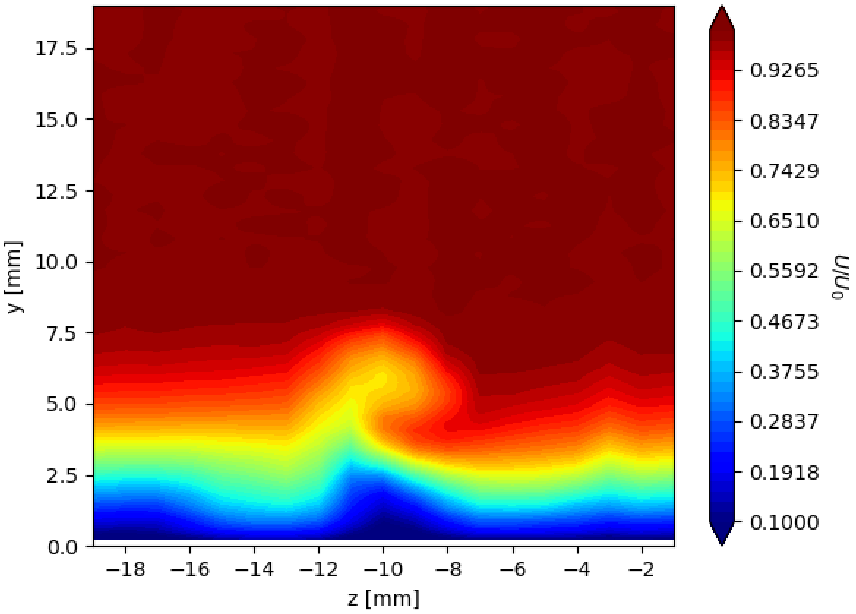

(a) Single-normal U/U_∞ measurement.

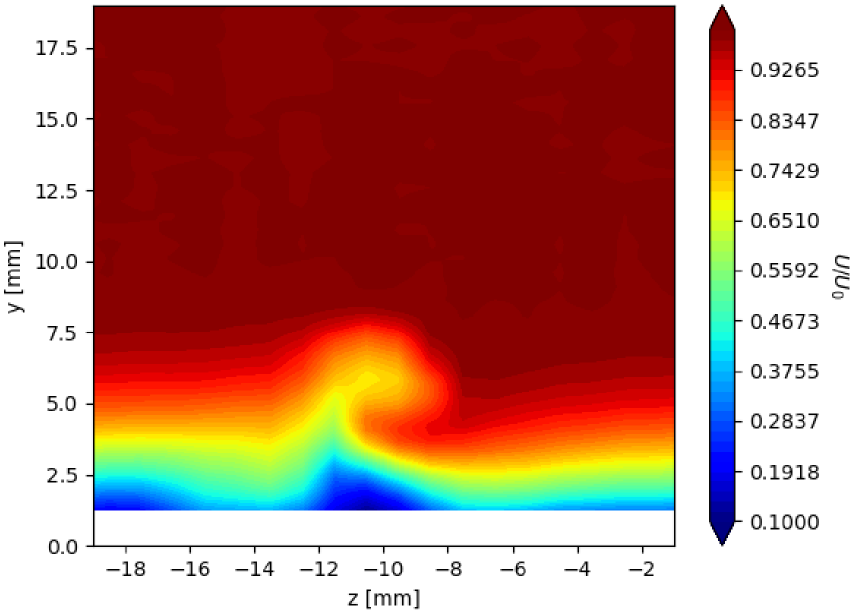

(b) Crosswire U/U_∞ measurement.

Figure B.3: Single-normal and cross-style hotwire U component measurement comparison at $\Delta x = 80$ mm downstream of the vortex generator trailing edge. White space near the wall corresponds to where the hotwires don't have sufficient information to resolve the velocity components.

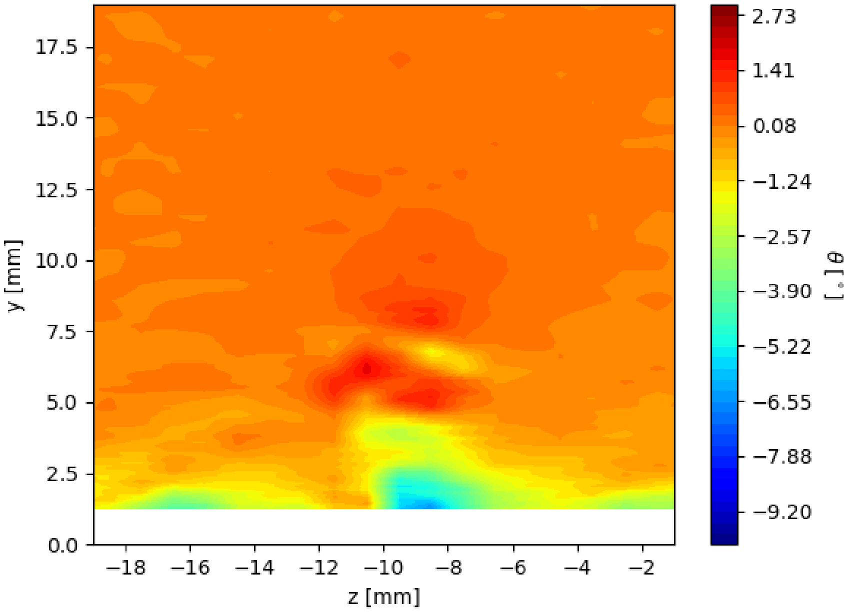

(a) Crosswire flow angle measurement.

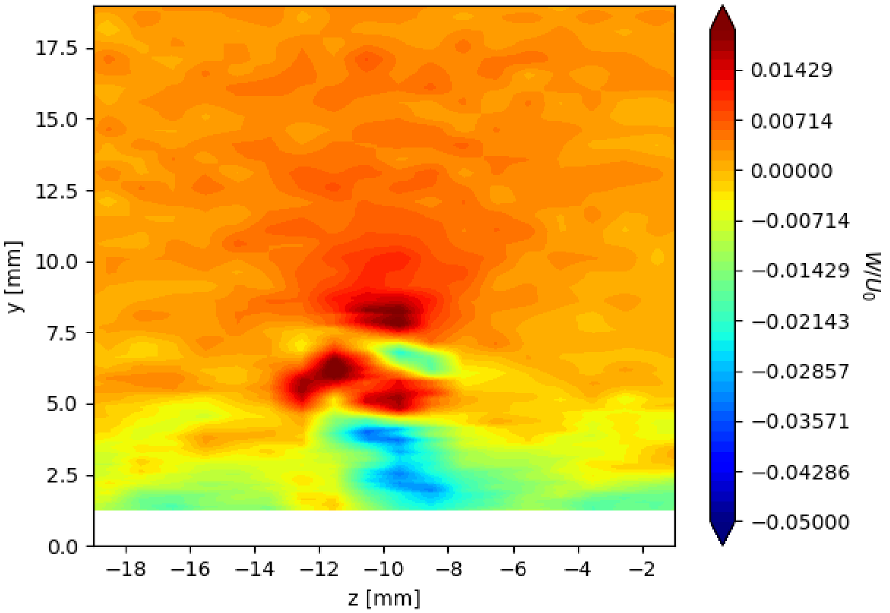

(b) Crosswire W/U_∞ measurement.

Figure B.4: Cross-style hotwire W component measurement and flow angle, θ, at $\Delta x = 80$ mm downstream of the vortex generator trailing edge. White space near the wall corresponds to where the crosswire doesn't have sufficient information to resolve the velocity components.

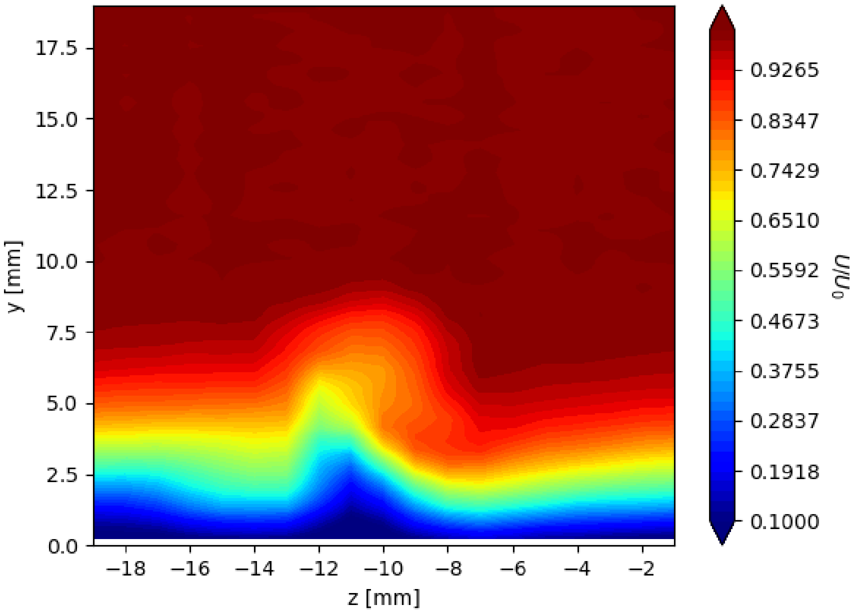

(a) Single-normal U/U_∞ measurement.

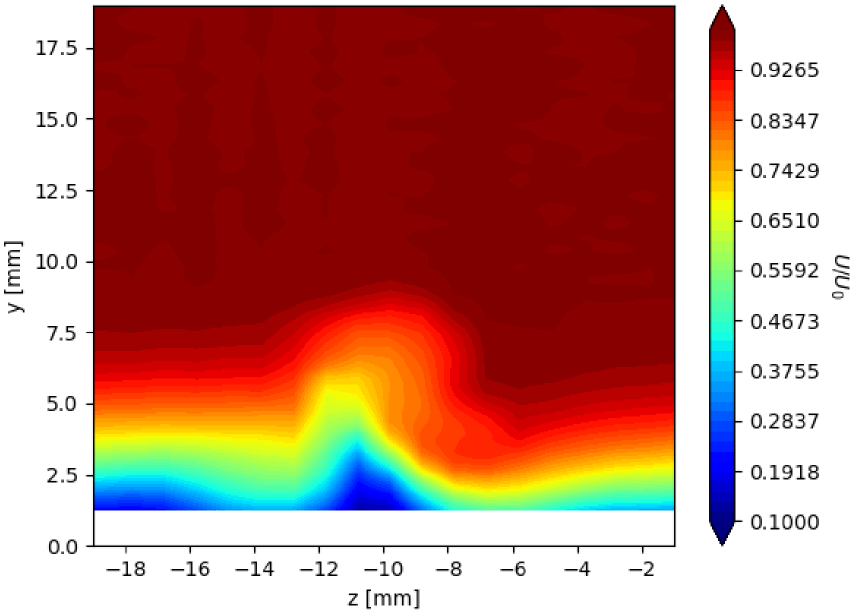

(b) Crosswire U/U_∞ measurement.

Figure B.5: Single-normal and cross-style hotwire U component measurement comparison at $\Delta x = 120$ mm downstream of the vortex generator trailing edge. White space near the wall corresponds to where the hotwires don't have sufficient information to resolve the velocity components.

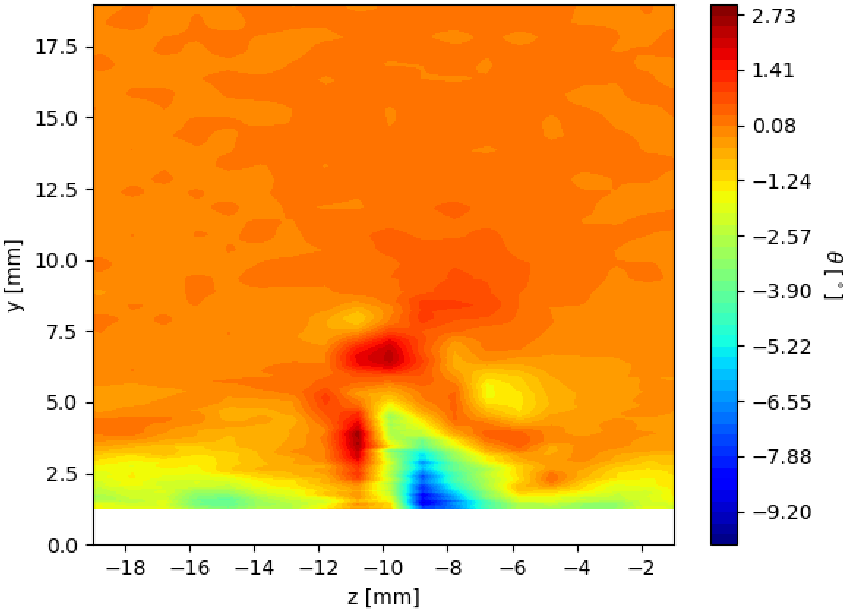

(a) Crosswire flow angle measurement.

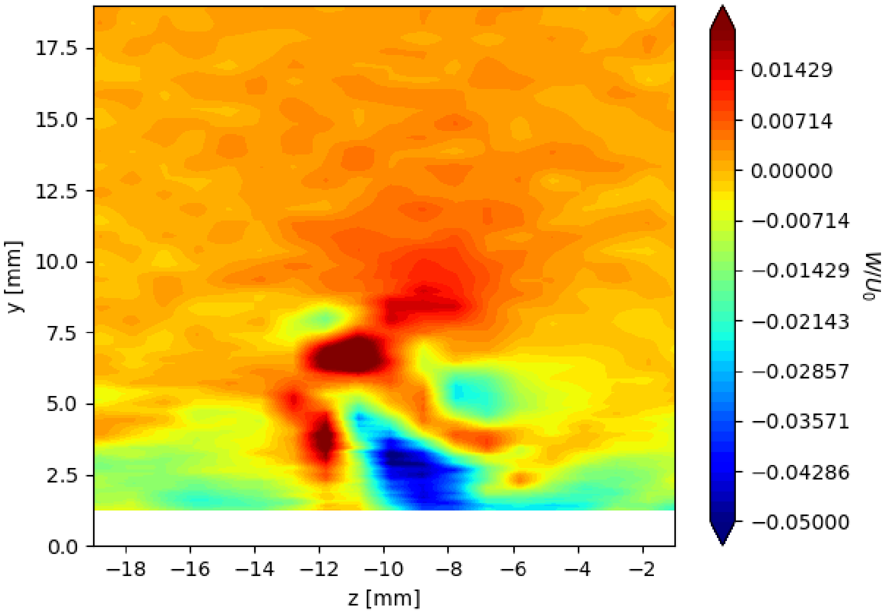

(b) Crosswire W/U_∞ measurement.

Figure B.6: Cross-style hotwire W component measurement and flow angle, θ, at $\Delta x = 120$ mm downstream of the vortex generator trailing edge. White space near the wall corresponds to where the crosswire doesn't have sufficient information to resolve the velocity components.

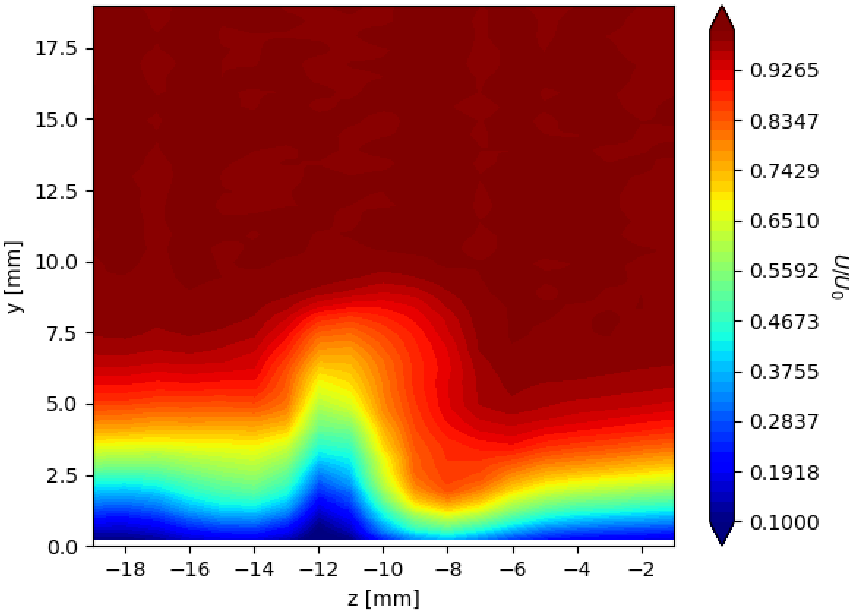

(a) Single-normal U/U_∞ measurement.

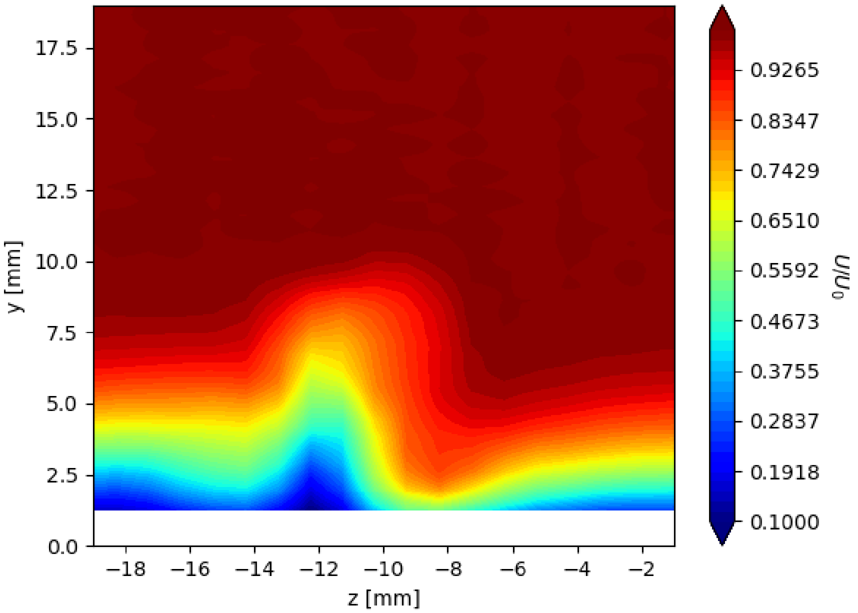

(b) Crosswire U/U_∞ measurement.

Figure B.7: Single-normal and cross-style hotwire U component measurement comparison at $\Delta x = 160$ mm downstream of the vortex generator trailing edge. White space near the wall corresponds to where the hotwires don't have sufficient information to resolve the velocity components.

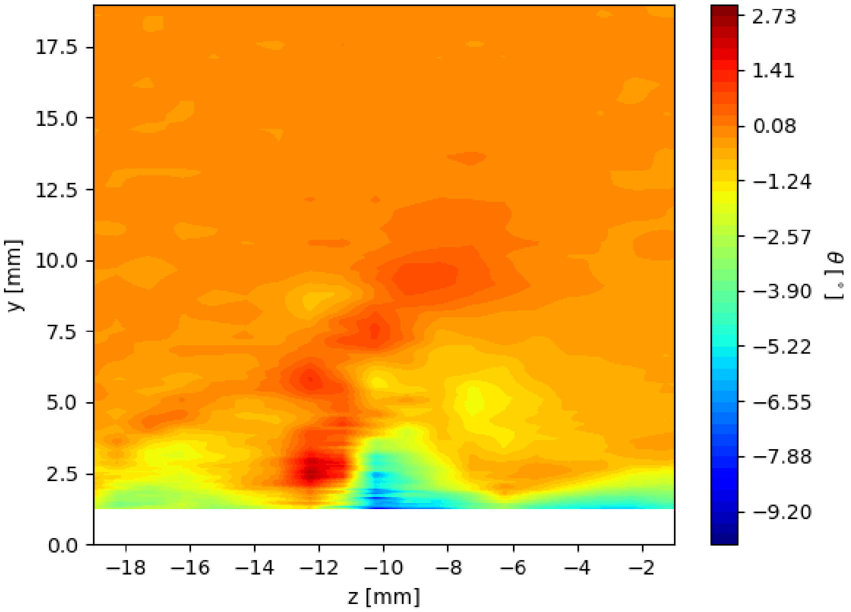

(a) Crosswire flow angle measurement.

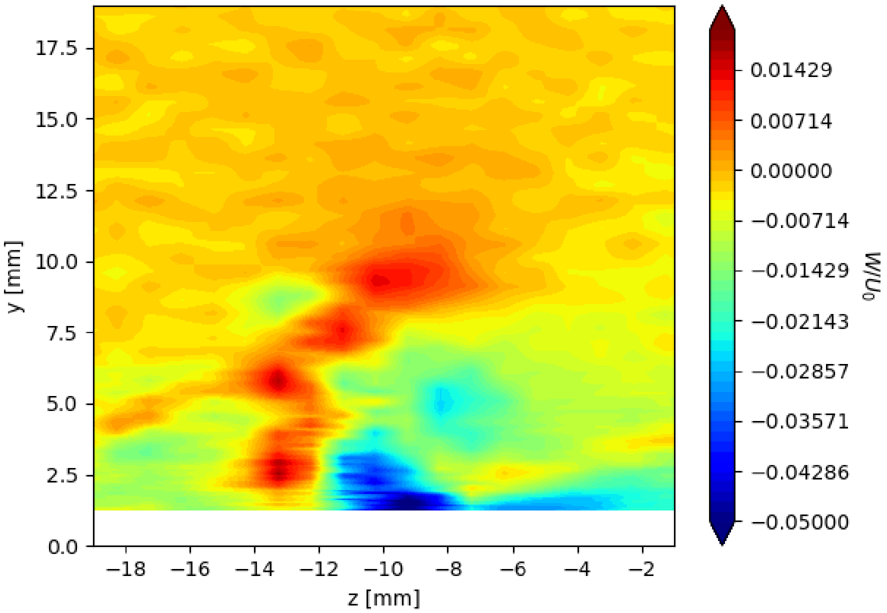

(b) Crosswire W/U_∞ measurement.

Figure B.8: Cross-style hotwire W component measurement and flow angle, θ, at $\Delta x = 160$ mm downstream of the vortex generator trailing edge. White space near the wall corresponds to where the crosswire doesn't have sufficient information to resolve the velocity components.

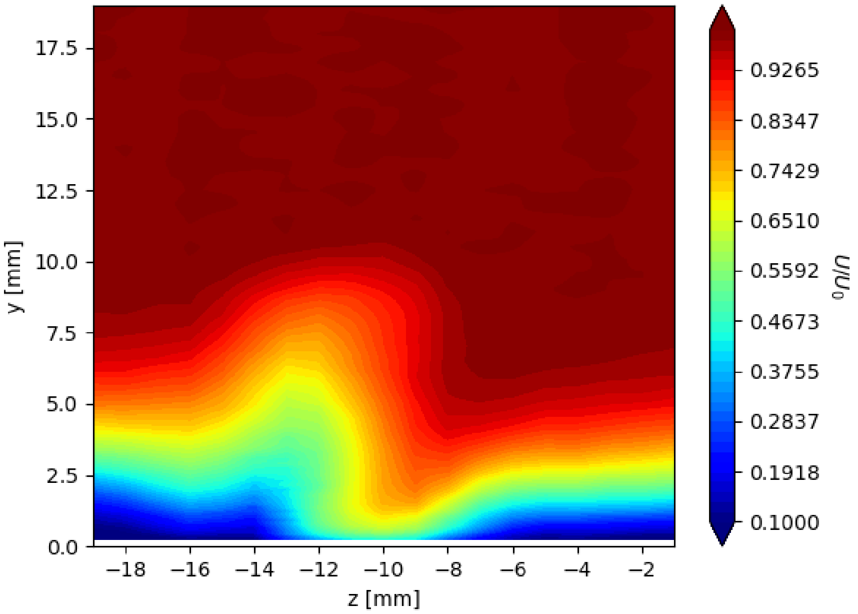

(a) Single-normal U/U_∞ measurement.

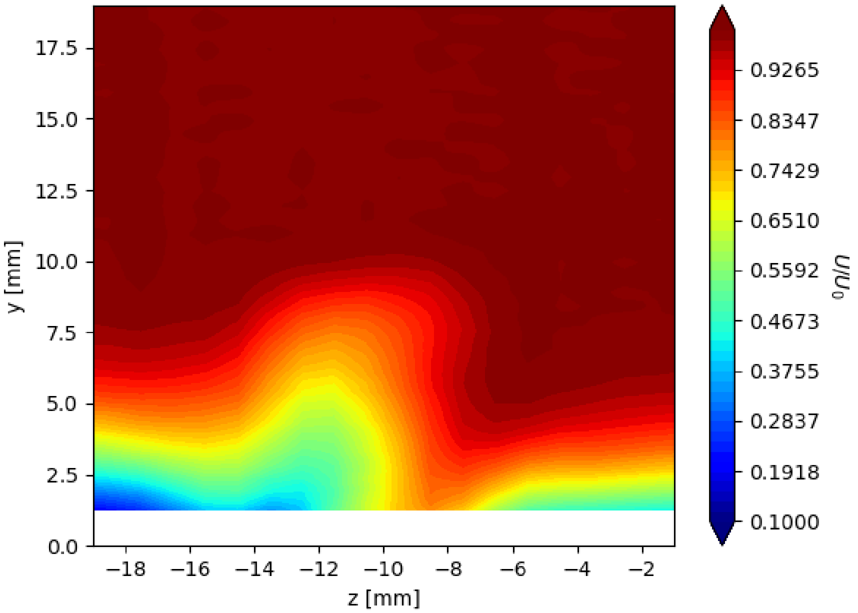

(b) Crosswire U/U_∞ measurement.

Figure B.9: Single-normal and cross-style hotwire U component measurement comparison at $\Delta x = 200$ mm downstream of the vortex generator trailing edge. White space near the wall corresponds to where the hotwires don't have sufficient information to resolve the velocity components.

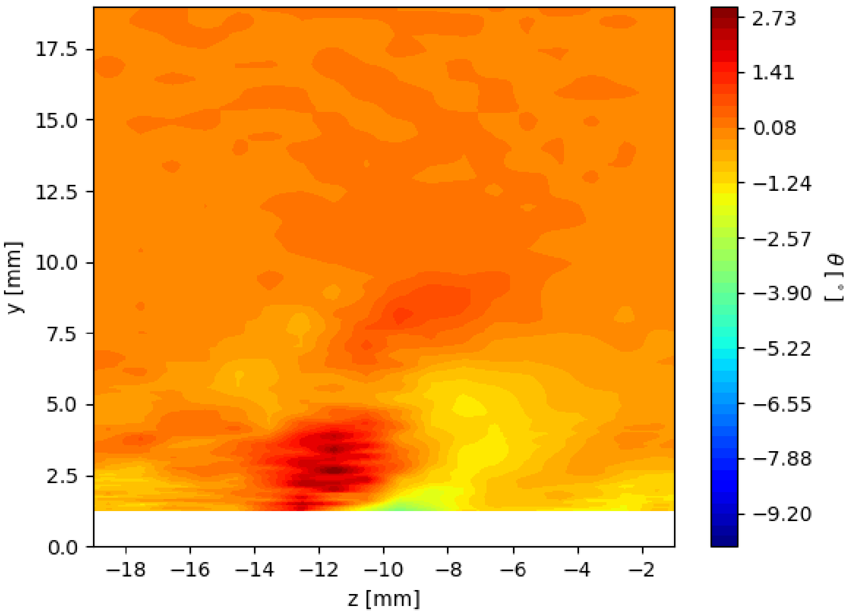

(a) Crosswire flow angle measurement.

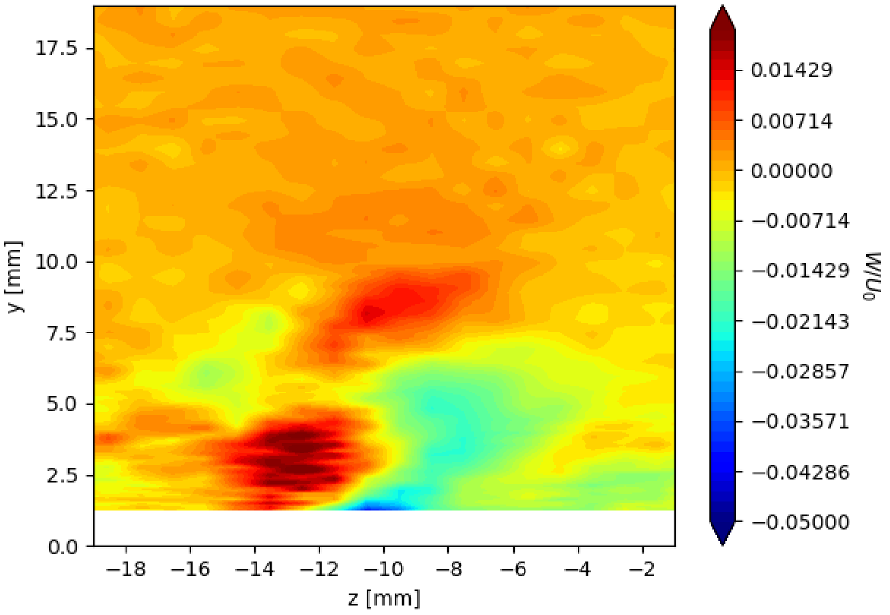

(b) Crosswire W/U_∞ measurement.

Figure B.10: Cross-style hotwire W component measurement and flow angle, θ, at $\Delta x = 200$ mm downstream of the vortex generator trailing edge. White space near the wall corresponds to where the crosswire doesn't have sufficient information to resolve the velocity components.